STUDIES ON HELIUM COOLED PLASMA FACING COMPONENTS FOR TOKAMAK BASED FUSION REACTOR APPLICATIONS

By

SANDEEP RIMZA

ENGG06201104004

Institute for Plasma Research, Gandhinagar

A thesis submitted to the

Board of Studies in Engineering Sciences

In partial fulfillment of requirements

For the Degree of

DOCTOR OF PHILOSOPHY

of

HOMI BHABHA NATIONAL INSTITUTE

Feb - 2016

Homi Bhabha National Institute

Recommendations of the Viva Voice Board

As members of the Viva Voce Committee, we certify that we have read the dissertation prepared by **Sandeep Rimza** entitled **"Studies on Helium Cooled Plasma Facing Components for Tokamak based Fusion Reactor Applications"** and recommend that it may be accepted as fulfilling the thesis requirement for the award of Degree of Doctor of Philosophy.

Chairman: Dr. Shashank Chaturvedi	**Date:** 17/05/2016
Guide: Dr. Samir S. Khirwadkar	**Date:** 17/05/2016
Co-guide: Dr. Karupanna Velusamy	**Date:** 17/05/2016
Examiner: Dr. Prasad Patnaik B.S.V	**Date:** 17/05/2016
Member 1: Dr. Subroto Mukherjee	**Date:** 17/05/2016
Member 2: Dr. Surya Kumar Pathak	**Date:** 17/05/2016

Final approval and acceptance of this thesis is contingent upon the candidate's submission of the final copies of the thesis to HBNI.

I hereby certify that I have read this thesis prepared under my direction and recommend that it may be accepted as fulfilling the thesis requirement.

Date: 17/05/2016

Place: Institute for Plasma Research (IPR)
Gandhinagar

Dr. Samir S. Khirwadkar
(Guide)

STATEMENT BY AUTHOR

This dissertation has been submitted in partial fulfillment of requirements for an advanced degree at Homi Bhabha National Institute (HBNI) and is deposited in the Library to be made available to borrowers under rules of the HBNI.

SRim89

Sandeep Rimza

DECLARATION

I, hereby declare that the investigation presented in the thesis has been carried out by me. The work is original and has not been submitted earlier as a whole or in part for a degree/diploma at this or any other Institution/University.

Sandeep Rimza

LIST OF PUBLICATIONS

Journal:

a. Accepted:

1. "Computational fluid dynamic studies on plasma facing heat sink concept for tokamak application", **S. Rimza**, S. Khirwadkar, K. Velusamy, *Applied Thermal Engineering (Elsevier)*, **2016**, 100, 1274–1291.

2. "Optimal design of divertor heat sink with different geometric configurations of sectorial extended surfaces", **S. Rimza**, K. Satpathy, S. Khirwadkar, K. Velusamy, *Fusion Engineering and Design (Elsevier),* **2015**, 100, 581–595.

3. "An experimental and numerical study of flow and heat transfer in helium cooled divertor finger mock-up with sectorial extended surfaces", **S. Rimza**, S. Khirwadkar, K. Velusamy, *Applied Thermal Engineering (Elsevier),* **2015**, 82, 390–402.

4. "Numerical studies on helium cooled divertor finger mock up with sectorial extended surfaces", **S. Rimza**, K. Satpathy, S. Khirwadkar, K. Velusamy, *Fusion Engineering and Design (Elsevier)***,** **2014**, 89, 2647–2658.

b. Communicated:

1. **"**Development of Heat Sink Concept for Near Term Fusion Power Plant Divertor", **S. Rimza**, S. Khirwadkar, K. Velusamy, *Journal of physics (IOP).*

c. To be Communicated:

1. "Effect of nozzle shapes, arrangement and nozzle diameter on the thermal performance of helium cooled divertor heat sink concept" **S. Rimza**, S. Khirwadkar, K. Velusamy, *Nuclear Engineering and Technology*.

Conferences:

1. "Development of heat sink concept for near-term fusion power plant divertor", **S. Rimza**, S.S. Khirwadkar, K. Velusamy, , 10th *Asia Plasma & Fusion Association Conference (APFA - 2015),* Gandhinagar, INDIA, 14th -18th Dec 2015.

2. "Numerical studies on helium cooled divertor finger mock-up with sectorial extended surfaces", **S. Rimza**, K. Satpathy, S.S. Khirwadkar, K. Velusamy, , 41th *International Conference on Fluid Mechanics and Fluid Power,* IIT-Kanpur, INDIA, 12th -14th Dec 2014.

3. "Studies on divertor cooling finger of helium mock-up through CFD approach", **S. Rimza**, K. Satpathy, S. Khirwadkar, K. Velusamy, Proceeding of the *International Workshop on New Horizons in Nuclear Reactor Thermal Hydraulics and Safety*, BARC, Mumbai, INDIA, 13th - 15th Jan 2014.

4. "DEMO Divertor Readiness Gaps and Needed R&D", S.S. Khirwadkar, V. Menon, **S. Rimza** et al., 1st *IAEA DEMO programme workshop* , University of California, Los Angeles, California, USA, 15th -18th Oct 2012.

Institute Technical Reports

1. "An advanced divertor heat sink concept for DEMO", **S. Rimza**, S. khirwadkar, K. Velusamy, **IPR/RR/751, 2015**.

2. "An experimental investigation of helium cooled divertor finger mock-ups", **S. Rimza**, S. khirwadkar, K. Velusamy, **IPR/RR/722, 2015**.

3. "Effect of geometric variations of sectorial extended surface on thermal performance of divertor finger mock-up", **S. Rimza**, K. Satpathy, S.S. Khirwadkar, K. Velusamy, **IPR/RR/650, 2014.**

4. "Numerical studies on helium cooled divertor finger mock up with sectorial extended surface", **S. Rimza**, K. Satpathy, S.S. Khirwadkar, K. Velusamy, **IPR/RR/ 627, 2013.**

5. "Studies on divertor cooling finger of helium mock-up through CFD approach", **S. Rimza**, K. Satpathy, S.S. Khirwadkar, V. Menon, D. Krishnan, **IPR/TR/ 237, 2012.**

Srimza

Sandeep Rimza

Dedication

Every piece of work needs self effort as well as guidance of those who were very close to our heart.

My humble effort I dedicated to my sweet and loving

Parents and Brothers

&

My Wife Akanksha & Daughter Dishani

Whose affection and love make me able to get such success and honor,

Along with all hard working and respected

Teachers

ACKNOWLEDGEMENT

Every piece of work done by an individual is a result of direct or indirect support and help of many others. I take this opportunity to acknowledge the people who helped me during my doctoral studies. First and foremost, I would like to express my deep and sincere gratitude to my guide **Dr. Samir S. Khirwadkar**, Head, *Divertor and First wall Technology Development Division (DFD), Institute for Plasma Research (IPR),* for his constant encouragement, caring, and insightful guidance in all the ways leading to the completion of my PhD work. His intellect and friendliness have made my research life more smooth and enjoyable. I specially thank him a lot and place my admiration on record.

I would like to acknowledge and extend my heartfelt gratitude to my co-guide **Dr. Karupanna Velusamy,** Head, *Mechanics and Hydraulics Division, Reactor Design Group (RDG), Indira Gandhi Centre for Atomic Research (IGCAR),* for his consistent and invaluable guidance throughout the thesis period without which I could not have learnt and he never accepted anything less than my best efforts.

I am deeply indebted to my Doctoral Committee Members **Dr. Shashank Chaturvedi, Dr. Subroto Mukherjee and Dr. Surya Kumar Pathak** towards timely reviewing the thesis work and giving insightful suggestions and advice. I would like to express my deep thanks to **Dr. Kamalakanta Satpathy,** for his suggestions, friendly support and advice and timely tough warnings.

I gratefully acknowledge **Mr. Sunil M. Belsare**, **Mr. Vinay Menon, Mr. Rajmannar Swamy, Mr. Deepu S. Krishnan** and **Mr. M. Rajendrakumar (IGCAR),** for their valuable contributions. I sincerely appreciate their kind help and sharing their scientific and technical knowledge through discussions and suggestions.

I thank to all members of DFD Division especially **Mr. Tushar Patel, Mr. Prakash K. Mokaria, Mr. Kalpesh Galodiya** and **Mr. Nikunj Patel** for their help in performing the experiment at Vidhata Lab, Gandhinagar (India).

I would also like to acknowledge **Mr. Gattu Ramesh Babu, Mr. Santra Prosenjit, Mr. Vipul More** and **Mr. Ranjitkumar S** for their valuable contributions. I sincerely appreciate their kind help and sharing their scientific and technical knowledge through discussions and suggestions.

My sincere gratitude to all my former and present fellow research scholars for making my life more cheerful during my stay at IPR hostel. Last but not the least, I would like to express my heartiest gratitude and honor to my family members and friend especially **Mr. Vishesh Verma** who are with me during the ups and downs of my life.

Sandeep Rimza

CONTENTS

SYNOPSIS

It is generally accepted that fusion power is one of the promising sources of sustainable energy in the future. Towards development of fusion reactor technology, India is seriously pursuing research and development activities through Department of Atomic Energy (DAE) at the Institute for Plasma Research along with support from other DAE as well as Non-DAE institutions. The study was launched with the aim of developing an innovative power plant concept for future fusion reactor known as “DEMO” reactor. However, there are many challenges towards successful design of the DEMO. One among them is the design of the divertor which is an important part of the fusion reactor that handles extremely high heat and particle flux escaping from the hot core plasma region along Scrape-Off-Layer (SOL). The function of the divertor is to remove fusion ash, plasma impurities, and unburned fuel from the reactor which affects the quality of the plasma.

The entire divertor system is typically divided into a number of modules known as “Cassettes” for improved handling, assembly/dis-assembly, repair and maintenance. Each cassette consists of plasma facing “Divertor targets” with respective support structures and coolant supply network. Each divertor target is made of tungsten material with appropriate cooling mechanism to extract the heat energy. Tungsten (W) is the preferred choice to be used as plasma facing material for covering the entire surface of divertor target due to its excellent thermo-physical properties such as high melting point, low thermal expansion, high thermal conductivity, low tritium retention, low erosion/sputtering rate, low-neutronic activation.

In the present helium cooled divertor concept study, divertor target is made up of numerous “finger” type assemblies cooled using high pressure high temperature helium gas to extract the heat energy. Helium gas has been chosen as the coolant due to its favourable safety characteristics and its ability to operate at high temperatures, which enhances the thermal efficiency of the power conversion systems. However, major drawbacks are its comparatively poor heat exchange capability and considerably large pumping power requirement. In the context of DEMO, it is desirable to explore efficient cooling technology for helium cooled divertor, which can withstand high heat flux values of ~10 MW/m^2.

Towards this, a novel design for heat transfer enhancement of helium cooled divertor finger mock-up has been proposed. Heat transfer characteristics of finger mock-up have been numerically investigated with new sectorial extended surfaces (SES). Numerical investigations show that addition of SES greatly increases thermal-hydraulic performance of the finger mock-up. Detailed parametric studies on critical parameters that influence thermal performance of the finger mock-up have been analysed. Thermo-mechanical analysis has also been carried out through finite element based approach to know the state of stress in the assembly as a result of large temperature gradients. It is seen that the stresses are within the permissible limits for the divertor design.

In order to validate the findings, experimental and computational approach has been proposed for the evaluation of thermal hydraulics performance of a finger type divertor with SES. Critical thermal hydraulic parameters, effective heat transfer coefficient and pressure loss have been measured in the experiment for the reference divertor as well as for a divertor with SES. The thermal performance has been evaluated by comparing the heat transfer coefficient and pressure drop across the test section. The experimental mock-ups are made to full scale respecting Reynolds and Prandtl number similarities. Air is used as the simulant to represent helium, which is the coolant in prototype. Heat concentrator has been developed to simulate the high heat flux, by electrical heating. The benchmark experimental data have been used to validate the three dimensional conjugate heat transfer models. The computational result for heat transfer coefficients and pressure loss are in satisfactory agreement with the experimental results. Based on detailed parametric studies, correlations have been proposed for Nusselt number (Nu) and pressure loss coefficient (K_L) as a function of Reynolds number which can be used for design applications. The proposed SES divertor is seen to significantly augment the thermal performance of the finger type divertor at the penalty of a minimum pressure drop at the prototypical condition. The results of the present study provide added confidence in the numerical model used to design the divertor and its applicability to other high heat flux gas cooled components.

Following satisfactory validation, elaborate parametric studies have been carried out towards geometrical optimization of divertor finger mock-up with SES to enhance the thermal hydraulic performance. Various non dimensional design variables, viz., relative pitch, thickness, jet diameter, the ratio of height of SES to jet diameter and circumferential position of the SES are considered for the optimization study. The analysis reveals that, the heat transfer performance of finger mock-up with SES is improved for two optimum designs having relative pitch and thickness of 0.30 and 0.56 respectively. Also, it is observed that finger mock-up heat sink with SES performs better, when the ratio of SES height to jet diameter, reduces to 0.75 at the cost of marginally higher pumping power. The effects of jet diameter and circumferential position of SES are found to be counterproductive towards the heat transfer performance. To understand the stress distribution in the optimized geometries, a combined computational fluid dynamics and structural analysis has been carried out. It is found that deviation in peak stresses among various optimized geometries is not significant.

Development of an efficient divertor concept is an important task to meet in the scenario of the fusion power plant. Therefore, an innovative divertor heat sink concept cooled by helium is proposed for the fusion reactor. The first wall of the divertor made-up of several modules has to overcome the stresses caused by high heat flux, in the proposed design. Thermal hydraulic performance of one such divertor heat sink module is numerically investigated. The effects of critical thermal hydraulic and geometric parameters on the heat transfer characteristics are investigated as a function of Reynolds number.

The 3-dimensional thermal hydraulic investigations include thimble diameter (D_T), nozzle diameter (D_N), the ratio of nozzle to wall space and nozzle diameter (H/D_N) and nozzle shapes etc. as parameters. Elliptical nozzles at specific orientation are found to perform better than other nozzles for identical Reynolds number. The performances of triangular nozzles are found to be poorer than other nozzles. Similarly, a minimum thimble temperature and pressure drop in the circuit is achieved at H/D_N ~1.66. The proposed design is found to have a margin of 10 % i.e., capable of handling 11 MW/m^2 against target heat flux values of 10 MW/m^2.The stresses induced in the divertor heat sink by the thermal and pressure loads are important factors that limit the life of the divertor. Therefore, structural analysis of the divertor heat sink assembly has been carried out and the stress values arising out of temperature gradient and pressure are found to be within acceptable limits, demanding the reliability of the proposed concept.

LIST OF FIGURES

LIST OF TABLES

CHAPTER 1

INTRODUCTION

1.0. FOREWORD

Global warming caused by increased greenhouse gases has become the most important scientific and political concern during the past few decades. Intergovernmental Panel for Climate Change (IPCC) estimates that global ground-level temperature increase by 1 °C over the period 1880 to 2012 [1]. Therefore, the prime objective of the current energy policy is the reduction in emission of greenhouse gases, particularly CO_2. At the same time, a long-term sustainable energy supply at an affordable cost must be ensured. The choice of the future energy source depends on the availability and cost of fuel, availability of capital funds, political decisions and social acceptance.

The per capita electricity consumption of a country is regarded as a measure of its economic condition. During the year 2014-15, the per capita electricity consumption in India was 1010 kWh with total electricity consumption of 938.823 billion kWh [2]. With the increase in population, tremendous pressure will be exerted on electricity production due to rapid growth in urbanization and industrialization. According to the Ministry of Power, the total installed capacity in India is about 271.722 GW at the end of March 2015. At present, a major portion of Indian energy demand is met by coal, which supplies nearly 61% of the energy requirement. Following this, natural gas contributes to 8%, diesel 1%, hydro power 15%, renewable energy source 13% and nuclear 2%. The statistics show that the major source of energy in India is a fossil fuels, which are exhaustible and also one of the main sources of greenhouse gases. Therefore, developing country like India needs new and cleaner ways to supply the increasing energy demand, as concerns grow over climate change and declining supplies of fossil fuels. The use of nuclear energy allows the lowest impact on the environment since it does not release any gases like carbon dioxide, methane which are mainly responsible for the greenhouse effect.

The power generated through nuclear fusion is a promising energy option for the future energy supply, in which two light nuclei of hydrogen isotopes combine to form a single heavier nucleus with the release of a large amount of energy. The power produced using fusion would have a number of advantages [3]:

- *Environmental compatibility:* The only byproduct in the fusion reactor as a result of fusion reactions is small amount of helium (He), which is an inert gas that does not add to atmospheric pollution.
- *Inexhaustible fuel supplies:* Fuel required for nuclear fusion reaction such as deuterium ($_1D^2$) can be obtained from water and tritium ($_1T^3$) can be produced from lithium, which is found in the earth's crust. Therefore, fuel supplies for fusion reactor will available for millions of years.
- *Energy efficiency:* One gram of fusion fuel can provide the same amount of energy as that of 10,000 liters of fuel oil or 11 tons of coal.
- *Short half-lived radioactive waste:* During the operation no long lived radioactive materials are produced. Only structural components of the plant become radioactive which can be safely recycled or disposed off conventionally within 100 years.
- *Favorable Safety characteristics:* The fusion process is inherently safe because any amplification of the reaction will cause the plasma to extinguish itself and, even if an accident were to occur that would release only fusion fuel to the environment. The amount of fuel present inside the reactor is low enough to ensure that the release to the environment will be at levels much lower than those allowed by current regulations.
- *Reliable power:* The power generated through fusion is appropriate for future base-load electricity, at costs that are similar to other energy sources.

These advantages are great hopes on nuclear fusion as one of the most promising energy supplier to meet the future energy demand.

1.1. PRINCIPLE OF NUCLEAR FUSION

Nuclear fusion is a process in which two light elements such as deuterium (D) and tritium (T) fuse together, and form heavier elements. The resulting heavier elements have slightly less mass than the fusing elements and this mass difference results in the release of enormous amounts of energy. A schematic diagram of fusion reaction is shown in Fig. 1.1.

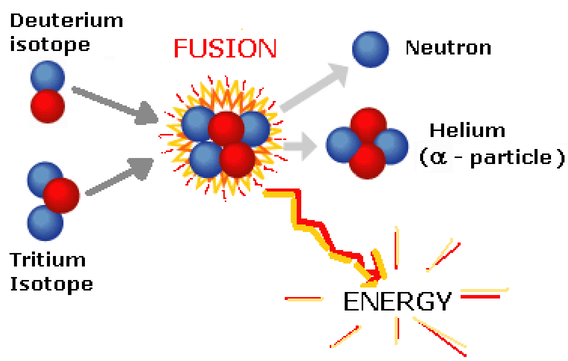

Fig. 1.1. A schematic diagram of fusion reaction.

There are many reactions possible to generate the power from nuclear fusion, which are as follows:

$$_1D^2 + {}_1T^3 \rightarrow {}_2He^4 + {}_0n^1 + 17.6\ \text{MeV} \quad (1.1)$$

$$_1D^2 + {}_1D^2 \rightarrow {}_2He^3 + {}_0n^1 + 3.30\ \text{MeV} \quad (1.2)$$

$$_1D^2 + {}_1D^2 \rightarrow {}_1T^3 + {}_1p^1 + 4.0\ \text{MeV} \quad (1.3)$$

$$_1T^3 + {}_1T^3 \rightarrow {}_2He^4 + {}_0n^2 + 11.3\ \text{MeV} \quad (1.4)$$

Amongst many possible fusion reactions, fusion of the hydrogen isotopes viz. deuterium and tritium (Eq. 1.1) is the most probable reaction at attainable temperatures in fusion reactors. The total energy released by this fusion reaction is 17.6 MeV, which is composed of the kinetic energy of the alpha particle ($_2He^4$) of 3.5 MeV and the neutron ($_0n^1$) of 14.1 MeV. The resulting fusion energy is about 10^6 times greater than that of the chemical processes. About 30 million kWh of electrical energy can be obtained from 1 kg D-T reaction [4]. This is nearly equal to the energy provided by 3.5 million kg of coal or about 2.5 million liters of fuel oil. This comparison shows that the fusion is a hope for the future energy supply of the world.

1.1.1. Thermonuclear Fusion

It is necessary that atomic nuclei should come close enough for the fusion reaction. However, similar positively charged atomic nuclei exert Coulomb repelling forces, making the fusion process very difficult. The Coulomb force increases with decreasing space between the nuclei. This repulsive force has to be overcome by much more attractive nuclear force, when distance between colliding nuclei becomes lower than 10^{-14} m.

To fuse D-T nuclei against Coulomb repelling force, an average temperature of about 100 million Kelvin (~10 keV) is necessary. The resulting process is known as *"Thermonuclear Fusion"* [5]. At such high temperatures, which are far above the ionization energy of hydrogen atom of 13.6 eV, electrons separate from nuclei leading to a neutral cloud of ions and unbound electrons. This state is known as *"plasma"*.

1.1.2. Lawson Criterion

To achieve break-even condition ($Q = P_{fusion} / P_{in} = 1$), i.e., self– sustained burning plasma, critical minimum condition for fusion plasma must be satisfied, which is usually known as the "Lawson criterion" [6, 7]:

- $n_e T_e \tau_E > 5\times10^{21}\ m^{-3}.\ keV.\ s$

This states that for plasma, the product of plasma density (n_e), energy confinement time (τ_E), and electron temperature (T_e) should have a minimum required value to maintain the plasma against all losses without external input power. In other words, when this condition is satisfied, released fusion energy equals the input energy required to produce and confine the plasma. This condition can be obtained through the power balance equation at steady state.

1.2. PLASMA CONFINEMENT IN TOKAMAK

The main goal of fusion research is to make self-sustaining fusion plasma after a single injection of ignition. In the ignited plasma state, only the consumed fuels, D and T must be replenished. This high energy plasma cannot be put in the container; because no material exists that can hold up such a high temperature. Also, it is necessary to avoid any contact of fusion plasma with the reaction vessel, so that constant temperature of 100 million Kelvin is possible satisfying the Lawson criterion. The most common way to satisfy the Lawson criterion is presented by the magnetic confinement fusion (MCF) concept [8], in which hot plasma (positive nuclei and negative electrons) can be shaped and confined in circular or helical path by the magnetic force such as poloidal and toroidal magnetic fields. A device where plasma is confined in the shape of a torus using a magnetic field is referred as "**Tokamak**" (*Toroidal chamber in magnetic coils*). A schematic of Tokamak with different field coils is depicted in Fig. 1.2.

In order to confine energetic plasma particles in a Tokamak, two superimposed magnetic field viz. toroidal and poloidal magnetic fields are necessary. Out of these, toroidal field is externally applied using Super Conduction Toroidal Field Magnets whereas Poloidal Field is generated by driving current through the plasma. The ring shaped toroidal field coils (Fig. 1.2) are used to generate the toroidal magnetic field and primary transformer drives the toroidal plasma current.

The required plasma current is generated by a transformer which simultaneously provides the initial heating (*resistive heating*) of the plasma. Here, plasma is the secondary of the transformer. The poloidal magnetic field is generated by the plasma current. The resulting helical field lines are superposition of the toroidal magnetic field and poloidal magnetic field.

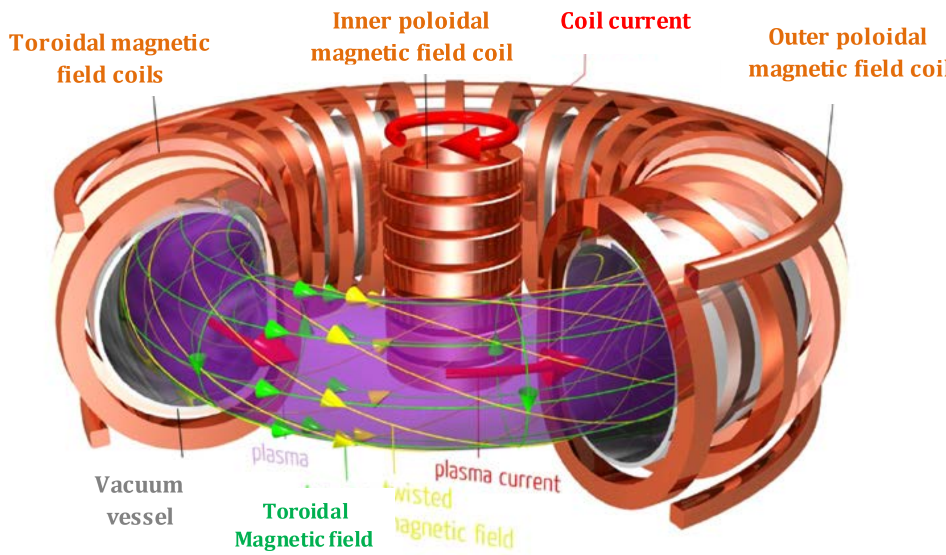

Fig. 1.2. A schematic of Tokamak with various field coils.

The Tokamak design was first introduced by the Russian scientist Basov, and since then it has become the leading magnetic confinement concept. There are various experimental Tokamak presently working, which include, DIII-D [9], JT [10], JET [11], Tore supra [12], EAST [13], MAST [14], TEXTOR [15], SST-1 [16, 17] and ADITYA [18].

The International Thermonuclear Experimental Reactor (ITER) [19, 20], is expected to reach the ignition and the state of self-burning plasma. This is an international nuclear research and engineering mega project which is scheduled to be built in France. This collaborative project is funded and run by seven participants viz. European Union, India, Japan, China, Russia, South

Korea and United States of America. A schematic diagram of ITER tokamak is depicted in Fig. 1.3. ITER tokamak will be used as a volumetric neutron source for testing materials, technologies, and components relevant for building a demonstration fusion power plant, popularly called by a generic term DEMO, which will be realized after successful operation of ITER [21]. However, there are many challenges towards successful design of the DEMO. One amongst them is the design of the "divertor" which is an important part of the fusion reactor that handles extremely high heat loads. Present thesis work is based on the efficient design of divertor for DEMO relevant conditions.

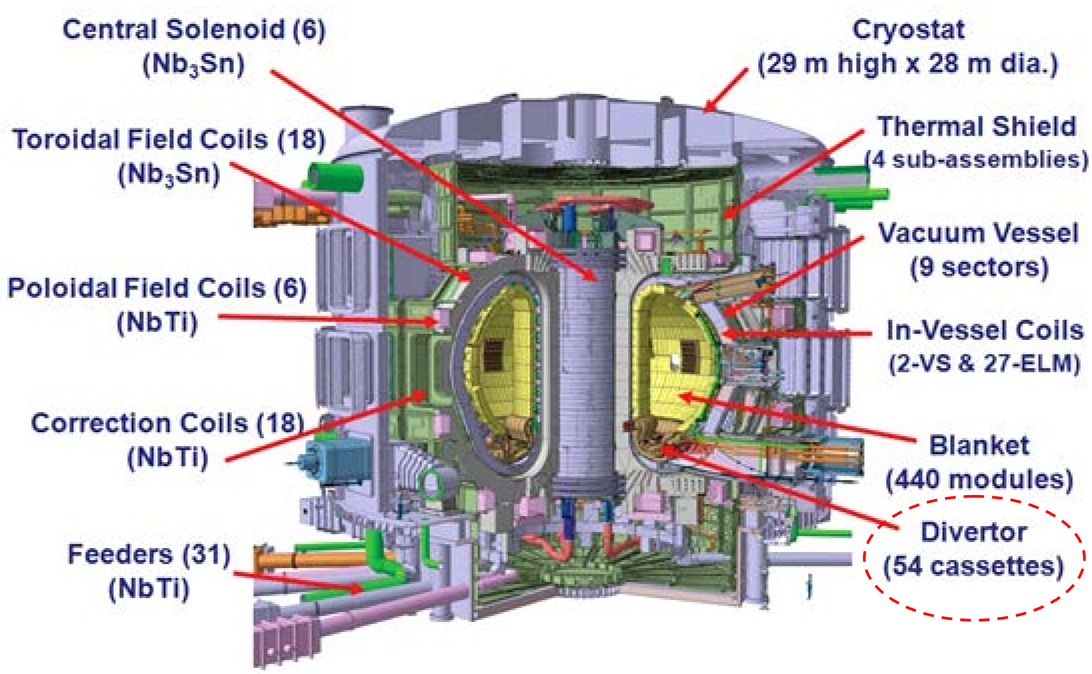

Fig. 1.3. Schematic diagram of ITER tokamak.

1.2.1. Role of Divertor and Scrape – Off Layer

The heat and particle losses from core of plasma in a tokamak occur during its transport in the parallel and perpendicular directions to the magnetic field structures confining it in the tokamak.

This leads to strong plasma-wall interactions, resulting in large erosion/damage of the walls. During the operation of a fusion reactor, fusion reaction ash, unburnt fuel and eroded particles from the reactor wall appear in the plasma. These products reduce the quality of the plasma and hinder further fusion reactions.

It is practically not possible to remove the particle fluxes emanating from the plasma. Therefore, in order to maintain the quality of plasma, the **"**divertor**"** concept has been introduced. This technique involves use of magnetic field lines to divert the particle fluxes emanating from the plasma into a separate region called as the divertor region. The charged particles approaching the wall are then swept out of the plasma into a divertor region where they are finally incident upon a divertor collector plate and become neutralized [22].

Due to the presence of divertor, tokamak plasma is divided into two regions, namely main plasma and Scrape-Off Layer (SOL) plasma as depicted in Fig. 1.4. The main plasma is the relatively hot plasma, which is confined in the closed magnetic field line structures arising due to toroidal and poloidal magnetic fields. The last closed magnetic field line is known as Separatrix or Last Closed Flux Surface (LCFS). In the divertor Tokamak, the LCFS is decided by the magnetic field. The plasma outside the LCFS travel along the open magnetic field lines known as a Scrape-Off Layer. Here, the open field lines are the field lines which touch some material surface. The SOL plasma works as an interface between the main confined plasma and the material surface of wall. It has the major role in deciding the main plasma purity and confinement times. The energy losses are compensated with the help of auxiliary heating using various schemes like Neutral Beam Injection (NBI), Lower Hybrid Current Drive (LCHD), and Ion Cyclotron Resonance Heating (ICRH) etc. Subsequently, in the ideal case, the alpha particle

($_2He^4$) generated during fusion reaction alone can cover all the energy losses and maintain the ignition temperature of plasma without auxiliary heating.

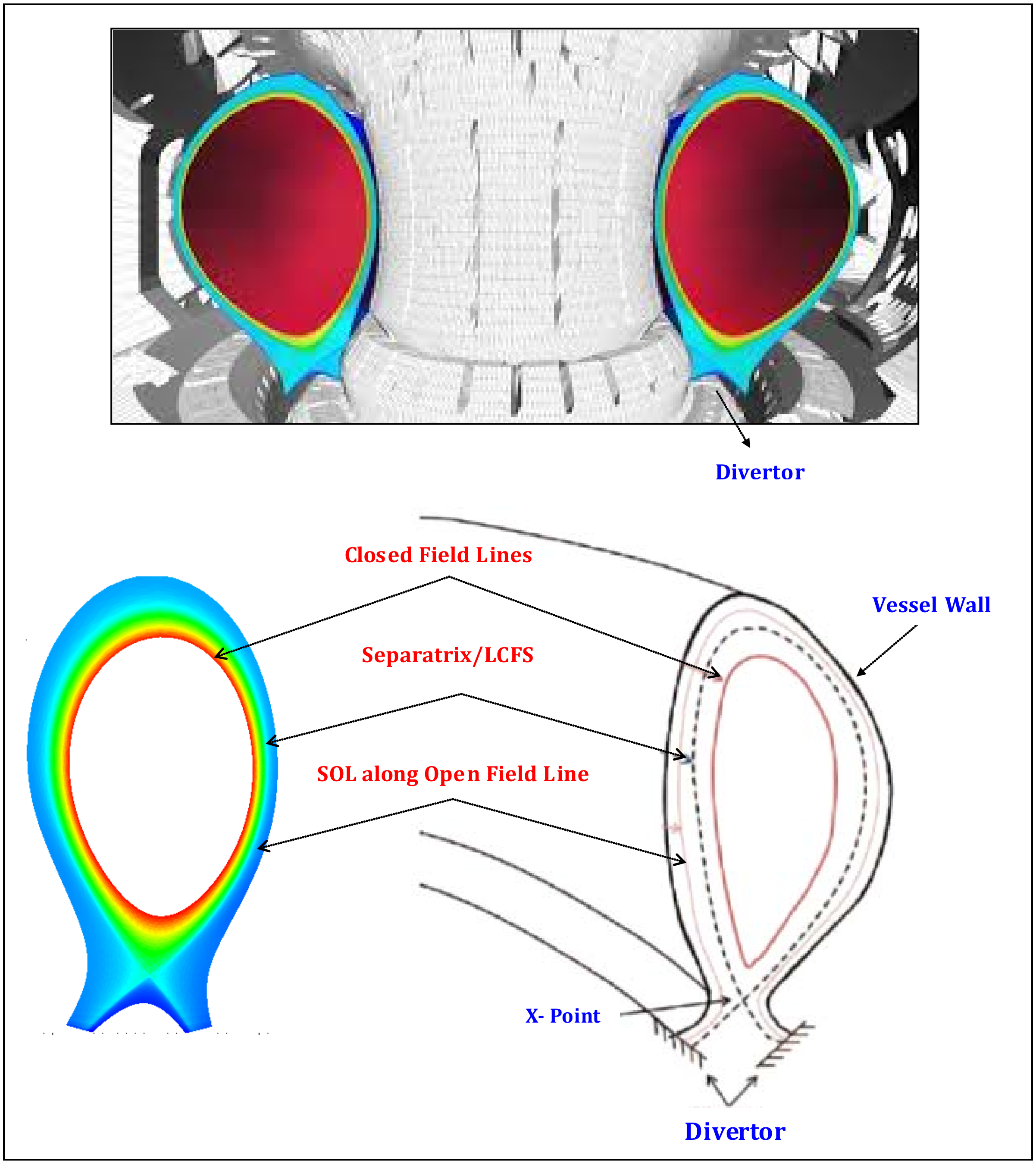

Fig. 1.4. Schematic of various regions of plasma.

1.3. FUNCTION OF DIVERTOR

Divertor is one of the integral parts of the fusion reactor that handles extremely high heat and particle flux escaping from the hot core plasma region along SOL as discussed. A significant fraction (~15%) of the total thermal power gained from the fusion reaction is removed by the divertor coolant. Hence, divertor has to face peak surface heat flux of the order of 10 MW/m² on a comparatively small target surface [23].

The use of divertor design in tokamak was intensively studied in the experimental tokamak devices such as ASDEX [24]. Divertor experiments have demonstrated decisively that the impurity content of plasma can be considerably reduced by magnetic divertor that also leads to improved energy confinement time. This shows that with the help of the divertor, plasma isolation resulting in clean plasmas can be achieved. This made the divertor to be a vital component of modern tokamaks. Following are the main functions of the divertor:

- *Remove heat energy deposited by plasma*: The divertor target surface has to manage large heat flux incident from plasma along SOL. This high heat energy is carried out by the cooling fluid flowing through the divertor system. Possibility of recycling the absorbed heat energy in the power-conversion system could significantly improve the thermodynamic efficiency of fusion power plants.

- *Reduce impurity content*: It removes the unburnt fuel, eroded particles, and helium ash from the reactor with the help of a vacuum pump. This is extremely important to extract the impurities from the plasma, which adversely affects the quality of plasma. These impurities are pumped out from the reactor to avoid dilution of fusion fuel.

1.3.1. Detailed Design of Divertor

The entire divertor system is toroidal divided into a number of modules known as *"Cassettes"* for improved handling, assembly/dis-assembly, repair, and maintenance as shown in Fig. 1.5a. Each cassette consists of plasma facing component (PFC) or divertor target with respective support structures and coolant supply network. These are the inner vertical target, outer vertical targets, and the dome. Openings have been given in the dome for extraction of the abraded particles from the reactor with the help of the vacuum pump.

The target plates are positioned with a certain angle to the magnetic field lines of SOL along which the plasma particles with high kinetic energy are incident on to the targets. Due to this high heat flux, thermo-mechanical stresses induced in the divertor target will also be high. Therefore, plasma-facing components are fabricated with numerous small cooling **"**fingers mock-up" to reduce the stresses as depicted in Fig 1.5b. Each individual module is combined with 8 others to form a 9-finger module that uses a common inlet and outlet for helium coolant. Several of these 9-finger modules are attached to a long hexagonal manifold to form a stripe-unit. Finally, each stripe unit is aligned with other units to form the target plate for the divertor [25]. The detailed design of finger mock-up is explained in Chapter 3.

In the perspective of future fusion reactor, it is desirable to explore an efficient cooling technology for divertor, which can withstand design loads and maintain the design stresses. This thesis work deals with an *efficient heat removal design concept for magnetic fusion energy power plant based on the Tokamak design.*

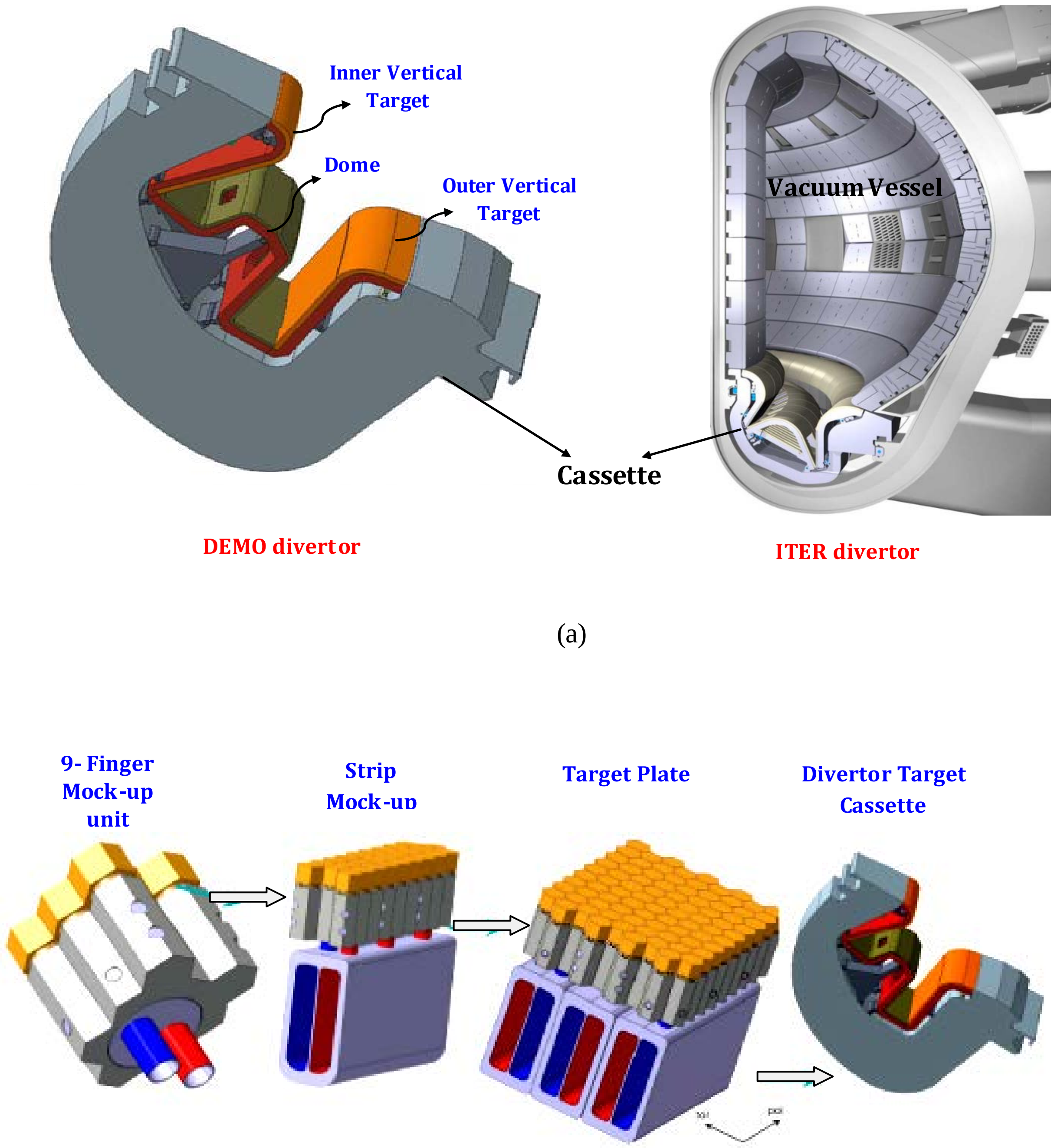

Fig. 1.5. Schematic of divertor (a) cassette and (b) finger mock-up.

1.3.1.1. Selection of Divertor Material

As explained above, the divertor targets are located at the intersection of magnetic field lines where the high-energy plasma particles hit the components. These charged and neutral particles lead to physical and chemical sputtering of plasma facing surface. Therefore, critical attention is paid to selection of the materials for divertor. The material used for the PFC should have following properties to deal with very high thermal and structural loads:

- It should be light enough to decrease pollution of the core plasma,
- Non-reactive with plasma species to avoid generation of volatile products,
- Thermal conductivity should be high for efficient heat transfer,
- Highly resistant to thermal shocks,
- Highly resistant to erosion processes,
- Low activation and short-life products under neutron irradiation

Unfortunately, no single material exists which consists of all the above properties. Therefore, a combination of three materials was introduced in the ITER design [26-28]. The first wall will be enclosed with Beryllium (Be) tiles, while Tungsten (W) will be used for the divertor. The use of Carbon Fibre Composite (CFC) material is originally proposed for the strike point region of divertor because of its very good thermal shock resistance. However, the most significant drawback of CFC is the very large sputtering and co-deposition of tritium with eroded particles (large inventory). Therefore, tungsten is the preferred choice to be used as plasma facing material for covering the entire surface of DEMO divertor target due to its excellent thermo-physical properties and plasma compatibility. The following are the main reasons to use tungsten as plasma facing material for divertor:

- High melting point,
- Low thermal expansion coefficient,
- High thermal conductivity,
- Low activation and sputtering rate,
- High thermal shock resistance

1.3.1.2. Choice of Cooling Fluid

Water is being used as coolant for present day tokamak as well as ITER. However, other coolant options are also being studied for the fusion reactor, which include liquid metal and helium [29]. At first, water was considered as an apparent option for cooling divertor, due to its high thermal conductivity and availability. However, there are some issues with the use of water in fusion reactors, which are following [30]:

- The use of water as a coolant poses a major safety hazard, because it reacts with the vessel material beryllium forming hydrogen which is explosive.
- In the case of the hydrolysis of a lithium-containing material, very acidic lithium hydroxide (LiOH) can be created which has a melting point of 470 °C and it is well below a typical operating temperature of fusion reactor.
- The main disadvantage of water arises from the need to avoid phase change and the associated critical heat flux.

Use of liquid metal as a coolant has disadvantages due to electromagnetic forces experienced by the fluid in presence of the background magnetic field resulting in unwanted changes in fluid flow. On the other hand, the use of helium as coolant is promising option for divertor of fusion reactor, because it has favorable safety characteristics and helium can be used at very high temperatures. Hence, it can be used directly for gas turbine cycle power conversion systems. Following are the main advantages of helium for use as a divertor coolant [30-31]:

- Chemically and neutronically inert,
- Non-magnetic and non-conductive,
- No induced radioactivity,
- No phase changes,
- Negligible gravity effects,
- Thermal and radiation stability,

1.5. THERMAL HYDRAULIC ISSUES AND DESIGN LIMITATION FOR DIVERTOR

In DEMO, helium gas is preferred as a coolant in “finger” type divertor targets as it offers several advantages, including chemical and neutronic inertness and ability to operate at higher temperature and pressures. However, also have certain disadvantage such as its comparatively poor heat exchange capability and considerably large pumping power requirement. In the context of DEMO, it is desirable to explore efficient cooling technology for helium cooled divertor, which can withstand high heat loads. There are certain design requirements and constraints for the helium cooled divertor as follows:

- The design should be able to withstand high heat load conditions, i.e, the steady state heat flux of ~ 10 MW/m^2.
- Heat conduction paths from plasma facing side to the cooling surface must be short enough to maintain the maximum temperature of the structural material below its recrystallization temperature.
- The temperature range of tungsten is restricted to lower limit of ductile-to-brittle transition temperature (DBTT ~ 600 °C), below which it loses its ductility with the risk of material failure. At the upper limit, the temperature is limited by the recrystallisation temperature (RCT = 1300 °C), above which tungsten loses its thermal fatigue strength due to grain coarsening.

- The design should be efficient, so that the pumping power of helium at the necessary pressure, temperature and flow rate through the divertor target should not exceed 10% of the total thermal energy absorbed.
- Stresses induced in the divertor as a result of large temperature gradients and high pressures are important factors that limit the performance and life of the divertor. The total stresses induced in the divertor must be lower than the allowable stress limit.

1.6. LITERATURE REVIEW

The technology necessary to actively cool divertor for removal of heat fluxes of ~ 10 MW/m^2 is a complex task, and the divertor designs that have been devised thus far utilize many advanced concepts. The cooling requirements alone present a challenge and are further complicated by the restriction of materials and coolants due to the high neutron fluences inside a fusion reactor. However, scientists and engineers from many different countries have managed to propose some possible solutions each at varying stages of development. This section presents an overview of the experimental and numerical investigations carried out by the various researchers for the helium cooled divertor and basic heat transfer enhancement concepts.

1.6.1. Experimental and Numerical Studies for Divertor

The concept of the fusion-fission hybrid reactor is reviewed by Schultz [32]. In his review, he summarized that helium gas is attractive as a coolant for hybrid systems because helium is chemically inert, nonmagnetic and nonconductive, which greatly reduces materials compatibility concerns. The challenges and the design issues associated with the helium cooling, viz., manifold sizes, pumping power, and leak prevention are studied by Baxi [33]. It was demonstrated that, the manifold sizes and the pumping power can be reduced to acceptable levels as per the design criteria. Baxi and Wong [34] reviewed various heat transfer enhancement techniques (viz., swirl tape, roughening, porous media etc.) to reduce the flow, pumping power and pressure requirements in helium cooling for fusion reactor applications. Various cooling technologies for future fusion power plants were studied by Ihli and Ilić [35]. Among different cooling technologies, V-rib based surface roughness approach for the first walls with multiple impingement cooling techniques were identified as a suitable method. Tillack et al. [30] summarized the various technical challenges resulting from the choice of water as a coolant and the differences in approach and assumptions that lead to different design decisions amongst researchers in the fusion field.

A comparative assessment of various helium cooled divertor concepts (Porous, Multichannel, Slot and Eccentric swirl concept) was performed by Hermsmeyer et al. [36]. They found that all the proposed designs are capable to handle only up to ~5 MW/m^2. Thermal performance and flow instabilities in multi-channel helium-cooled porous metal divertor modules were analyzed by Youchison et al. [37]. The module was tested for uniform heat loads to assess the effects of mass flow instabilities, and it was found that the design can survive heat flux ~5 MW/m^2. Gayton et al. [38] investigated the heat transfer and friction characteristics in a plate type divertor. They predicted that the thermal performance of the divertor increases with the use of metallic foam, but implementation of foam and pressure drop in the design are of main concerns. Effect of fins on the heat transfer coefficient of plate-type divertor was investigated by Hageman et al. [39]. The results suggested that, adding fins nearly doubles the effective heat transfer coefficient. To enhance the heat transfer and reduce the thermal stresses in order to accommodate a high heat flux, a design optimization of divertor plate concept was performed by Wang et al. [40]. It was found that, the concept can handle a peak heat flux of close to ~10 MW/m^2 while accommodating the temperature, stress and pumping power constraints.

High Efficiency Thermal Shield (HETS) concept that relies on an abrupt change of momentum of the fluid was proposed by Pizzuto et al. [41] and Eliseo et al. [42]. The numerical studies along with experiments indicate that HETS solution is viable in order to attain a good heat transfer with limited pumping power. Karditsas [43] investigated the effect of the geometry variation on the thermal hydraulic performance of HETS divertor concept. The computational simulation shows that the combination of rounding the sharp corner and expanding flow cross-sectional area leads to reduced pressure losses without any degradation in the thermal performance of the component.

An overview of the development of different concepts for a fusion power plant alog with advantages and disadvantages as well as expected performance was discussed by Norajitra et al. [44]. Furthermore, they summarized the status and progress of R&D associated with He-cooled divertor designs which have been proposed in most of conceptual plant models in Europe and USA. A modular helium cooled divertor for power plant application was studied by Diegele et al. [45] with an improved heat transfer technique. The result showed that the design has the potential of removing high heat flux up to ~10 MW/m^2. An advanced helium cooled divertor concept was studied by Ihli et al. [46] with modular target plate design through computational fluid dynamics simulations. The authors achieved promising cooling performance of the modular divertor system with jet impingement technique. Validation of the CFD tools for the development of a helium-cooled divertor was performed by Kruessmann et al. [47]. They found that simulated and measured results were in satisfactory agreement. Končar et al. [48] investigated the effect of nozzle diameter on the thermal performance of helium cooled divertor. The predicted result shows that equal sized nozzle decreases the highest thimble temperature. Thermal stress is regarded as an important limit for performance of the fusion power plants.

Toward this, Widak and Norajitra [49] numerically investigated the thermo-mechanical aspect through a finite element approach. Norajitra et al. [50-52] and Aktaa et al. [53] reported the progress of He-cooled divertor, current status of divertor development and manufacturing technologies for modular divertors. Thermal hydraulic characteristics of fusion reactor components were analyzed by Arbeiter et al. [54] through various turbulence models using CFD code STAR–CD, and the results were validated against experiments. It is seen that, k–ε turbulence model gives accurate results for high heat flux test module.

1.6.2. Basic Heat Transfer Enhancement Concepts

Many experimental and numerical studies have been reported in the open literature to investigate the heat transfer enhancement and fluid flow characteristics of extended surface. The focus of these studies has been to achieve a high surface area to volume ratio, a large convective heat transfer coefficient, and a minimum volume of coolant inventory. Yuan et al. [55] investigated the potential of a plate pin fin heat sink for electronics cooling. The predicted result shows that pin height and air velocity have significant influences on the thermal hydraulic performances. Numerical simulation of flow and heat transfer of fin structure in air-cooled heat exchanger has been investigated by Li et al. [56]. It was found that the air-side heat flux and heat transfer coefficient increase sharply for the wavy fin arrangement. Shafeie et al. [57] numerically investigated the effect of micro channel and pin fin on the thermal performance of heat sinks. It was observed that, heat removal capability of the finned heat sinks is lower than that of the micro-channel for an identical pumping power. A fan-shaped pin fin in a rectangular channel was analyzed by Moon et al. [58] and their studies revealed that, fan-shaped pin fin showed an improved Nusselt number (Nu) compared to a circular pin fin, at Reynolds number (Re) less than 100,000. On the other hand, the pressure drop in the channel with the fan-shaped pin fin was marginally less small than that with the circular pin fin. The heat transfer enhancement characteristics of wavy fin-and-flat tube heat exchangers have been analyzed by Dong et al. [59]. They found that, wavy fin with large waviness amplitude can provide a high heat transfer coefficient. A numerical study on the heat transfer enhancement with interrupted annular groove fin was performed by Lin et al. [60]. Their results reveal that, interrupted annular groove has a dual effect on fluid flow, guiding and detached eddy inhibition to reduce the size of the wake region.

Experimental studies on staggered and in-line pin fin arrays installed in an internal cooling channel were performed by Fossen [61] and Sparrow et al. [62]. It was found that the heat transfer coefficient and pressure drop for the in-line array are lower than those for the staggered array. A novel heat transfer enhancement technique was evaluated by Collins et al. [63]. In their studies, they showed that the use of wire-coil significantly increases the heat transfer at reasonably low flow rates, and hence pumping power. The flow and heat transfer performance in a channel with dimples has been studied by Moon et al. [64], Mahmood and Ligrani [65], and Mahmood et al. [66]. Their studies revealed that by providing dimple on the surface can enhance the Nusselt number compared to a smooth surface by a factor of 1.8 – 2.8. Thermodynamic analysis of heat and fluid flow in a micro channel with internal fins and optimization study has been performed by Narayanaswamy et al. [67, 68]. Based on the numerical study, they concluded that internal fins in a micro channel have the potential to provide heat transfer augmentation.

1.7. MOTIVATION FOR THE PRESENT RESEARCH

From the existing literature, it is observed that manufacturing difficulties, high heat flux removal capabilities and high pressure drop associated with helium cooled divertor design are of main concerns during the design, fabrication and implementation. It is also found that the heat transfer enhancement is an active area of current research and currently a few international research groups are working on it to address the heat transfer enhancement for DEMO relevant divertor systems. Moreover, designs for DEMO proposed by the researchers for accommodating the design loads (10 MW/m^2) are very few in numbers and without much experimental validation studies. These form the motivation for the present work. Following are the main issues considered and addressed in the present thesis work:

- Finger type design is considered for the present work due to its smaller size that results in reduction of thermo-mechanical stresses due to high pressure and temperature gradients.
- In the present work, fabrication has been simplified to a great extent by choosing sectorial extended surfaces that can be simply machined out of a solid cylinder using available machining processes like Electrode Discharge Machining, Water jet Cutting or Milling.
- Efforts are made to achieve steady state heat flux removal capability of 10 MW/m^2 while maintaining temperature on tungsten within allowed window limits. Design configuration and operating parameters are optimized for maintaining pumping power (i.e., efficiency of heat transfer for given input parameters) within acceptable limit of 10%.
- In order to validate the computational design, an experimental setup is established, test mock-ups are fabricated and experiments have been performed. Efforts are made to simplify the experimental requirements by using appropriate equivalent conditions without compromising on technical details. Both heat transfer and pressure drop have been measured in the experiment as a function of Reynolds number. Based on the experimental work, correlations have been derived for Nusselt Number (Nu) and Pressure Loss Coefficient (K_L) in the finger mock-up as a function of Reynolds number.
- In addition to the above work on “finger” type concept, an innovative divertor heat sink concept is also proposed and numerically investigated to handle the design load at the acceptable pumping power limit for the divertor target of fusion reactor. However, its design validation is not done during the present work. Experimental design validation of divertor heat sink can form part of the future studies.

1.8. OBJECTIVES AND SCOPE OF THE PRESENT WORK

The objective of the present thesis is to develop computational and experimental models of helium cooled divertor target for prediction of heat transfer and pressure drop characteristics for the proposed DEMO reactor. The scope of the present thesis work is as follows:

- To perform detailed numerical studies for evaluation of thermal-hydraulic performance of the "finger" type design and develop the possible conceptual design for divertor target.
- To carry out in-house experimental and numerical investigations to validate the thermal hydraulic performance of the "finger" type divertor design.
- Identification and development of appropriate heat transfer enhancement techniques for the existing "finger" type design.
- To understand the effects of various geometric parameters on the thermal-hydraulic performance so as to find an optimum solution to divertor design.
- To carry out the thermo-mechanical analysis using finite element method based computational tools to verify practicability of the design.

1.9. OUTLINE OF THESIS WORKS

Thesis work is divided in total seven chapters as follows:

- First chapter gives an introduction to the helium cooled divertor, thermal hydraulic issues and limitations. It also includes the literature survey, motivation and objective of the thesis work.
- Second chapter describes the numerical approach used for the present simulations.
- Third chapter describes a heat transfer enhancement design for divertor finger mock-up and associated numerical investigations.
- Fourth chapter describes the experimental and numerical verification of the proposed design for divertor, using a full scale model with air as the coolant.
- In the fifth chapter, the proposed design has been optimized to enhance the thermal hydraulic performance of divertor.

- In the sixth chapter, an efficient divertor heat sink concept is proposed and detailed numerical study has been performed to understand the thermal hydraulic performance of divertor heat sink.
- Conclusions and future scope of work are presented in the seventh chapter.

CHAPTER 2

MATHEMATICAL MODEL AND GOVERNING EQUATIONS

2.0. INTRODUCTION

This chapter deals with a brief introduction to Computational Fluid Dynamic (CFD) model, techniques used for solving thermal fluid flow problems, governing equations for fluid dynamics, turbulence model and boundary conditions used to determine fluid flow and heat transfer in the helium cooled divertor. It is known that fluid dynamics is the science of fluid motion. The studies of thermal fluid flow problems are possible by three different methods, viz., experimental, theoretical and numerical. The numerical route is known as Computational Fluid Dynamics (CFD). The CFD consists of three elements known as (i) pre-processor, (ii) solver and (iii) post-processor [69]. Pre-processor consists of inputs of the flow problem to a CFD program by means of an operator friendly Graphical User Interface and the subsequent transformation of this input into a form suitable for use by the CFD solver.

The region of the fluid to be analyzed is called the "computational domain" and it is made up of a number of discrete volumes known the "mesh" or "grids". After mesh generation, the properties of fluid and appropriate boundary conditions are specified. The solver completes the solution of the CFD problem by solving the governing equations. The governing equations are in the form of Partial Differential Equations (PDE) made up of combinations of flow variables and their derivatives. The solver converts the PDEs into a system of algebraic equations employing finite difference, finite volume or finite element method. This process is known as "numerical discretisation". The various methods of discretisation are described in Fig. 2.1. Post-processor is used to visualize and process the results from the solver part quantitatively. The present thesis work is based on the finite volume method using the commercial CFD software package ANSYS FLUENT 14.0 [70].

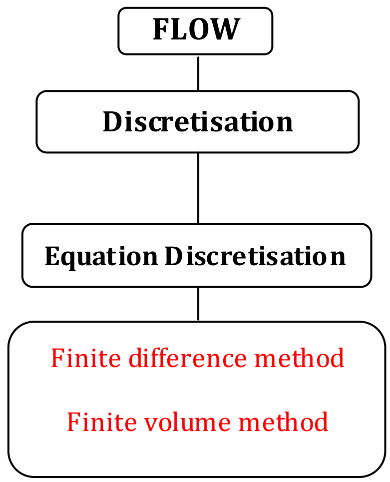

Fig. 2.1. Various discretization methods.

2.1. GOVERNING EQUATIONS

Combining the fundamental principles, the physics of fluid flow is expressed in terms of a set of partial differential equations known as Navier-Stokes equations given by famous French engineer Claudia Navier and the Irish mathematician George Stokes. These equations are derived from fundamental principles of fluid dynamics known as: (1) continuity equation, (2) momentum equation, and (3) energy equation. These equations represent the conservation laws of physics. The steady state forms of continuity, momentum, and energy equations for an ideal gas fluid used for the present numerical simulation. The following equations describe the steady state fluid flow and heat transfer process of a fluid [71]:

- Continuity equation:

$$\frac{\partial(\rho u_i)}{\partial x_i} = 0 \tag{2.1}$$

❖ Momentum equation:

$$\frac{\partial(\rho u_j u_i)}{\partial x_j} = -\frac{\partial P}{\partial x_i} + \frac{\partial}{\partial x_j}\left(\mu_{eff}\frac{\partial u_i}{\partial x_j}\right) \tag{2.2}$$

❖ Energy equation:

$$\frac{\partial(\rho C_p u_i T)}{\partial x_i} = \frac{\partial}{\partial x_i}\left(K_{eff}\frac{\partial T}{\partial x_i}\right) \tag{2.3}$$

In a solid medium, the heat conduction equation for steady state temperature field is given by:

❖ $$\frac{\partial}{\partial x_i}\left(\lambda s \frac{\partial T}{\partial x_i}\right) = 0 \tag{2.4}$$

In the above equation $\mu_{eff} = \mu_l + \mu_t$ and $K_{eff} = K_l + K_t$, where μ_l and K_l are respectively molecular viscosity and molecular thermal conductivity of the fluid. Similarly, μ_t and K_t are respectively turbulent viscosity and turbulent conductivity, and λ_s is the thermal conductivity of solid. Furthermore, turbulent viscosity (μ_t) and turbulent conductivity (K_t) of fluid are described by:

- $\mu_t = \rho C_\mu k^2/\varepsilon$ (2.5)

and

- $K_t = \mu_t C_p/P_{rt}$ (2.6)

Where the symbols have their usual meanings and are described in the "Nomenclature" section at the end of the thesis.

2.2. AN OVERVIEW OF TURBULENCE MODEL

Flow can be laminar or turbulent depending on the fluid flow conditions reflected through Reynolds number. For engineering applications, most flows are turbulent in nature. Flow in the turbulent regime contains eddies with different sizes which are always rotational in motion and are responsible for carrying energy and momentum in the flow. The smallest scale eddies, where dissipation of energy occurs are known as the *"Kolmogorov scale eddies"*. The length scale of these eddies are smaller than the lengths of engineering interest. In spite of their tiny sizes, the eddy Reynolds number of turbulent motion is of the order of unity, suggesting that even the smallest eddy obeys the continuum hypothesis [72]. Larger eddies extract energy from the mean flow and transfer it to the smaller eddies where energy is taken out through viscosity which is known as the *"Richardson's cascade"*. Currently available computer power is not yet sufficient to resolve the smaller eddies. So turbulence models are generally based on some simplified assumptions. An overview of turbulence model used in the study is explained in the subsequent section.

2.2.1. The Standard k-ε Model

The k-ε turbulence model solves the flow equations based on the main assumption that the rate of production and dissipation of turbulent flows are in near balance in energy transfer. The dissipation rate (ε) of the energy is written as [73],

- $$\varepsilon = \frac{k^{3/2}}{L} \tag{2.7}$$

where 'k' is the turbulent kinetic energy and 'L' is length scale.

The turbulent viscosity μ_t is related to k and ε as given in Eq. 2.5, where 'C_μ' is an empirical constant. The transport equations for the turbulent kinetic energy (k) and its dissipation rates (ε) are:

$$\frac{\partial}{\partial x_i}(\rho u_i k) = \frac{\partial}{\partial x_j}\left[\left(\mu + \frac{\mu_t}{\sigma_k}\right)\frac{\partial k}{\partial x_j}\right] + G_k - \rho\varepsilon \qquad (2.8)$$

The equation for ε is,

$$\frac{\partial}{\partial x_i}(\rho u_i \varepsilon) = \frac{\partial}{\partial x_j}\left[\left(\mu + \frac{\mu_t}{\sigma_\varepsilon}\right)\frac{\partial \varepsilon}{\partial x_j}\right] + C_{\varepsilon 1}\frac{\varepsilon}{k}G_k - \rho C_{\varepsilon 2}\frac{\varepsilon^2}{k} \qquad (2.9)$$

where G_k represents the generation of turbulent kinetic energy the arises due to mean velocity gradients. Based on an extensive examination of a wide range of turbulent flows, the constant parameters used in the equations take the following values [74]:

$C_\mu = 0.09$, $C_{\varepsilon 1} = 1.44$, $C_{\varepsilon 2} = 1.92$, $\sigma_k = 1.0$, and $\sigma_\varepsilon = 1.3$

The term for the production of turbulent kinetic energy G_k is common in many of the turbulence models studied and is defined by,

$$G_k = -\rho\,\overline{u'_i u'_j}\frac{\partial u_j}{\partial x_i} \qquad (2.10)$$

2.2.2. The Realizable k-ε Model

The second model is Realizable k-ε, an improvement over the standard k-ε model. It is a relatively recent development and differs from the standard k-ε model in two ways. It uses a new equation for the turbulent viscosity and the dissipation rate transport equation has been derived from the equation for the transport of the mean-square vortices fluctuation. The term "realizable" means that the model satisfies certain mathematical constraints on the Reynolds stresses, consistent with the physics of turbulent flows. This is not satisfied by the standard k-ε models which make the realizable model more precise than standard models at predicting flows such as separated flows and flows with complex secondary flow features. In terms of the improved changes the transport equations become:

- $$\frac{\partial}{\partial x_j}(\rho u_i k) = \frac{\partial}{\partial x_j}\left[\left(\mu + \frac{\mu_t}{\sigma_k}\right)\frac{\partial k}{\partial x_j}\right] + G_k - \rho\varepsilon \qquad (2.11)$$

- $$\frac{\partial}{\partial x_j}(\rho u_j \varepsilon) = \frac{\partial}{\partial x_j}\left[\left(\mu + \frac{\mu_t}{\sigma_\varepsilon}\right)\frac{\partial \varepsilon}{\partial x_j}\right] + \rho C_1 S\varepsilon - \rho C_2 \frac{\varepsilon^2}{k + \sqrt{v\varepsilon}} \qquad (2.12)$$

Similar to the previous the k-ε models, the turbulent viscosity is determined by the formula given below; however it produces different results as C_μ is

- $$\mu_t = \rho\, C_\mu \frac{k^2}{\varepsilon} \qquad (2.13)$$

where C_μ is computed from

$$C_\mu = \frac{1}{A_0 + A_s \frac{kU^*}{\varepsilon}} \qquad (2.14)$$

where

$$U^* = \sqrt{S_{ij}S_{ij} + \tilde{\Omega}_{ij}\tilde{\Omega}_{ij}} \qquad \tilde{\Omega}_{ij} = \bar{\Omega}_{ij} - \varepsilon_{ijk}\omega_k - 2\varepsilon_{ijk}\omega_k$$

In the above equation, $\bar{\Omega}_{ij}$ is the mean rate of rotation tensor viewed in a rotating reference frame with angular velocity ω_k. The constants A_0 and A_s are defined as;

$$A_0 = 4.04\ , \qquad A_s = \sqrt{6}\cos\phi$$

where

$$\phi = \frac{1}{3}\cos^{-1}\left(\sqrt{6}\frac{S_{ij}S_{jk}S_{ki}}{\tilde{S}^3}\right)\cos\phi, \qquad \tilde{S} = \sqrt{S_{ij}S_{ij}}, \qquad S_{ij} = \frac{1}{2}\left(\frac{\partial u_j}{\partial x_i} + \frac{\partial u_i}{\partial x_i}\right)$$

It has been shown that C_μ is a function of the mean strain and rotational rates, the angular velocity of the rotating system, and the turbulent kinetic energy and its dissipation rate. The standard value of $C_\mu = 0.09$ is found to be the solution of equation 2.14 for an inertial sub layer in the equilibrium boundary layer. The values of constants determined by experiment are follows.

$C_2 = 1.9$, $\sigma_k = 1.0$, and $\sigma_\varepsilon = 1.2$

where C_1 is determined by,

$$C_1 = \max\left[0.43, \frac{\eta}{\eta+5}\right], \quad \eta = S\frac{k}{\varepsilon}, \quad S = \sqrt{2S_{ij}S_{ij}}$$

The k-ε model has gained popularity among RANS models due to

- Accurate prediction of the performance for separation, recirculation, and flows involving boundary layers under pressure gradients
- Robust formulation
- Widely documented and reliable
- Lower computational overhead

2.3. BOUNDARY CONDITIONS

The governing equations are elliptic in space coordinates and hence the boundary conditions for velocity components, k and ε are needed to be specified on all the boundaries. For the solution of non-linear equations, solution variables (φ) are to be specified with an initial condition to start the iteration. The velocity components are zero on solid walls (no-slip condition) and φ are to be mentioned at inflow boundary. At outlet, specified pressure or outflow boundary condition

$\left(\frac{\partial u_i}{\partial n}=0\right)$ is to be specified. Furthermore, symmetric boundary condition $\left(\frac{\partial \phi}{\partial n}=0\right)$ is applied to take advantage of special geometrical features of the solution region.

For turbulent flow simulations, the standard practice is to use wall functions [75] close to the wall, where values of the variables change sharply. This is required to avoid excessive grid refinement and associated high computational effort [72]. The details of boundary conditions for each specific problem are discussed in the corresponding chapters.

2.4. GRID INDEPENDENCE TEST AND CONVERGENCE

In all CFD simulations, mesh independence test is an important step in order to achieve a reasonably accurate and converged solution which means a change of the mesh does not affect the numerical solutions significantly. A mesh independence test is usually done by refining mesh resolution of the simulations gradually to achieve a mesh size invariant. Another aspect in the CFD study is the residual to declare convergence of the solutions. The equations describing fluid flow are solved iteratively and hence residuals appear. A residual is usually targeted between four to six orders of magnitude less compared to the original value to achieve convergence [71] of the solution to an acceptable level.

2.5. CLOSURE

The governing equations for the ideal gas flow of helium, heat absorption of helium from solid surfaces and conduction heat transfer from solid surfaces have been presented for the conjugate conduction and convection heat transfer study. Detailed flow boundary conditions, grid independent test and the solution procedure used for the simulations are presented in the subsequent respective chapters.

CHAPTER 3

NUMERICAL STUDIES ON HELIUM COOLED DIVERTOR FINGER MOCK UP WITH SECTORIAL EXTENDED SURFACES

3.0. INTRODUCTION

As mentioned previously, cooling of fusion reactor "divertor" by helium is widely accepted due to its chemical and neutronic inertness and superior safety aspect. However, its poor thermo physical characteristics need high pressure to remove large heat flux encountered in fusion power plant (DEMO). In the context of DEMO, it is essential to look at a competent cooling technology for divertor that can handle extremely high heat flux generated in interior of the core. Towards this, a new type of "*Sectorial Extended Surface*" (SES) has been proposed. This particular design is easy to manufacture and cost effective.

As detailed in Section 1.3.1, the plasma-facing components are fabricated with numerous small sized "*finger*" shaped mock-ups cooled by helium jets to reduce the stresses caused by temperature gradients and internal gas pressure. The present study is "*focused towards finding an optimum performance of one such finger mock-up through systematic computational fluid dynamics studies. Heat transfer characteristics of finger mock-up have been numerically investigated with a sectorial extended surface*". Numerical investigations show that addition of SES greatly increases thermal-hydraulic performance of the finger mock-up. Detailed parametric studies on critical parameters that influence thermal performance of the finger mock-up have been analysed. Thermo-mechanical analysis has also been carried out through finite element based approach to know about possible stresses in the assembly as a result of large temperature gradients and gas pressure. It is seen that the stresses are within the permissible limits of materials adopted for the present design. Benchmark studies have been performed for reported other designs that are experimentally tested through high-heat flux experiments [48] and a good agreement is obtained between the present simulation results and the reported results.

3.1. SOLUTION METHODOLOGY

3.1.1. Detailed Design of Finger Mock-Up

The entire divertor of tokamak is divided into a number of modules known as “cassettes”, which are independently cooled. The plasma facing components of the divertor are split into a number of ‘finger mock-ups’ in order to reduce the thermal stress, as presented in Figs. 3.1. Each mock-up consists of small hexagonal ‘tile’ (width 17.8 mm) made up of pure tungsten (W) material with sacrificial thickness (~ 5 mm) used as the thermal shield. A hexagonal form of small segments allows a higher packing density for heat dissipation. Tiles are brazed to another material of tungsten alloy (WL-10) known as the ‘thimble’ (Ø15×1mm). Tungsten Lanthanum Oxide (WL-10) is chosen as thimble material because of its encouraging property for the machining. The motive for the separation of these two components (tile and thimble) is that any crack originating from the tile surface does not reach the thimble and is stopped at the interface.

The brazing of the tile and thimble is performed with a nickel (Ni) alloy filler metal, STEMET ® 1311 (Ni-based, 16.0 (Co), 5.0 (Fe), 4.0 (Si), 4.0 (B), 0.4 (Cr)) with a brazing temperature of 1050 ˚C. A cartridge (Ø11.2×1 mm) made up of Reduced Activation Ferritic Martensitic steel (RAFMS) carrying the nozzle is placed concentrically inside the thimble. Fluid enters through the nozzle and flows radially outwards through the space between cartridge and the thimble. These tungsten finger mock-up units are connected to the support structure by means of brazing which is preferred to be made of RAFMS [76]. Thermo-hydraulic performance of mock-up has been studied with addition of sectorial extended surfaces, which is placed between cartridge and the thimble with a supporting plate of 1 mm thickness, as depicted in Fig. 3.1(b). The circumferential pitch are varied from first row to last row that leads to reduce the expense of machining to cover the top cooled surface. Extended surfaces are angularly constructed at every 30° sector, resulting in 36 numbers of extended surfaces with 1 mm thickness, 0.8 mm pitch, and 2 mm height. Circumferential gap between the extended surfaces is maintained at 0.4 mm.

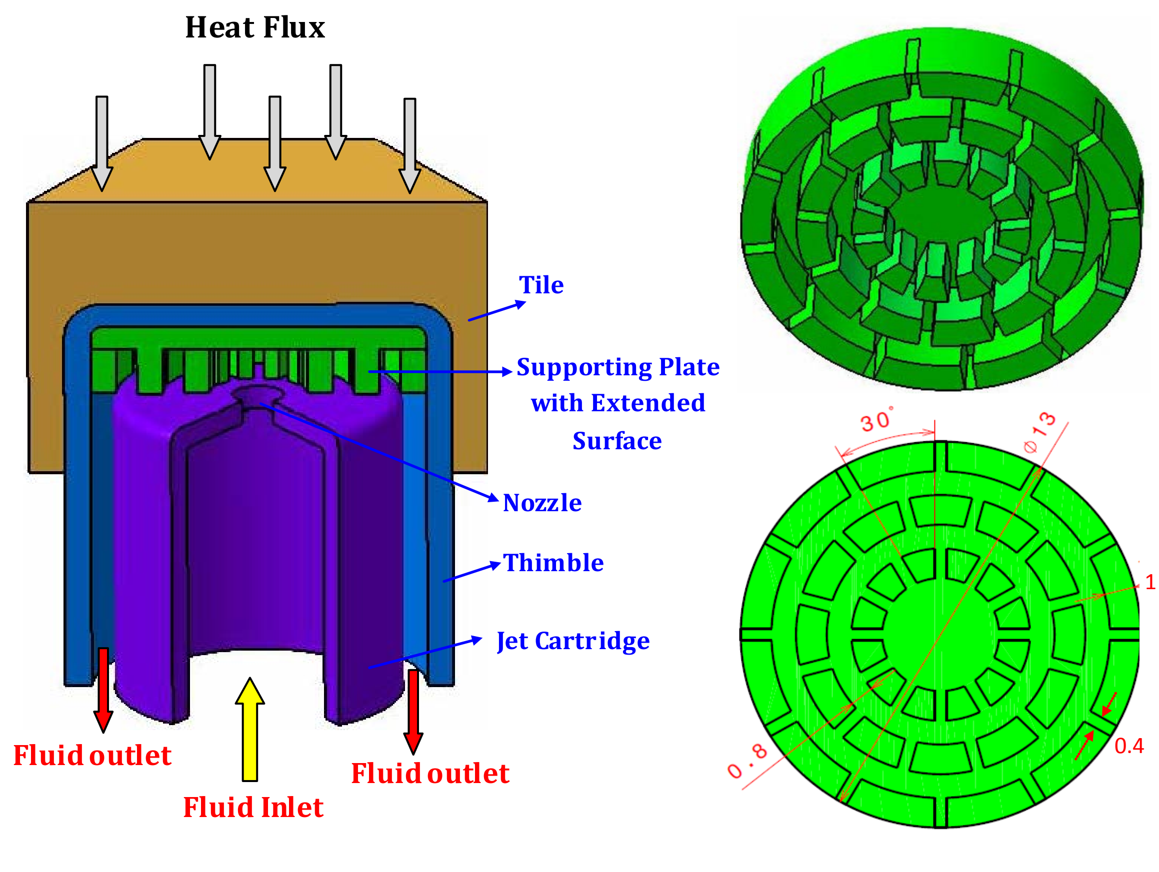

(a) (b)

Fig. 3.1. Schematic of (a) He-cooled divertor finger mock-up and (b) 3-D and close up views of SES (all dimensions in mm).

Fabrication has been simplified to a great extent by SES that can be simply machined out of a solid cylinder using typical available machining processes like Electrode Discharge Machining, Water jet Cutting or Milling. The most important design criterion is to keep thimble temperature above ductile brittle transition temperature (DBTT, ~600°C) and below re-crystallization temperature (RCT, ~1300°C). The brazing filler temperature of tiles and thimble should not exceed 1050°C [48] and pumping power should be lower than ~10 % of incident power.

3.1.2. Governing Equations

The steady state forms of continuity, momentum, and energy equations for an ideal gas fluid used for the present numerical simulation are described in Chapter 2. In the present simulation, Mach Number (M) is found to be less than 0.3 and temperature rise of helium in the divertor assembly is only about 60 K. Hence, the assumption of helium as an incompressible gas is justified. To resolve the Reynolds stresses, realizable k-ε turbulence model is employed, because it accurately predicts the performance for separation, recirculation, and flows involving boundary layers under pressure gradients [70] and also used to simulate flow and heat transfer in pin fin channel [77]. Pressure-velocity coupling between the incompressible Navier-Stokes and continuity equations is resolved using the "Semi Implicit Pressure Linked Equations" (SIMPLE) algorithm. To declare convergence at any iteration, the absolute errors in the discretization momentum and continuity equations are set to be 10^{-4} whereas for energy, it is set to be 10^{-7}.

3.1.3. Boundary Conditions

A schematic of computational model with boundary conditions is depicted in Fig. 3.2. Due to the symmetry, a 30° sector model is considered for the present numerical simulation. Temperature dependent material properties are taken into consideration for the tile, thimble, and supporting plate with extended surfaces [78] whereas constant material properties are considered for cartridge. The finger mock-up is cooled by helium jet at 10 MPa and 600 °C impinging onto the heated wall of the target surface. The inlet and outlet temperatures of the He coolant are limited by the DBTT of tungsten lanthanum oxide (600 °C) and the creep rupture strength of the RAFMS steel structure. High pressure of helium (~10MPa) has been used for efficient removal of heat from the hot target surface. The boundary conditions for the present 3D numerical simulations are as follows:

- Symmetry boundary conditions are imposed on the 30° cut sections.
- Adiabatic boundary conditions are imposed on outer sides of the domain.
- Top surface of the domain is imposed with constant heat flux (10 MW/m^2).
- Mass flow rate and temperature of He gas are specified at the inlet.
- No-slip conditions are imposed on the walls and at the extended surfaces.

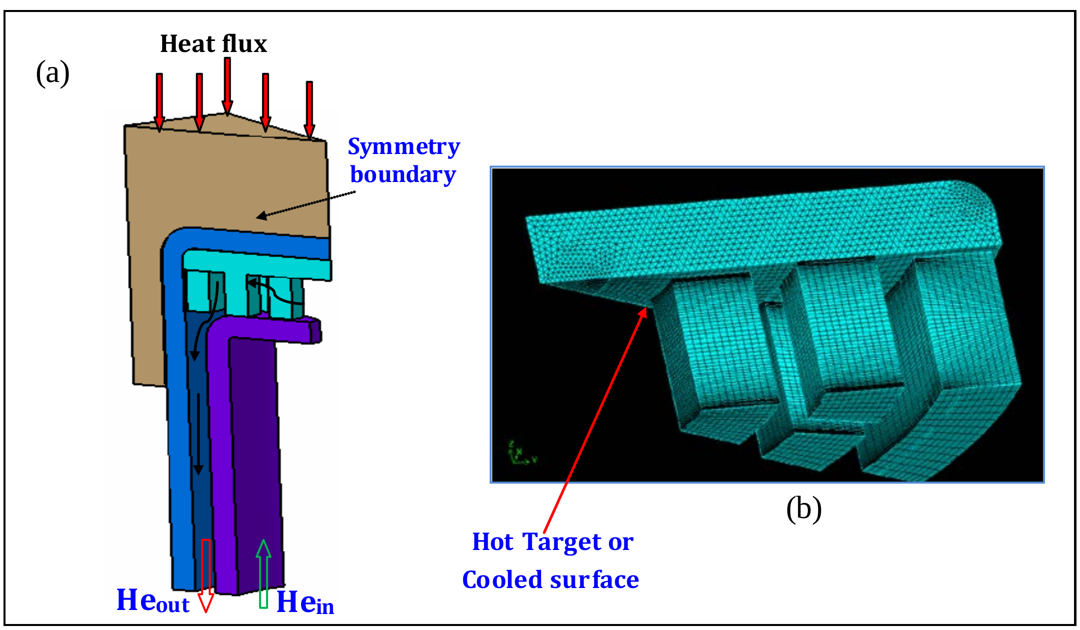

Fig. 3.2. (a) Finger mock-up with boundary condition and (b) grid domain of SES.

3.2. BENCHMARK VALIDATION

Benchmarking the numerical calculation against suitable experimental data is of vital importance in CFD studies. For the validation exercise, same geometric structure as reported in the literature [48] has been adopted. In the reported literature, helium-cooled concept based on multi jet impingement has been adopted. The coolant has an inlet temperature and pressure of about 873 K and 10 MPa. The thermal hydraulic performance of concept was analyzed at constant mass flow rate 13.5g/s and heat flux is varied in the range of 4.01 -12.6 MW/m^2.

3.2.1. Grid Sensitivity Analysis

In a CFD simulation, establishing grid size towards independent nature of the solution is an essential first step. In this regard, efforts are made to determine the optimum mesh for the present numerical simulations. Different mesh sizes employed for the grid sensitivity study are shown in Table 3.1 along with maximum tile and thimble temperature. Temperature differences increase, because the grid spacing reduces with increase in the number of control volume. The reduction in the grid spacing reduces the discretization error in the solution and predicts the most accurate results as compare to coarse mesh.

Table 3.1: Grid sensitivity analysis

Mesh	Control Volume	Minimum grid spacing (mm)	Maximum tile Temperature (°C)	Maximum thimble Temperature. (°C)	CPU time per Iterations (s)
M1	2.5×10^5	0.2	1687	1087	3
M2	3.5×10^5	0.15	1675	1064	5
M3	**5×10^5**	**0.1**	**1651**	**1004**	**8**
M4	6×10^5	0.08	1649	1003	12
Maximum 'tile' and 'thimble' temperature as reported in literature [48] are 1660.3°C and 1010.73°C respectively.					

It can be noticed that the difference between temperature distributions of tiles and thimbles obtained from mesh M3 and M4 are small. The percentage of deviation in temperature between M3 and M4 are 0.12% and 0.09% respectively. Though the change is a small but computational effort is significantly higher for M4 as compared to M3, thus justifying the use of mesh M3 for further investigations.

3.2.2. Parametric Studies

Systematic parametric studies are performed using mesh M3 for various mass flow rates with different heat flux. This particular grid has been chosen after performing a detailed grid sensitivity study as discussed in Section 3.2.1. The outcomes of these parametric studies are depicted in Figs. 3.3(a) and (b). It is observed that temperature at tile & thimble and rise in temperature of helium gas continuously increase with increase in the heat flux whereas the pressure drop remains unchanged, as expected.

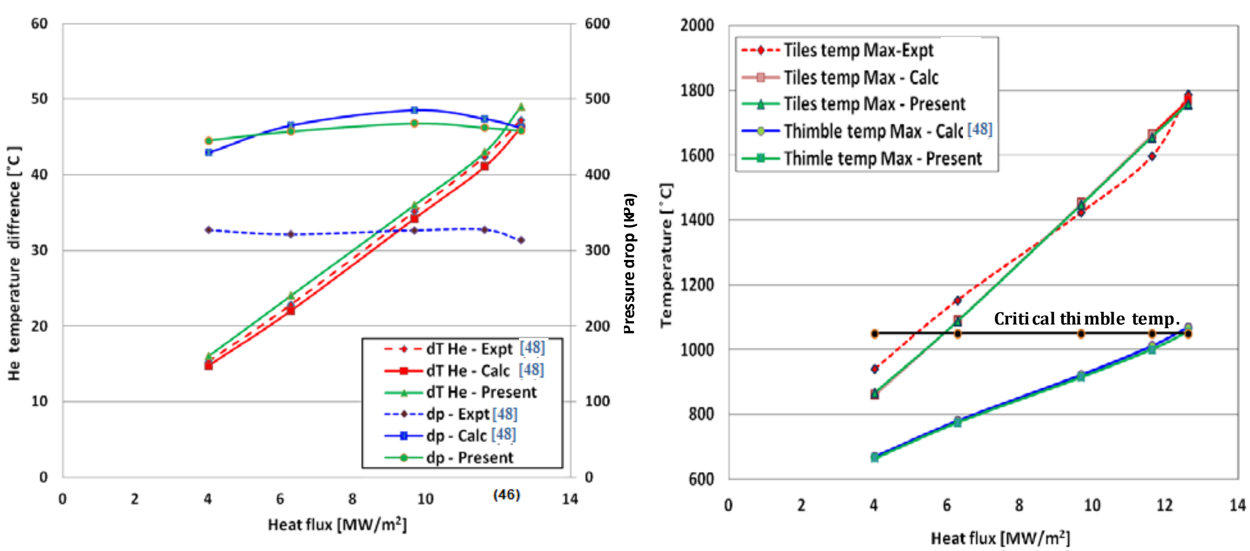

(a) (b)

Fig. 3.3. Comparison between (a) helium pressure drop & temperature difference and (b) maximum tile and thimble temperature as a function of heat flux.

In the present simulations, temperature distributions across tile, thimble and rise in temperature of helium gas at various heat fluxes are found to be in good agreement with the reported results [48]. Analysis has been performed for nominal mass flow rate and is validated against the reported result. The temperature distributions in the solid and fluid regions are presented in Fig. 3.4. The maximum tile temperature occurs at the outer corner of the surface, and the maximum thimble temperature is noticed just above the central jet.

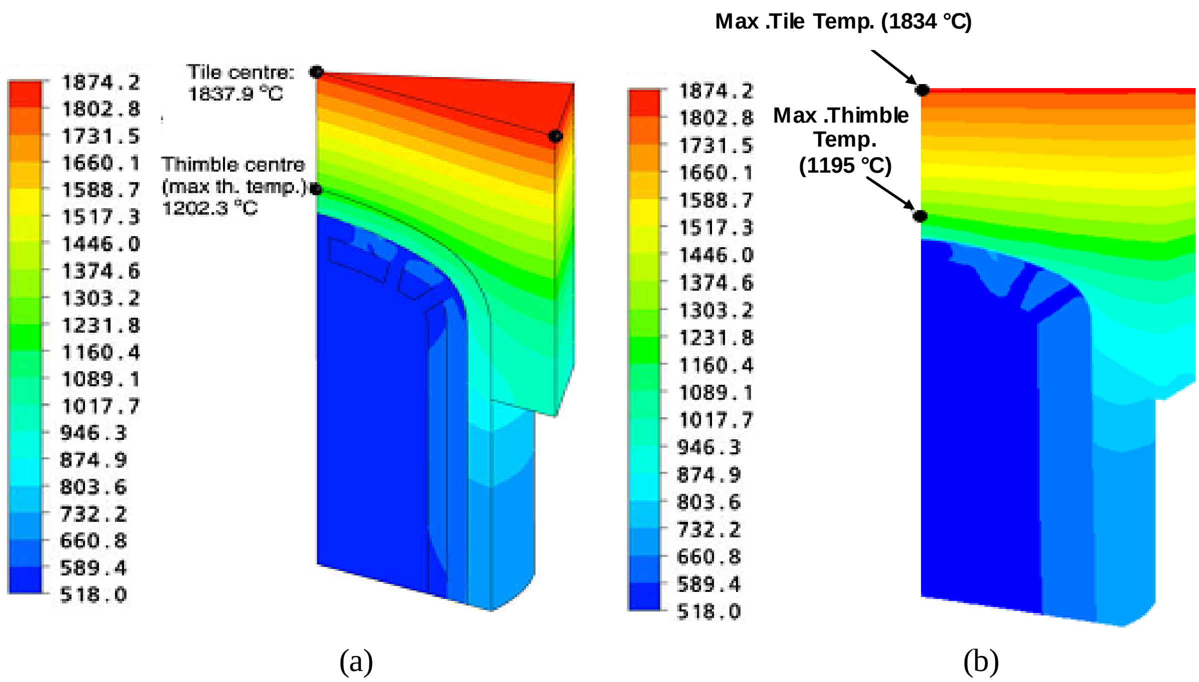

Fig. 3.4. Temperature distribution for mass flow rate of 6.8 g/s with a heat flux of 10 MW/m^2 (a) reported results and (b) present simulation.

3.3. RESULTS AND DISCUSSION

3.3.1. Comparative Studies for Flow & Heat Transfer Analysis

Comparative studies for flow & heat transfer without SES and with SES have been carried out and presented for mass flow rate of 5 g/s with heat flux value of 10 MW/m^2. Figure 3.5(a) depicts distribution of turbulence kinetic energy with the presence of SES. It is seen that maximum kinetic energy occurs at the nozzle entrance due to high velocity of coolant at the centre. The sectional top view of velocity distribution around SES is depicted in Fig. 3.5(c). Symmetric eddies are formed in between the extended surfaces due to flow obstruction, which is similar to flow across bluff bodies. Flow bypass occurs through the gap between the wall of the extended surfaces and the channel wall that is clearly seen from the figure. Formations of eddies leads to increase in turbulence activity and hence increase in the rate of heat transfer.

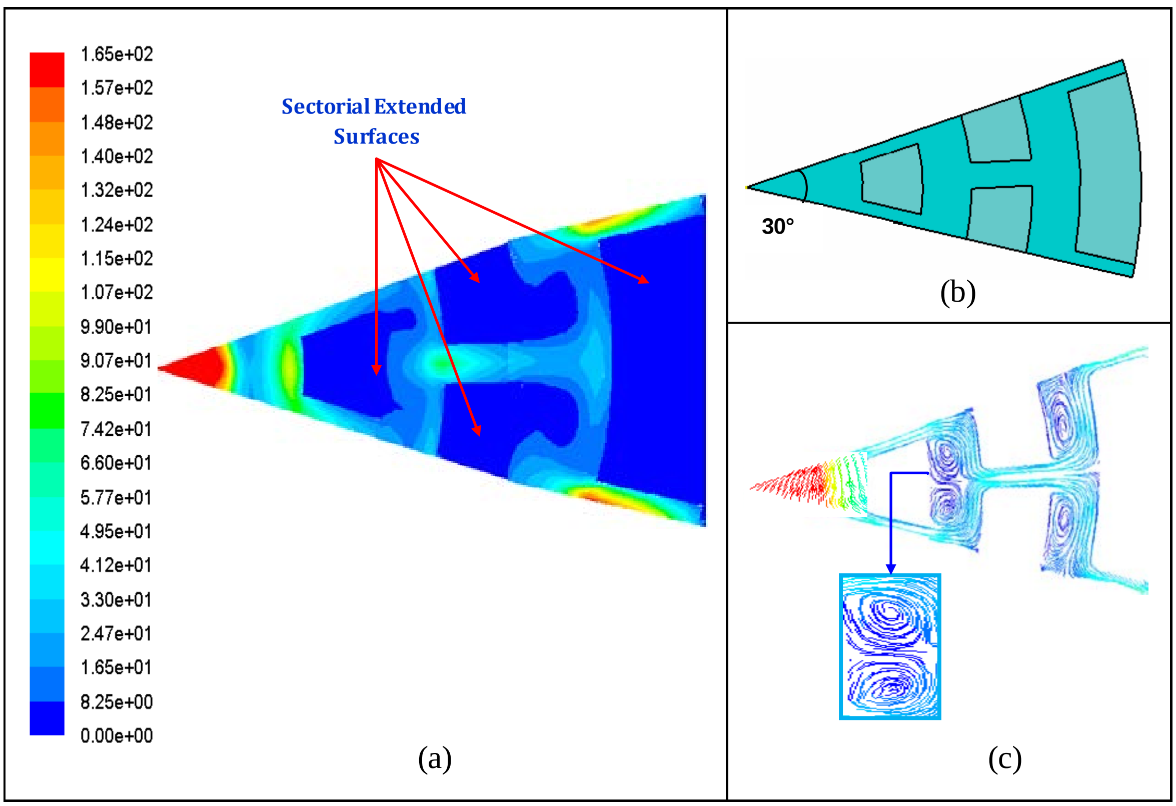

Fig. 3.5. (a) Sectional top view of turbulence kinetic energy distribution (m^2/s^2) around SES (b) sectional view of 30˚ sector of SES (c) velocity distribution (m/s) with close up view.

Temperature distributions for without and with SES are shown in Fig. 3.6. It is observed that the temperature of tile and thimble are reduced for SES as compared to that without SES. The addition of extended surface in divertor finger mock-up increases heat flux distribution and heat transfer rate as compared to smooth channel as more surface area is available for fluid to interact with the hot surface.

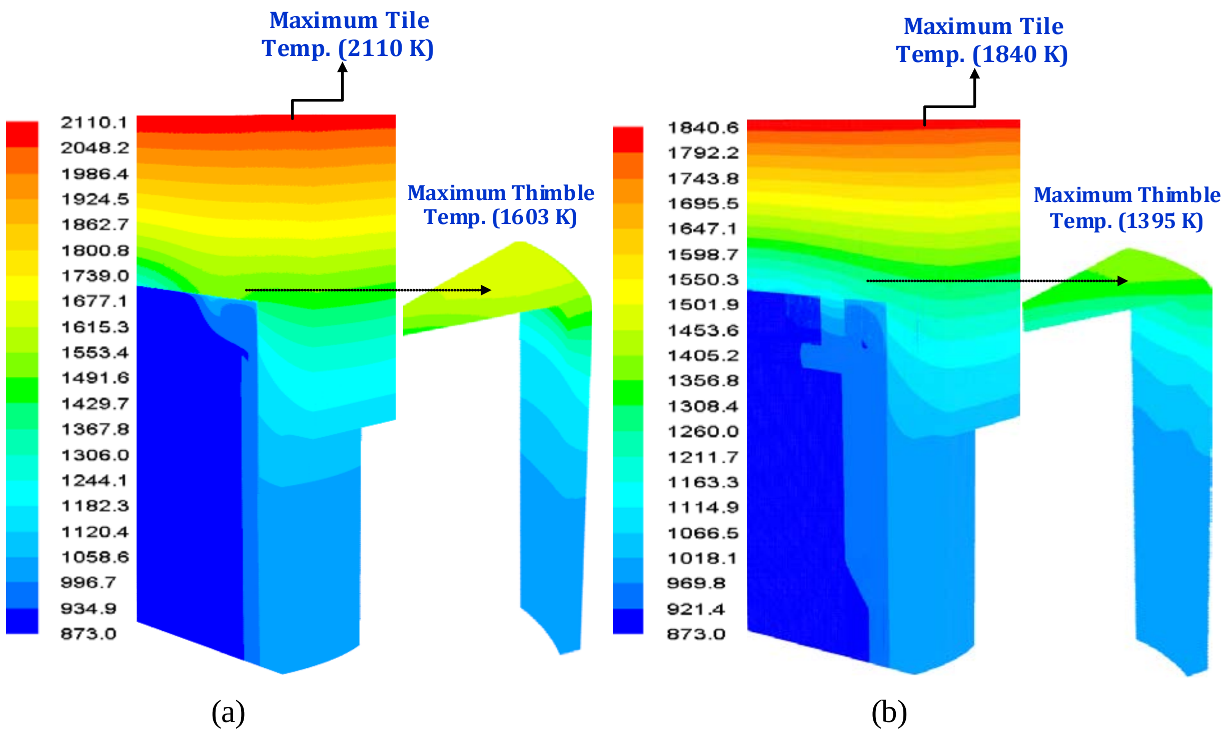

Fig. 3.6. Temperature distribution of divertor cooling finger mock-up design (a) without SES and (b) with SES.

3.3.2. Extraction of Thermal parameters

The effective heat transfer coefficient (h_{eff}) for the case without SES is determined based on the average heat flux (Q/A_c) incident on the cooled surface and the temperature difference between the cooled surface wall and the bulk fluid as defined by,

- $h_{eff} = Q / (\overline{T_c} - T_b) A_c$ (3.1)

The test section without extended surface actual and effective heat transfer coefficient (h_{act} = h_{eff}) will be same due to unavailability of extended surface. However, the effective wall heat transfer coefficient for the test section with extended surface requires accounting the fin efficiency (η), because the surface temperature of the SES is spatially non-uniform. Therefore,

- $h_{eff}\ A_c = h_{act}\ (A_p + A_e\ \eta)$ (3.2)

Efficiency (η) of the extended surface is given by [79]:

- $\eta = (\tanh Ml)/Ml$ (3. 3)

where, $M = \sqrt{\frac{h_{act}\ P_e}{\lambda_e\ A_{ce}}}$ and 'l ' is the length of SES.

Effectiveness (ζ) of the extended surface is defined as the ratio of heat transfer rate by SES to that without extended surface and is written as:

- $\zeta = A_e \times \eta\ / A_c$ (3. 4)

The corresponding pumping power (W) is then determined by:

- $W = m \times \Delta P\ /\ \rho$ (3. 5)

Where the symbols have their usual meanings and are described in the nomenclature.

3.3.3. Assessment of Performance for Flow Parameters (without SES)

The prime motive of this investigation is to find optimum mass flow rate at an acceptable pressure drop for cooling of finger mock-up. Towards this, numerical studies have been performed without considering SES at different heat fluxes value, viz., 8, 10, and 12 MW/m^2 over a wide range of mass flow rates (5 – 20 g/s). Temperature distributions on the surface of tile and thimble for various mass flow rates for given heat loads are depicted in Fig. 3.7(a) and (b) respectively.

Figure 3.7 shows that the tile and thimble temperatures are within design limits for lower heat flux value of 8 MW/m^2 with mass flow rate of ~ 10 g/s, whereas for higher heat flux (10 - 12 MW/m^2), flow rate in the range of 14 – 19 g/s is required to keep thimble temperature within the design limits (1050 ˚C). From the above figure, it implies that without SES, cooling finger will require very high mass flow rate and hence pumping power will be high to maintain the desired constraint.

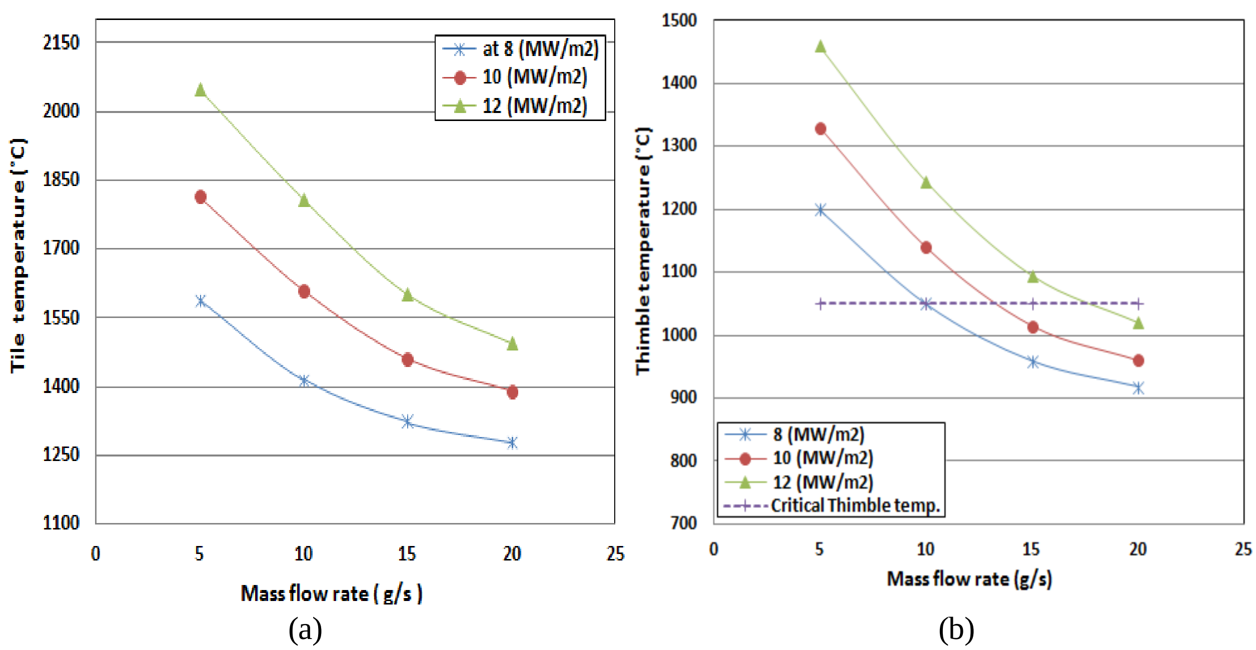

Fig. 3.7. Maximum temperature as function of mass flow rate at different heat loads (a) tile and (b) thimble.

Figures 3.8(a) and (b) represent heat transfer coefficient and pressure drop as a function of Reynolds number (Re). With increasing Re, both h_{eff} and ΔP increases however, there is no appreciable effect observed with variation in heat flux due to the temperature variation of cooled wall surface.

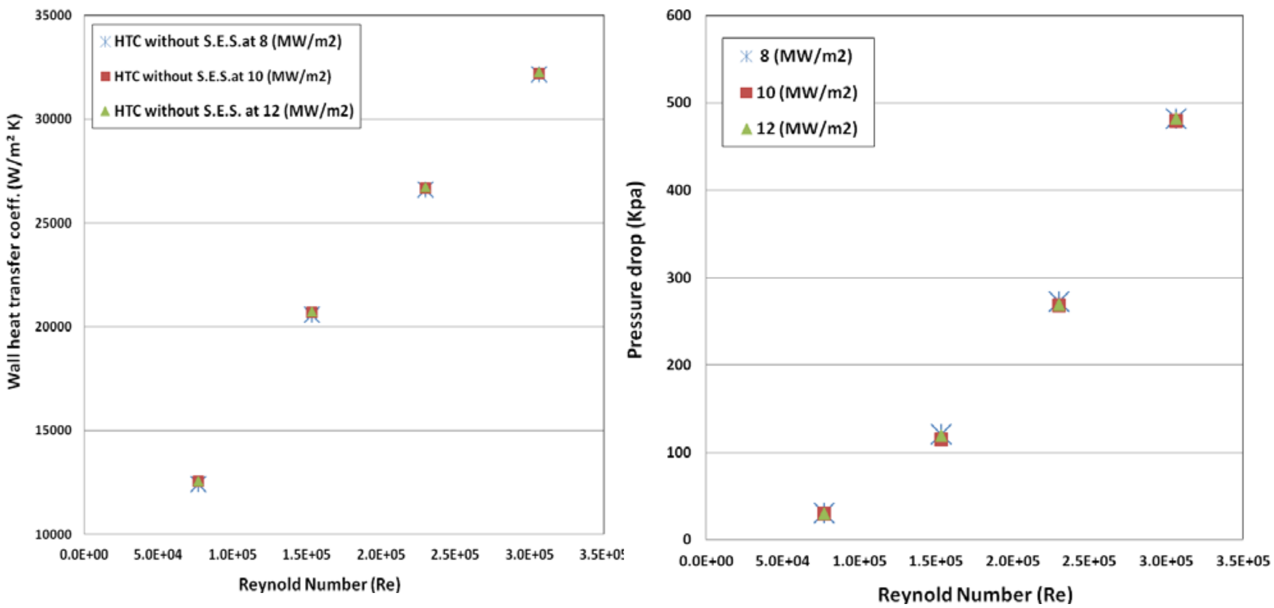

(a) (b)

Fig. 3.8. Effect of Reynolds number on (a) heat transfer coefficient and (b) pressure drop at different heat loads.

3.3.4. Performance Analysis with Extended Surfaces

Thermal-hydraulics performance of finger mock-up has been analyzed to find the effectiveness of SES at specified heat load conditions described in Section. 3.3.3. Four cases (Flow with & without SES) are analysed with two-heat flux, viz., 8 and 10 MW/m^2. Coolant mass flow rate is varied from 5 – 20 g/s. Maximum temperature values on tiles and thimble without, and with SES at different mass flow rates are depicted in Fig. 3.9.

It is observed that, tiles and thimble temperature reduces with an increase in flows rate. The temperature values along the tiles and thimble with SES are significantly lower than that without SES. With the presence of SES, lesser mass flow rates (5 g/s for heat flux of 8 MW/m^2 and 7.3 g/s for 10 MW/m^2) are adequate to keep thimble temperature within the desire limits.

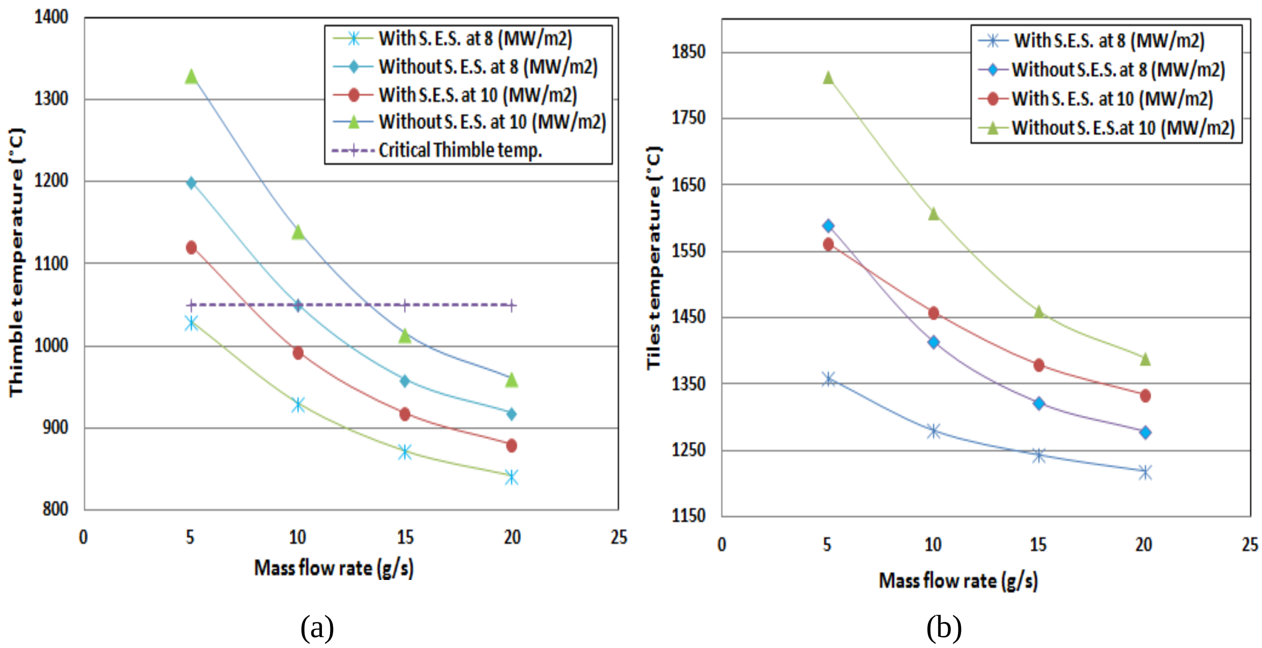

Fig. 3.9. (a) Comparisons of tiles and (b) thimble maximum temperature for with and without SES at different heat loads.

Figure 3.10 represents the variation of effective heat transfer coefficient (h_{eff}) and pressure drop for without and with SES at different Re. It is noted that 'h_{eff}' for both the cases increase with the rise in Re, but the rate of increase is higher in presence of SES. This is due to increase in the surface area that enhances turbulence in the flow of gas and hence improves the effective heat transfer coefficient. Similarly, the values of pressure drop increases in the presence of SES as compared to that without extended surfaces as seen from Fig. 3.10(b) as expected.

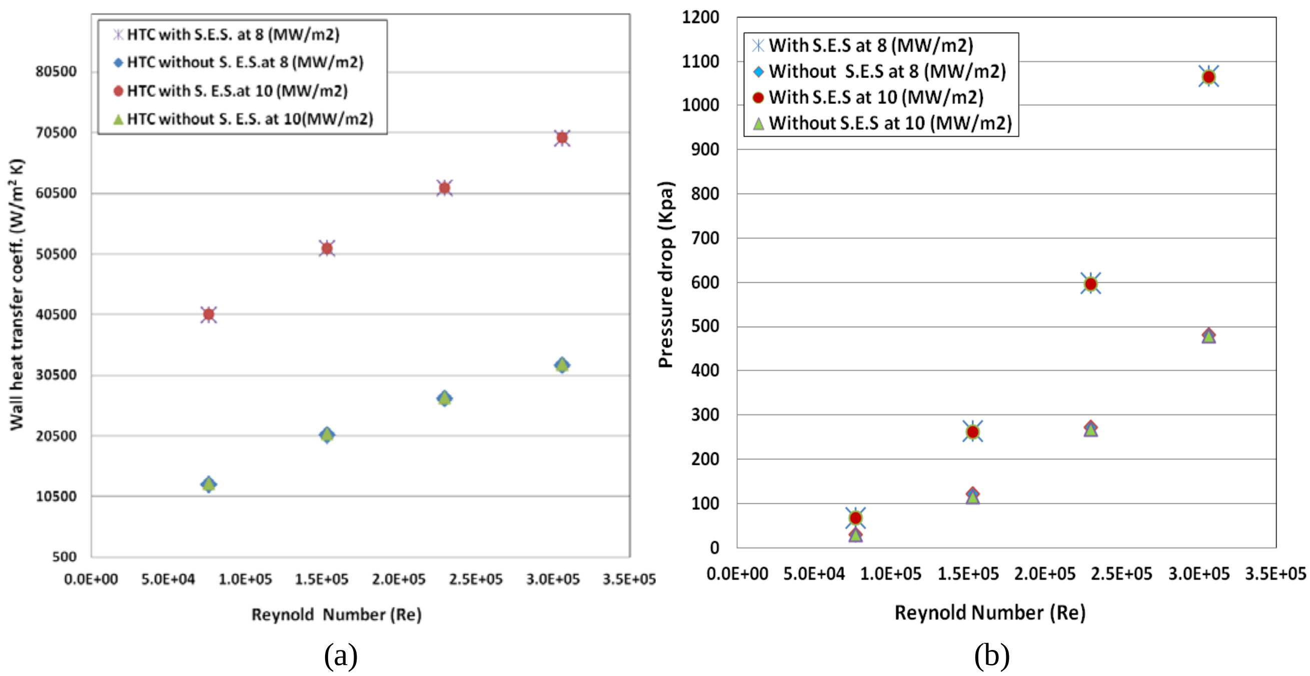

Fig. 3.10. Comparisons of (a) effective wall heat transfer coefficient and (b) pressure drop for with and without SES at optimized heat loads.

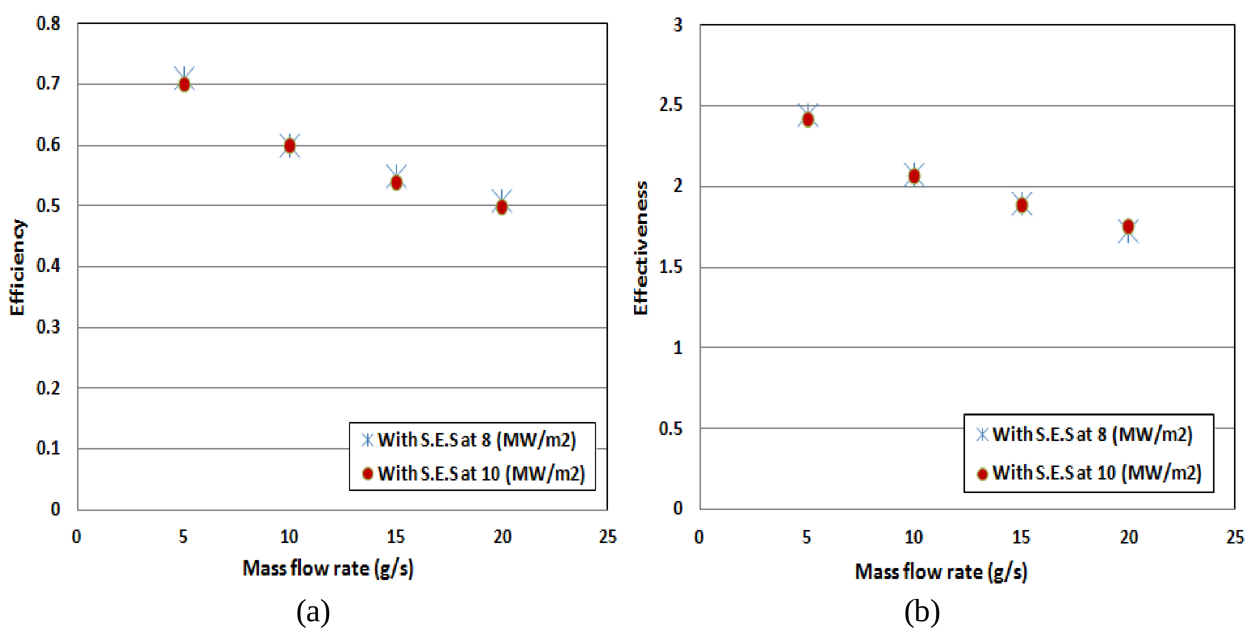

Fig. 3.11. (a) Comparison of efficiency (η) and (b) effectiveness (ζ) with SES.

Variation in efficiency (η) and effectiveness (ζ) with mass flows rate are depicted in Fig. 3.11. It is seen that both η and ζ are maximum at lower mass flow rate, and they start decreasing continuously as mass flow further increases. This particular behaviour is expected as both these factors inherently depend on heat transfer coefficient. From the above comparison, it is implied that extended surfaces potentially enhance the thermal performance of the finger mock-up.

3.3.5. Design Analysis of Divertor Finger Mock-up

The dependence of pumping power on the proposed design of finger mock-up has been investigated for various mass flow rates and is presented in Fig. 3.12. It is seen that, the pumping power continuously increases with mass flow rate for a constant heat flux 10 MW/m^2. Dashed line marks the design limit on pumping power.

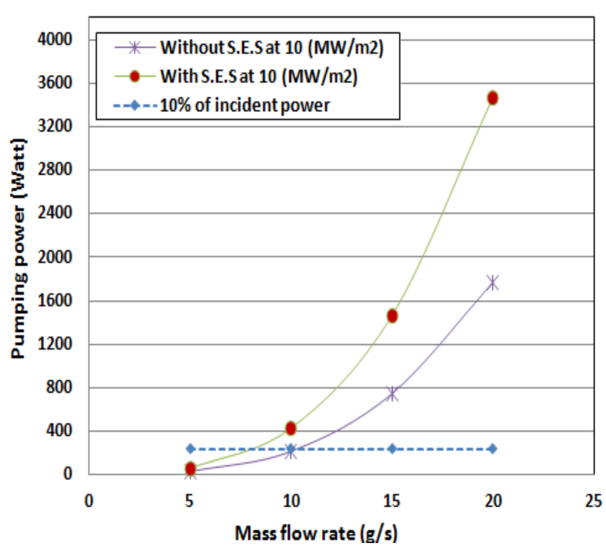

Fig. 3.12. Comparison of pumping power with and without SES as function of mass flow rate.

From the figure, clearly the mass flow rate should not exceed 10 g/s for the finger mock up without SES, so as to limit pumping power within 10% limit. However, this limitation on flow rate leads to exceeding the temperature limits (Fig. 3.7b, Sec 3.3.3). Therefore, the reference design is unable to tolerate 10 MW/m^2 unless extended surface is added to it. It is also seen that, with the addition of SES, even a lower mass flow rate of ~7.3 g/s is adequate to maintain the desired temperature and pumping power constraint.

The maximum heat flux to be accommodated by finger mock-up at allowable tile/thimble filler temperature constraint has been estimated as:

$$q'' = \frac{\left(\overline{T}_c - T_i\right)}{\left(\dfrac{A}{h_{eff} A_c} + \dfrac{t}{\lambda_t}\right)} \tag{3.6}$$

where t and λ_t denote the thickness and thermal conductivity of the thimble respectively.

Figure 3.13 depicts the variation of heat flux with mass flow rate for the cases with and without SES at 10 MW/m^2. It is observed that prototypical mass flow rates for fusion power plant (~7.3 g/s) with SES can accommodate a heat flux of 10 MW/m^2 whereas it is only ~4.5 MW/m^2 without SES. In order to accommodate high heat flux exceeding 10 MW/m^2 with the present design, melting limits of the tile/thimble brazing filler material should be increased.

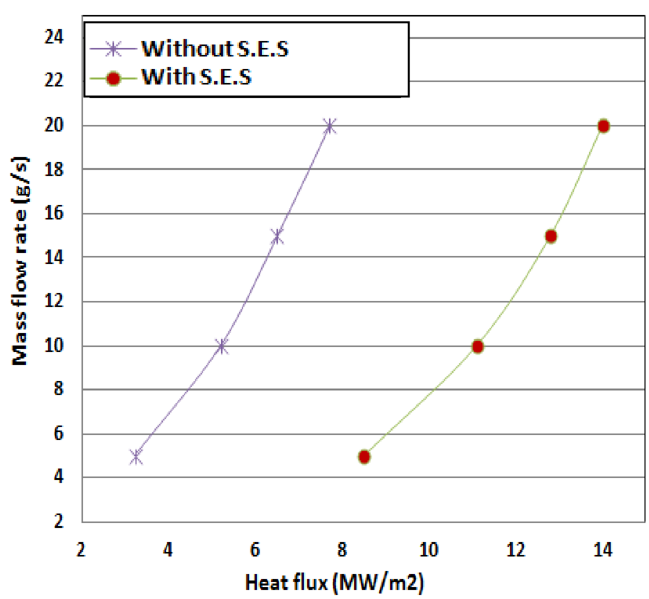

Fig. 3.13. Comparison of mass flow rate without and with SES for different heat flux values.

Parametric studies on pumping power without and with SES are analyzed for two different pumping power limits, viz., 10 – 15 % of the total power removed from the tile and thimble. The corresponding results are depicted in Fig. 3.14. It is observed that with extended surface, finger mock-up can tolerate up to a maximum heat load of 10 - 11.2 MW/m^2 at the expense of pumping powers 10% and 15 % of the incident power. However, without the extended surfaces, it can handle highest heat load of 5 MW/m^2 only.

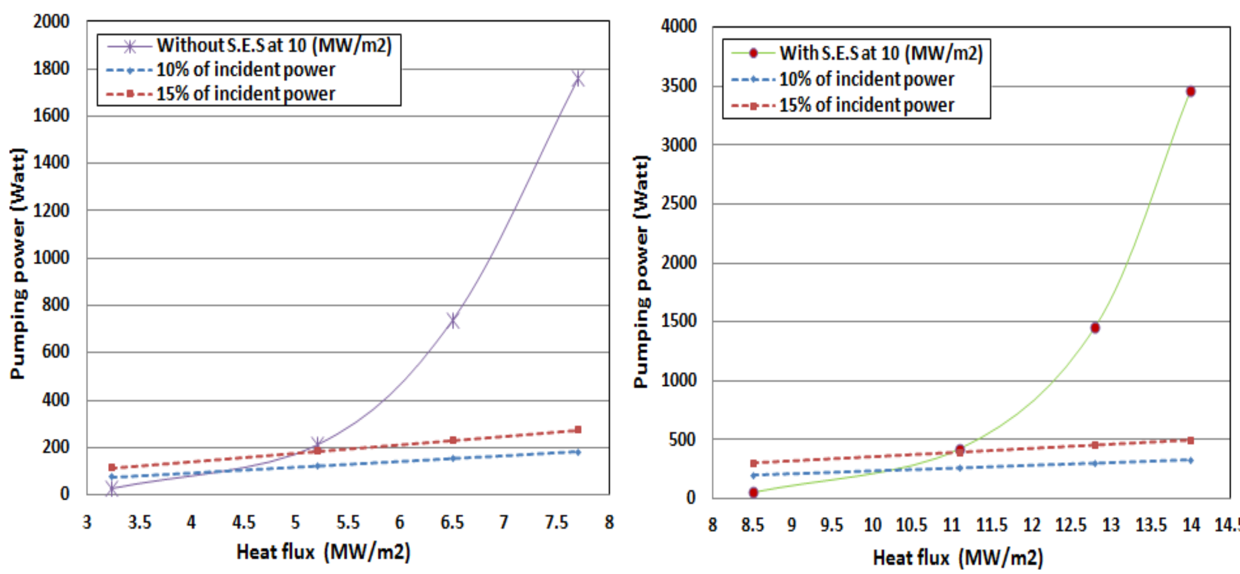

(a) (b)

Fig. 3.14. Comparison of pumping power (a) without SES and (b) with SES as a function of heat flux.

Figure 3.15 compare the effective heat transfer coefficient obtained for heat flux 10MW/m^2 with pumping power for with SES and without SES. From the figure, it is found that at identical required pumping power, the mock-up with extended surface offer a higher heat transfer coefficient and thereby higher heat transfer enhancement. From all these parametric studies, it is evident that the use of extended surface in the finger mock up significantly increase the thermal performance associated with low additional pressure drop. To respect pumping power and thimble temperature limit, low mass flow rates (~ 7.3 g/s) is adequate for the present design.

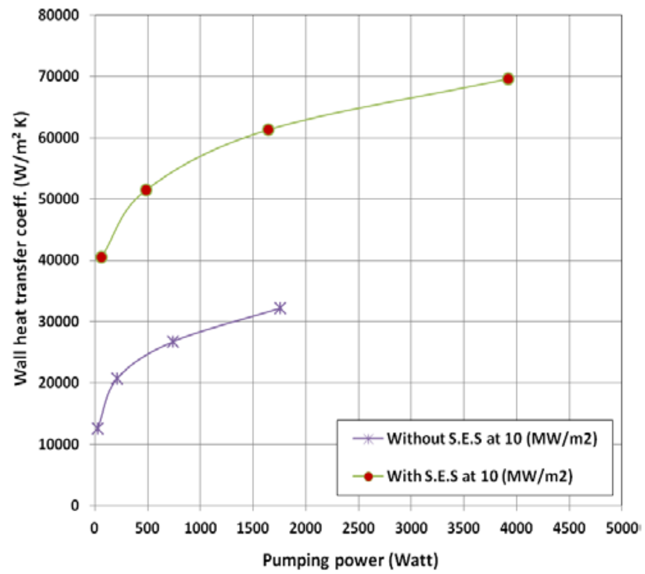

Fig. 3.15. Comparison of effective wall heat transfer coefficient for without SES and with SES as function of pumping power.

3.4. THERMO-MECHANICAL ANALYSIS

In order to verify the practicability of design, thermo-mechanical investigations are carried out using finite element analysis tools [70]. Towards this, nodal temperatures and pressure obtained from the CFD optimization studies are imported to the FEM software for structural analysis. For the entire solid domain, temperature dependent material properties [78] are considered, and frictionless boundary condition is considered at the bottom.

Figure 3.16 shows temperature distribution around the extended surface as well as the von-Mises stress for the optimized geometry. Figure 3.16(a) illustrates the maximum temperature at top of the mock up and the temperature distribution around the extended surface is nonhomogeneous. It is seen that the maximum stress develops at the tile-thimble interface. However, all the stresses are within the permissible limit [3.16b].

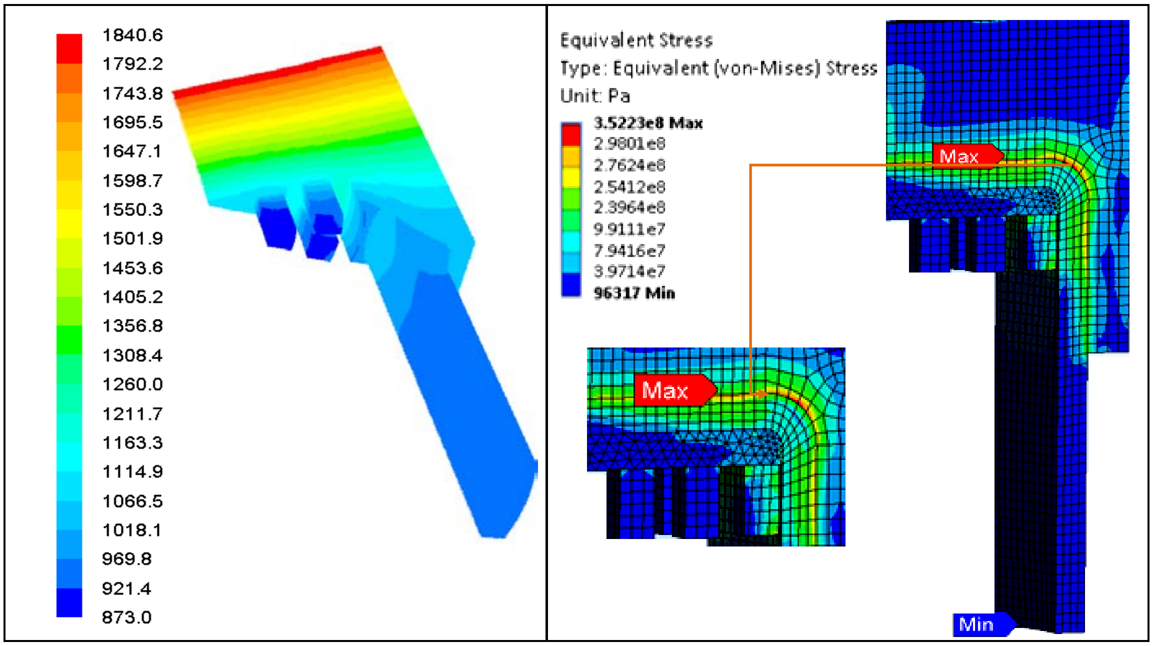

Fig. 3.16. 30˚ sector cooling finger mock-up (a) Temperature distribution (K) (b) von-Mises Stress distribution.

3.5. CLOSURE

The fluid flow and heat transfer characteristics of divertor cooling finger mock-up are investigated through jet impinging technique with and without sectorial extended surfaces (SES). The main objective of the present study is to numerically evaluate how addition of SES affects the thermal hydraulics performance of finger type divertor. Towards this, systematic studies by modelling of one such cooling finger have been carried out. Grid sensitivity analyses have been performed through a 30˚ sector model, and the optimized grid has been obtained. In the second stage, flow and heat transfer features have been investigated and are compared with the published experimental and computational data. The calculated and measured values of the tile and thimble surface temperatures show good agreement with the reported results. Numerical investigations showed that addition of SES greatly increases thermal-hydraulic performance of the finger mock-up. Performance analysis indicates that present mock-up design should be acceptable for mass flow rate less than 7.3 g/s (Re ~111000) to ensure desired pumping power and thimble temperature limits. Adding the array of extended surface doubles the maximum heat flux that can be accommodated by the divertor finger mock-up. Thermo-mechanical analysis has been carried out for the finger mock-up through finite element based approach. It is seen that, all the stresses are within the permissible limit.

CHAPTER 4

EXPERIMENTAL STUDIES WITH DIVERTOR FINGER MOCK-UP AND VALIDATION OF THE CFD MODEL

4.0. INTRODUCTION

A jet impingement technique with a sectorial extended surface (SES) concept for the modular helium-cooled divertor has been numerically studied in the earlier Chapter 3. The computational study indicated that heat removal potential greatly enhances with the addition of SES in divertor finger mock-up. However, no experimental data have been reported to validate the findings. Hence, it is required *to conduct an experimental investigation to validate the thermal hydraulic performance of a finger mock-up design with proposed SES*.

Critical thermal hydraulic parameters, effective heat transfer coefficient and pressure loss have been measured in the experiment for the reference divertor as well as for a divertor with SES. The thermal performance has been evaluated by comparing the heat transfer coefficient and pressure drop across the test section. The experimental mock-ups are made to full scale respecting Reynolds and Prandtl number similarities. Air is used as the simulant to represent helium, which is the coolant in prototype. Heat concentrator has been developed to simulate the high heat flux, by electrical heating. The benchmark experimental data have been used to validate the three dimensional conjugate heat transfer models.

The computational result for heat transfer coefficients and pressure loss are in satisfactory agreement with the experimental results. Based on detailed parametric studies, correlations have been proposed for Nusselt number (Nu) and pressure loss coefficient (K_L) as a function of Reynolds number which can be used for design applications. The proposed SES divertor is seen to significantly improve the thermal performance of the finger type divertor at the penalty of a minimum pressure drop at the prototypical condition. The results of the present study provide added confidence in the numerical model used to design the divertor and its applicability to other gas cooled components.

4.1. EXPERIMENTAL STUDIES

4.1.1. Experimental Condition

It is known that geometric and dynamic similarities are very essential to carry out model experiments, and enable one to scale up the results from model to prototype. In the present investigation test geometries were manufactured to closely resemble the prototype for testing in an air loop. The test condition studied has Reynolds (Re) and Prandtl (Pr) numbers similar to the prototypical operating condition of the divertor as presented in Table 4.1. The Reynolds number based on the jet diameter (2 mm) is defined as:

$$Re = m\, D / (\mu\, A_{jet}) \tag{4.1}$$

From Table 4.1, it is observed that the effect of Pr number on thermal performance of divertor is less affected due to negligible difference in Pr numbers for air and helium. The "prototypical Reynolds number" (Re_p) corresponding to mass flow rate ~7.3 g/s of the jet is 1.1×10^5 and for the present investigation, it is varied over a wide range 6.9×10^4 to 2.6×10^5 with an incident flux of ~ 0.75 MW/m^2.

Table 4.1: Comparison of thermal hydraulic parameters for the actual He-cooled divertor and experiment studies using air loop.

Coolant	Inlet Temperature	Inlet pressure	Dynamic viscosity	Heat flux	Gas Flow Rate	Re_p	Pr_p
	(˚C)	(bar)	(kg/m-s)	(MW/m^2)	(g/s)		
He	600	100	4.16×10^{-5}	10	7.3	1.1×10^5	0.70
Air	~27	6.86	1.80×10^{-5}	~0.75	3.1	1.1×10^5	0.68

4.1.2. Experimental Test Module

Thermal conductivity of brass is similar to tungsten alloy at high temperature. Hence, experiment has been performed in a brass alloy test module with uniform incident heat flux, as depicted in Fig. 4.1. The test module consists of jet cartridge, outer brass shell assembly and heat concentrator. The experimental investigation has been carried out in test module with two design configurations, with and without arrays of sectorial extended surface.

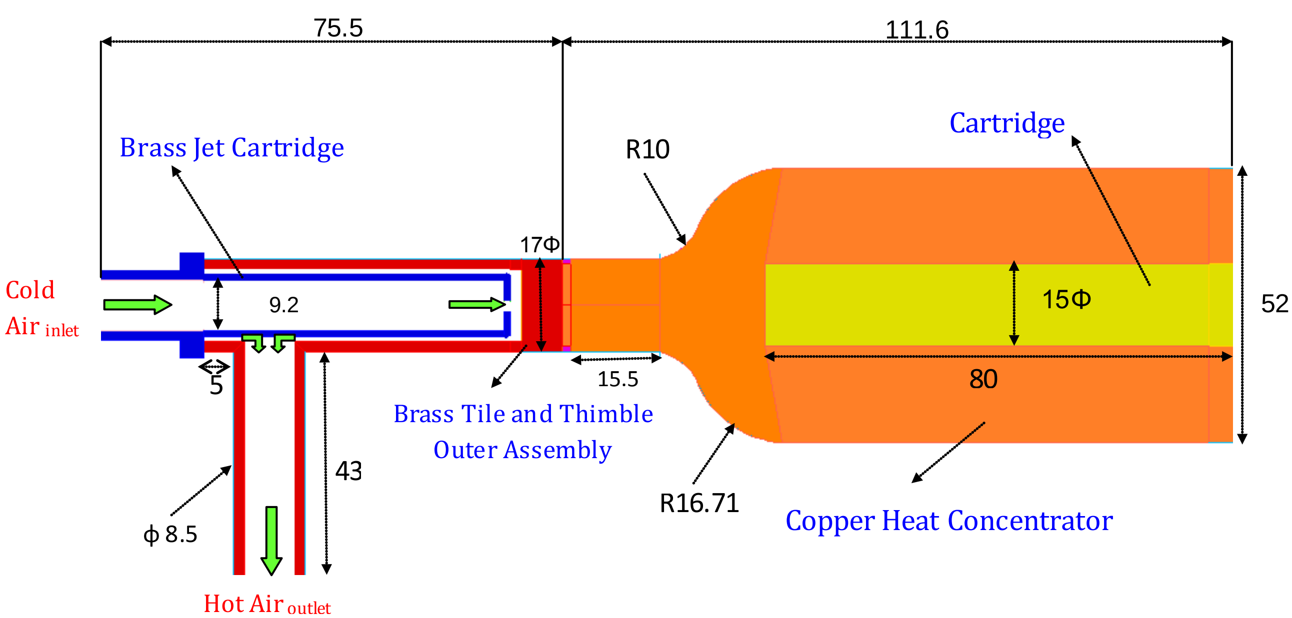

Fig. 4.1. Experimental test module assembly without SES (all dimensions in mm).

4.1.2.1. Heat Concentrator

A copper heater block is used to achieve a uniform incident heat flux, and the block is tapered at the neck region to focus and increase the incident flux at the test module. A high density 950 W cartridge heater (OD15 mm x 80 mm long) is tightly fitted to the copper heater block to heat the test module as shown in Fig. 4.1. A high thermal conductivity paste has been used between the mating surfaces to minimize the thermal resistance. A variac has been connected to an ammeter and voltmeter to control the power output through the cartridge heater for a uniform heat flux on top of the test module. The neck region (OD 13mm) of the concentrator is slip fitted in the test module. The detailed drawing and photograph of the manufactured heat concentrator are shown in Fig. 4.2.

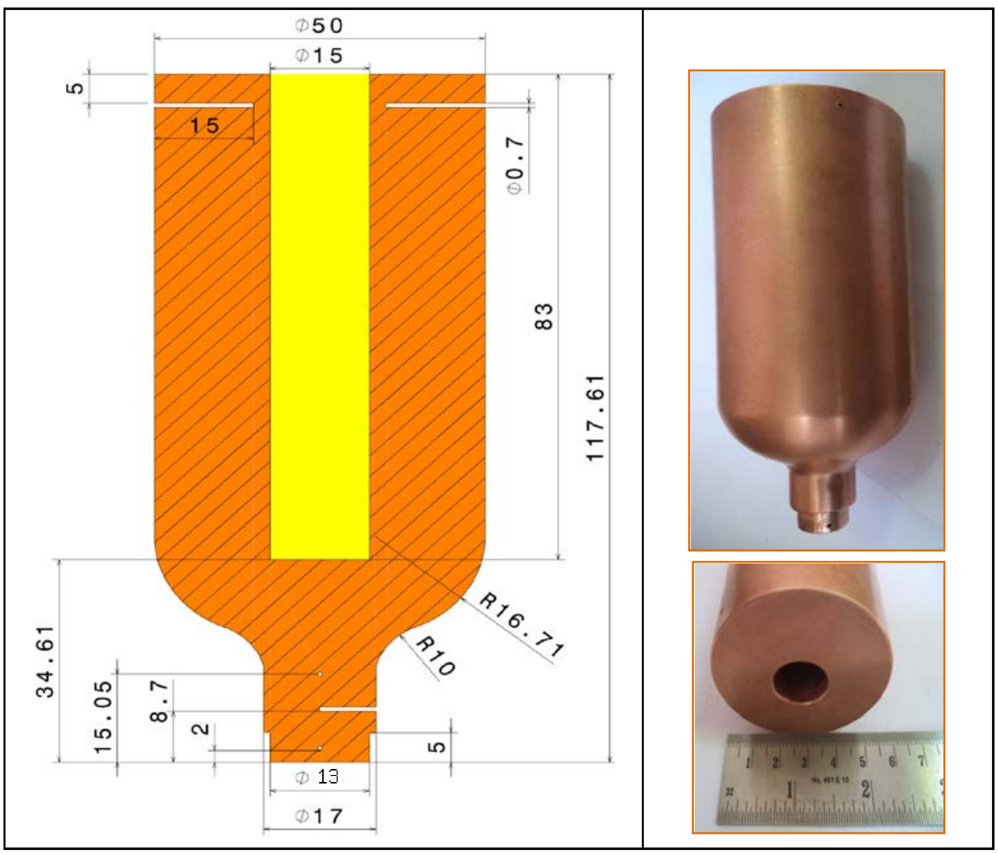

Fig. 4.2. Drawing and photograph of the manufactured heat concentrator.

4.1.2.2. Jet Cartridge and Outer Shell Assembly

The inner cartridge (ID 9.2 mm x 53 mm long) has been constructed in brass that simulates the steel cartridge in the prototype is presented in Fig. 4.3. The gap between the brass cartridge and outer assembly is maintained at 2 mm for the case without SES configuration. The configuration with SES has been manufactured as depicted in Fig. 4.4.

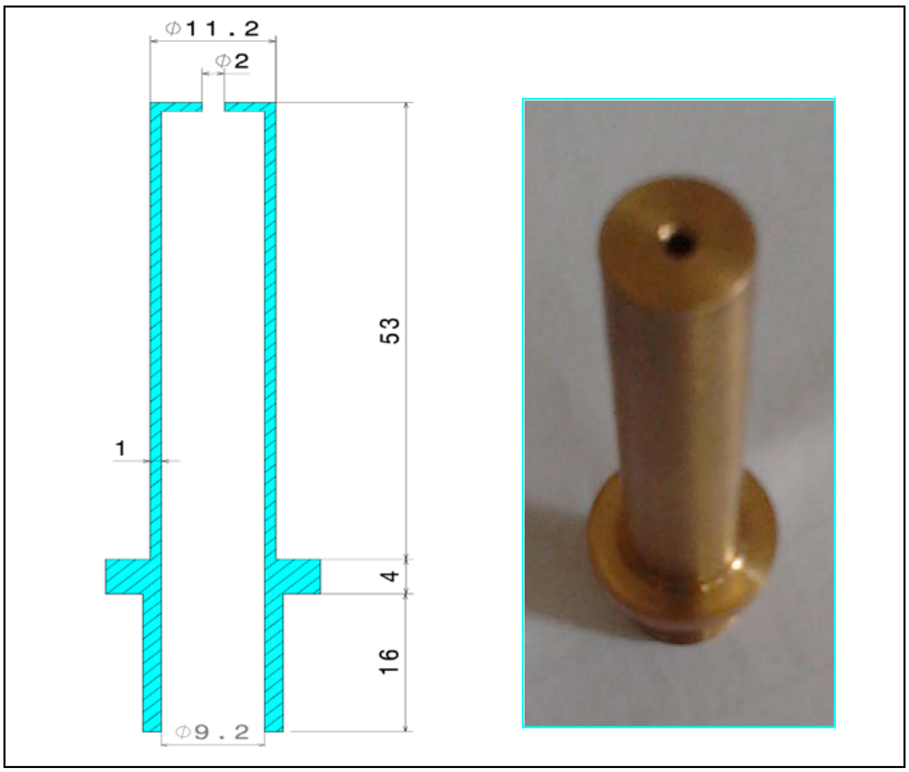

Fig. 4.3. Drawing and photograph of the jet cartridge.

An outer brass shell surrounding the inner cartridge that closely duplicates the W-alloy structure, in the first set of configuration tile, thimble and supporting plate unit has been manufactured as a single entity (Fig. 4.4). The test module is instrumented by way of four 0.6

mm diameter, K–type thermocouples (TCs). All the thermocouples used in the present experimental work, have been subjected to three points (50 °C, 100 °C and 170 °C) calibration within ±1°C accuracy. The thermocouples are insulated with Kapton to have a negligible heat loss. The TCs are positioned within brass alloy, 0.5 mm from the cooled surface and offset by 90˚ to the each other at a radial distance of 2.5, 4.5, 6.5 and 8.5 mm respectively as depicted in Fig.4.4.

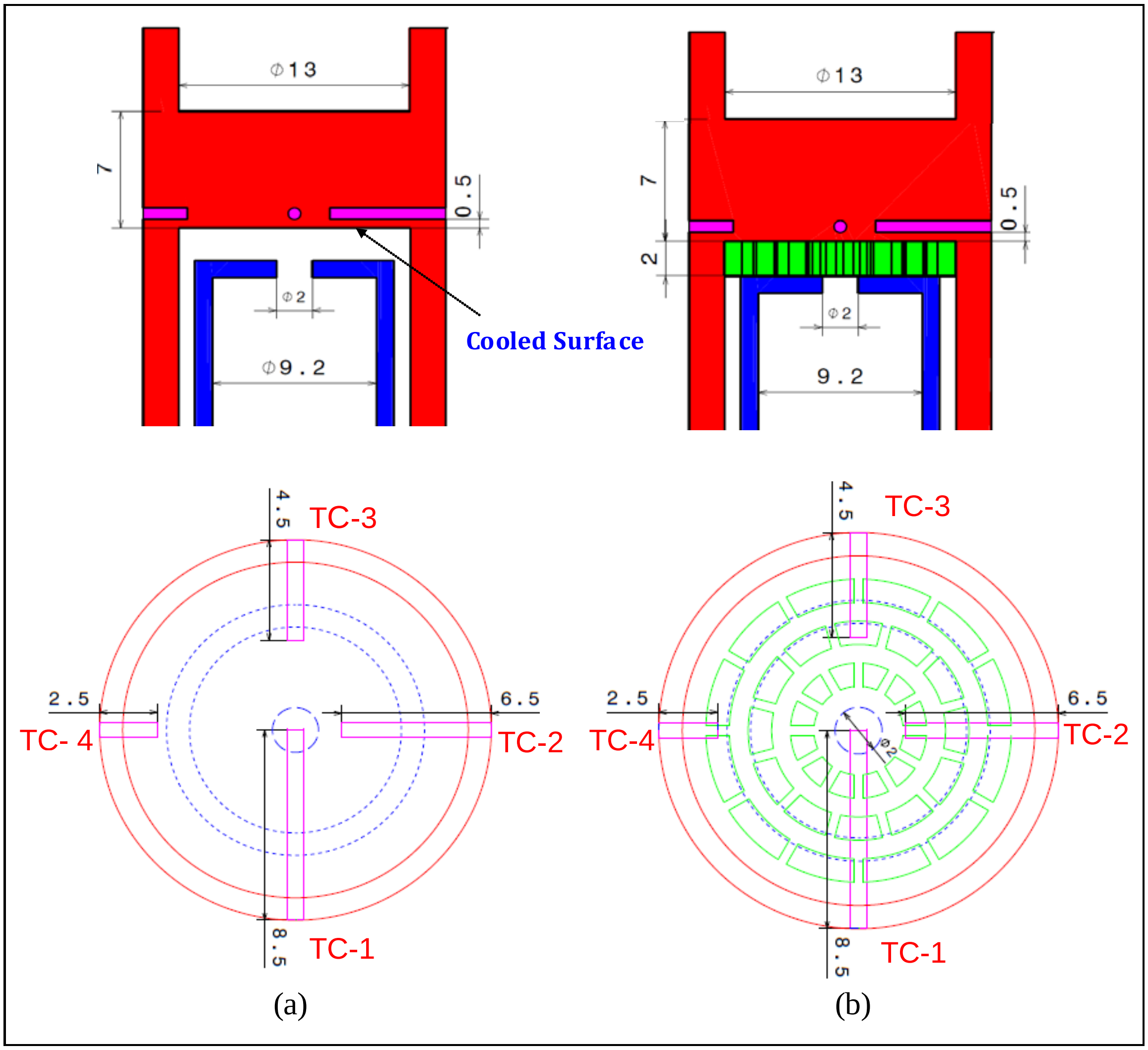

Fig. 4.4. Close up views of experimental test module with thermocouples locations (a) without SES and (b) with SES.

To ensure correct positions of the thermocouples in the test module, thermocouple wires were graduated with a length which was used as a reference for insertion length. A high thermal conductivity paste (OMEGA@600) has been used to fix the thermocouples in the test section and to minimize the thermal contact resistance. The output from these TCs are used to compute the average heat transfer coefficient over the cooled surface for a given incident heat flux. Photographs of the test assembly with different configurations are shown in Fig. 4.5.

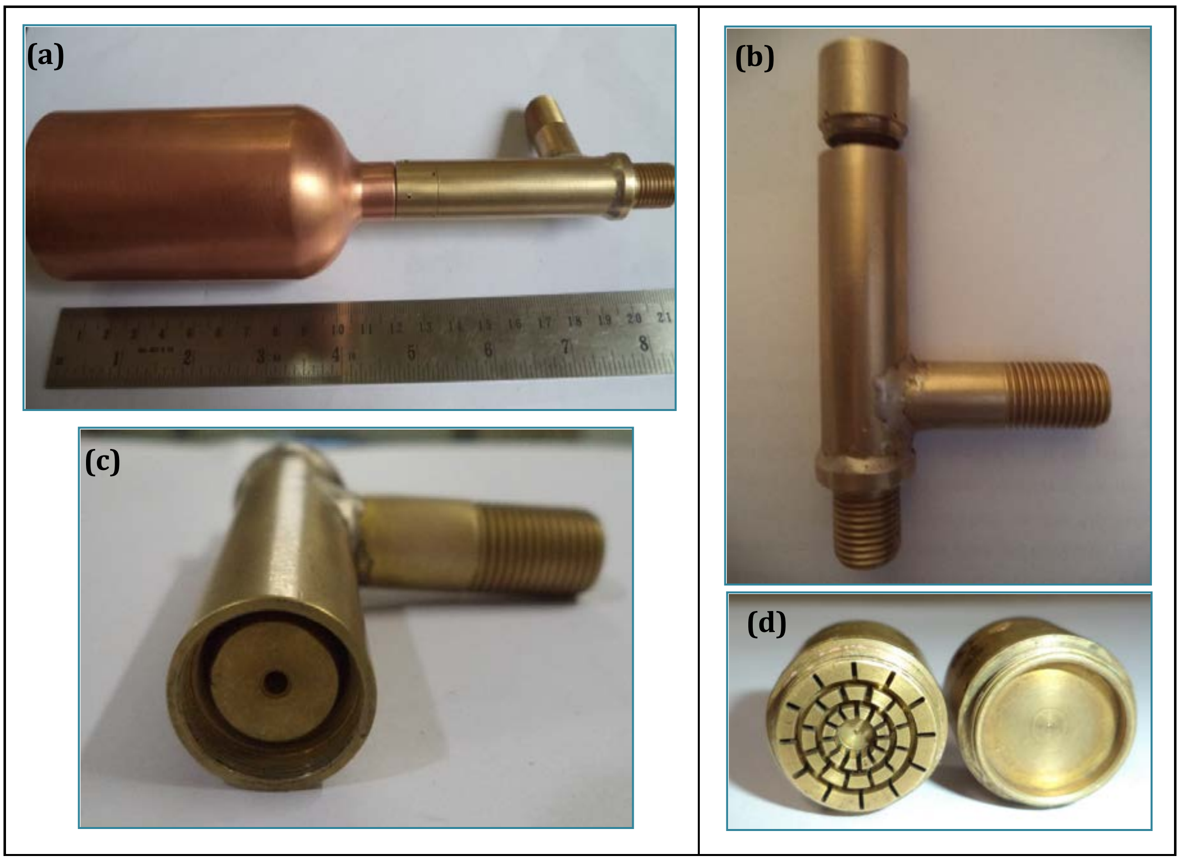

Fig. 4.5. Photographs of (a) assembly of the test section, (b) jet cartridge and outer Shell assembly, (c) section view of test section and (d) with and without SES configuration.

4.1.3. Experimental Flow Loop and Procedure

The experimental test module was investigated in an open air flow loop as shown in Fig. 4.6. Cartridge heater (Kerone, 120 V and 950 Watts) was placed in the copper heater block to heat the test module and a variable transformer was connected to control the power output through the cartridge heater for the uniform heat flux on top of the test module. Air from a compressed air line at gauge pressures of 6.86 bars was used as the coolant. Pressure regulators (Marsh, 0.1%) are used to control the outlet pressure of the compressor.

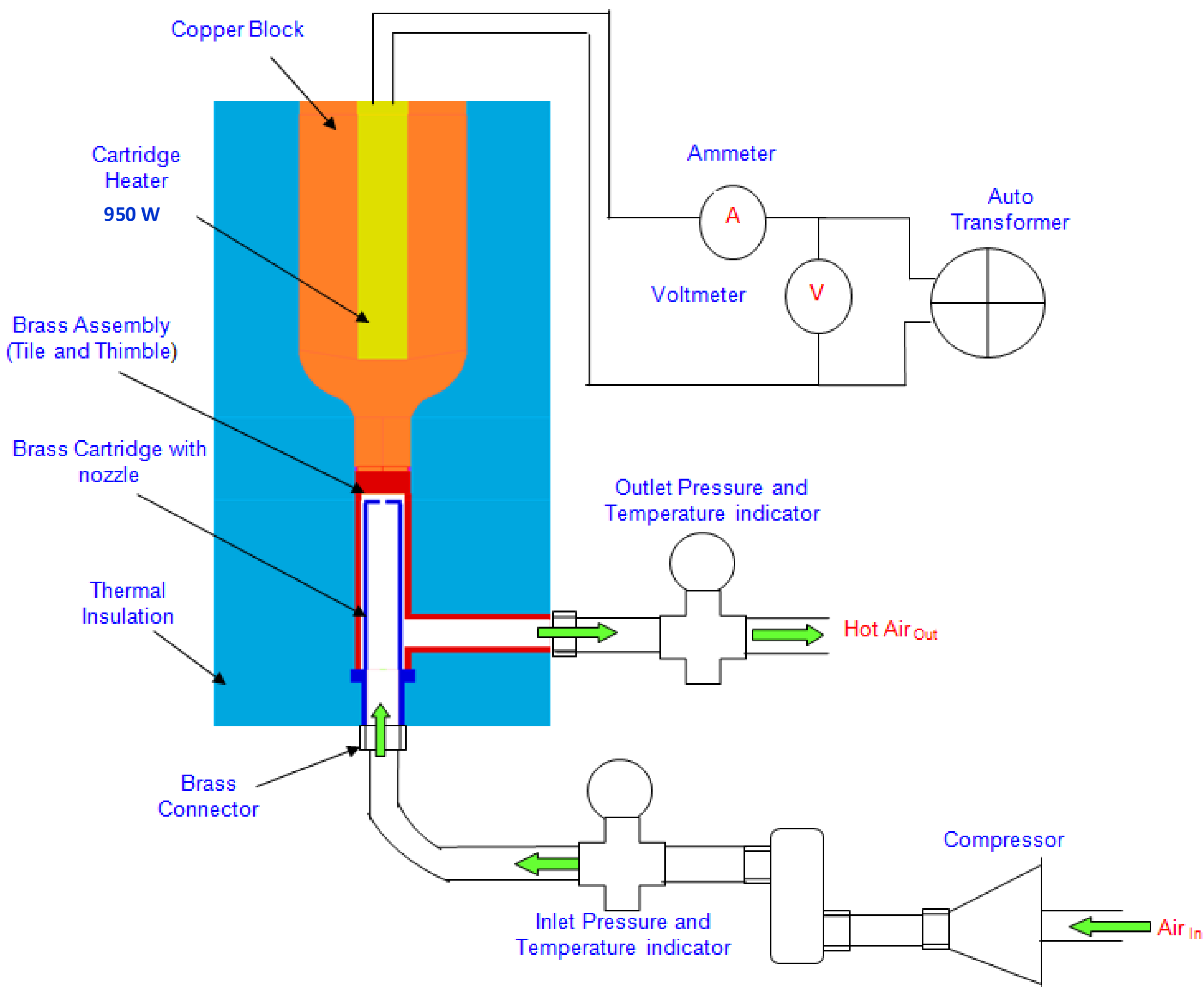

Fig. 4.6. Schematic of the experimental facility.

The compressed air was passed through a Rotameter before the test module and was finally discharged to atmosphere. The mass flow rate (m) through the test section, measured by the flow meter, was controlled by a 1/4" high pressure needle valve (Parker Autoclave, SW4071). Pressure transmitter (Marsh, ±1%) and Thermocouples (Omega, ±1°C) were used to measure the test section inlet/outlet pressures and temperature. The whole test section assembly was insulated with a thick glass wool layer.

The flow is considered to have “steady state”, when the temperatures measured by the TCs did not change more than 0.5°C over 10 minute intervals. Each experiment took approximately 30 minutes to reach steady state. The air inlet temperature was ~27°C. The mass flow rate of air was varied from 2 g/s to 7.5 g/s for Reynolds number 6.9×10^4 to 2.6×10^5. Energy balance validation shows a deviation of less than ~3.5% for the experiments over the whole Reynolds number range. A picture of the assembled test section with instruments attached is shown in Fig. 4.7.

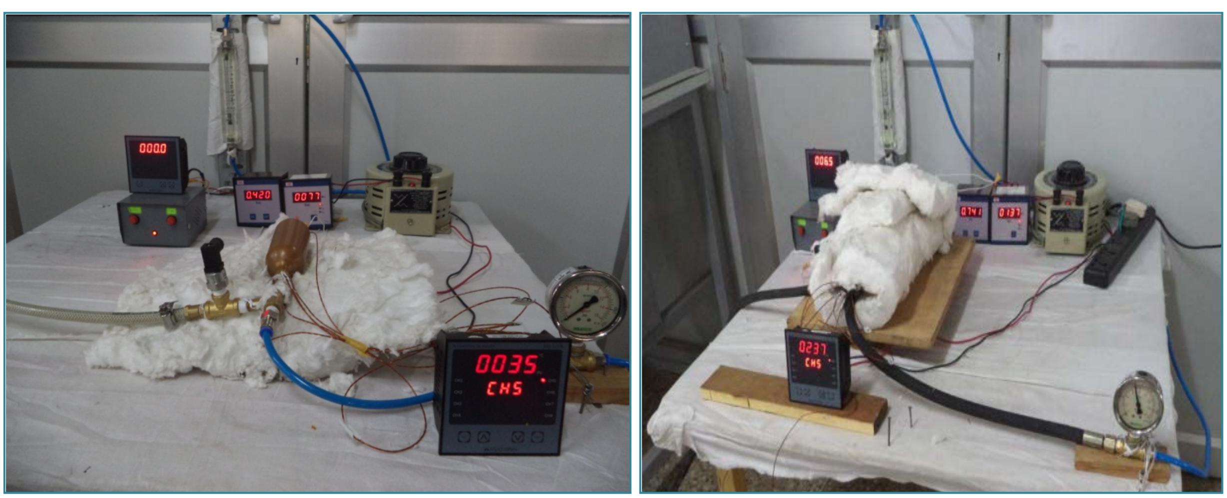

Fig. 4.7. Photograph of the assembled test section with instruments attached.

4.2. NUMERICAL APPROACH

4.2.1 Computational Model, Meshing and Boundary Conditions

Three dimensional and steady sate conjugate numerical simulations were performed, to predict flow and heat transfer characteristics in the finger mock up with and without sectorial extended surface. In order to validate the numerical results the heat transport in the solid wall and in the fluid and the boundary conditions were made identical to the experiments. A schematic of the test module used for the numerical simulation with boundary conditions is depicted in Fig. 4.8.

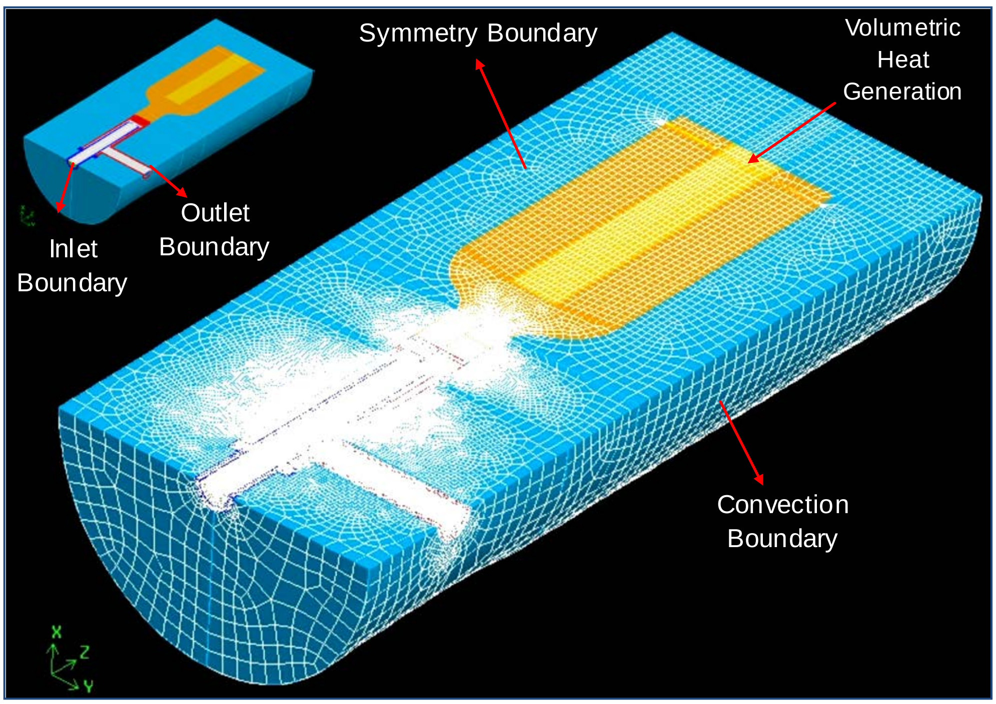

Fig. 4.8. Schematic symmetry sector of 180˚ computational model of the air loop mock-up.

Due to the presence of symmetry, one half of the test section (180° sector) is modeled in the present simulation. Temperature dependent material properties were adopted for all solid domains, namely jet cartridge, outer shell assembly, SES, cartridge heater and heat concentrator.

For all the simulations, the ideal gas assumption was used for the working fluid air. In the numerical model, experimental values of inlet temperature, mass flow rate (m) and power inputs to the heater such as volumetric heat generation were specified as a boundary condition. At the exit, the pressure outlet boundary condition was specified.

A natural convection boundary condition was imposed over all the other exterior surface of the model which was insulated with glass wool insulation and it was estimated through standard natural convection correlations [79]. Thermocouples are mounted on the outer surface of insulation to measure the surface temperature and to account for the convection heat loss from test module.

4.2.2. Mathematical Model

The realizable k–ε turbulence model was used, due to high Reynolds number and complicated geometrical model. This model accurately predicts the complex turbulent flows with rotation, boundary layers under strong adverse pressure gradients, separation, and recirculation [70, 77]. This model has been successfully used to simulate the flow and heat transfer in channel with pin fins [80, 81].

A second order discretisation scheme is used to reduce the numerical errors, and the SIMPLE algorithm was used to resolve the pressure-velocity coupling in the computation. The residual for declaring convergence was 10^{-4} for continuity and momentum equations. The same was 10^{-7} for the energy equation.

4.3. EMPIRICAL CORRELATION FOR THERMAL PERFORMANCE

4.3.1. Extraction of Heat Flux and Surface Temperatures

The heat flux is the ratio of net heating power (Q_{net}), to the area of the cooled surface, A_c = 13×10^{-3} m^2. The net heating power is the balance of total electric power supplied to the heater and the minor heat loss (estimated as 2 – 3.5% of total heating power) through the test module by natural convection. Figure 4.4 is the schematic view of the cooled surface showing the locations and the areas used to determine the area weighted mean temperature using various TC readings.

The average temperature of the cooled surface in the experiments was estimated from the TCs entrenched just below the cooled surface. The TC readings were first extrapolated to the cooled surface assuming conduction through 0.5 mm thickness of the brass shell using the calculated heat flux. These extrapolated temperatures were used to find the area weighted main plate temperature ($\overline{T}_c$) from,

$$\overline{T}_c = 2\pi \int_c T(r)\, r\, dr / A_c = 0.01\ TC_1^* + 0.10\ TC_2^* + 0.33\ TC_3^* + 0.55\ TC_4^* \qquad (4.2)$$

Where, `*' represents extrapolated readings of TCs at the cooled surface.

4.3.2. Extraction of Heat Transfer Coefficient

The thermal hydraulic performance of test section has been evaluated by considering various thermal parameters such as effective heat transfer coefficient (h_{eff}), effectiveness (ζ), efficiency (η) and pumping power (W). Details of the thermal parameters are given in the Section 3.3.2.

4.3.3. Error Analysis

The uncertainty in the experimental data has been determined by the standard error analysis method described by Bevington and Robinson [82]. The measurement error in net heating power (Q_{net}) and temperature are ±2.5 % and ±0.4 °C respectively, and the air property is ±1.1%. Based on this data, the measurement error in derived quantities h_{eff}, ΔP, η, W and ζ are respectively ±4.95%, ±5.6%, ±1.2%, ±6.1% and ±1.29%. The values are very small compared to the mean values of the corresponding quantities in the respective graphs. Hence, the error bar is not visible in the graphs.

4.4. RESULTS AND DISCUSSION

4.4.1. Grid Sensitivity Analysis

Identification of an optimum mesh size beyond which, the computed simulation is independent of the mesh size is the first step in computational simulation. The number of radial grid divisions on the periphery of the extended surface and in the nozzle is a useful constraint to determine the mesh for an accurate prediction of the cooled surface wall temperature. Towards this, an effort is made to investigate the sensitivity of the results to various computational grids, where the computational domain is examined for three grid systems, that is coarse (13×10^5), medium (15×10^5) and fine (18×10^5) grids. Figure 4.9 shows a detailed view for the medium grid around the extended surface and SES grid domain.

The grid sensitivity analysis was performed for Reynolds number of 6.9×10^4. The predicted results of mean surface temperature and pressure drop in the finger mock up are presented in Fig. 4.10 for various grid counts. It is clear that the surface temperature and pressure drop of test section do not change significantly between the medium grid and fine grid. The maximum relative deviation of the two variables is within 4.5%. However, it is found that the computational time required for each iteration in the case of fine mesh is large compared to that of the medium grid. Therefore, the medium grid has been chosen for further investigations.

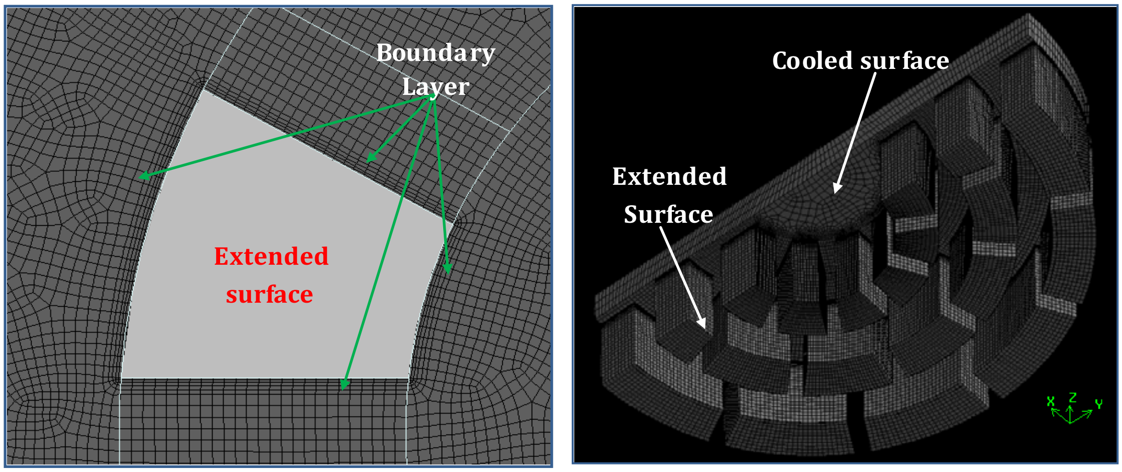

(a) (b)

Fig. 4.9. Computational grid near the extended surface (a) expanded view of medium grid and (b) surface mesh.

The y^+ value is also an important criterion in the numerical simulation for the accuracy of predictions for wall shear stress and heat transfer near the solid/ fluid interface region. To capture the heat transfer performance close to the wall, meshing with denser grids was adopted by using a boundary layer mesh as depicted in Fig. 4.9. In the present study, y^+ values were maintained around ~1 [70]. The measured value of wall temperature for Re = 6.9×10^4 is 154 ˚C. The corresponding value predicted in the medium grid is 151 ˚C and it compares satisfactorily with the experimental data.

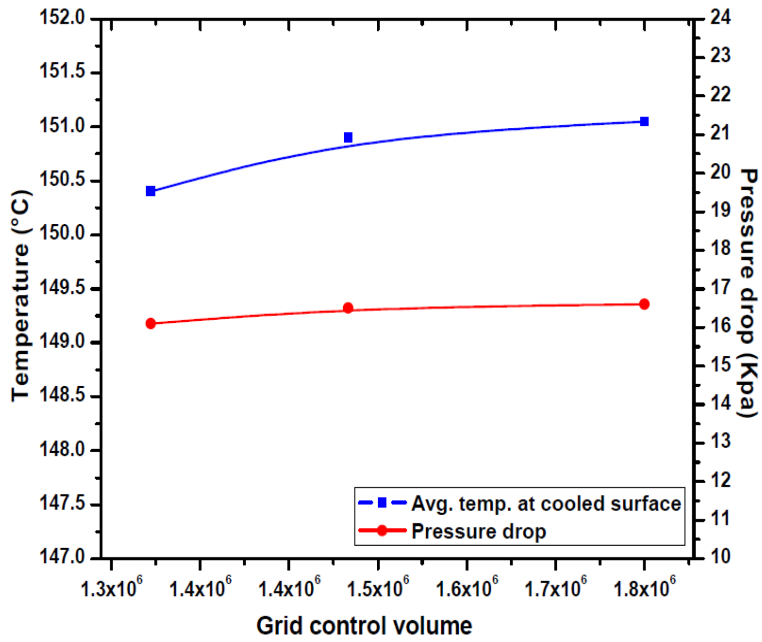

Fig. 4.10. Results of grid sensitivity analysis.

4.4.2. Comparative Studies of the Thermocouple Temperatures

The thermocouple temperatures in the test section with and without SES have been measured in the Reynolds number range of 6.9×10^4 to 2.6×10^5. The comparison between computed thermocouple temperatures against the experimental data for different Reynolds number is depicted in Fig.4.11. It is seen that the local surface temperatures of the test module decrease with an increase in Reynolds number as expected, but the reduction is more in case with SES.

The wall temperature exhibits a radial non-uniformity to the extent of 4 to 6 ˚C. This is expected since coolant temperature increases along the flow direction. The temperature values at thermocouples location obtained from the simulation are in satisfactory agreement with the experimental results with maximum deviation less than 5 ˚C. Predicted wall temperatures are consistently less than the measured data.

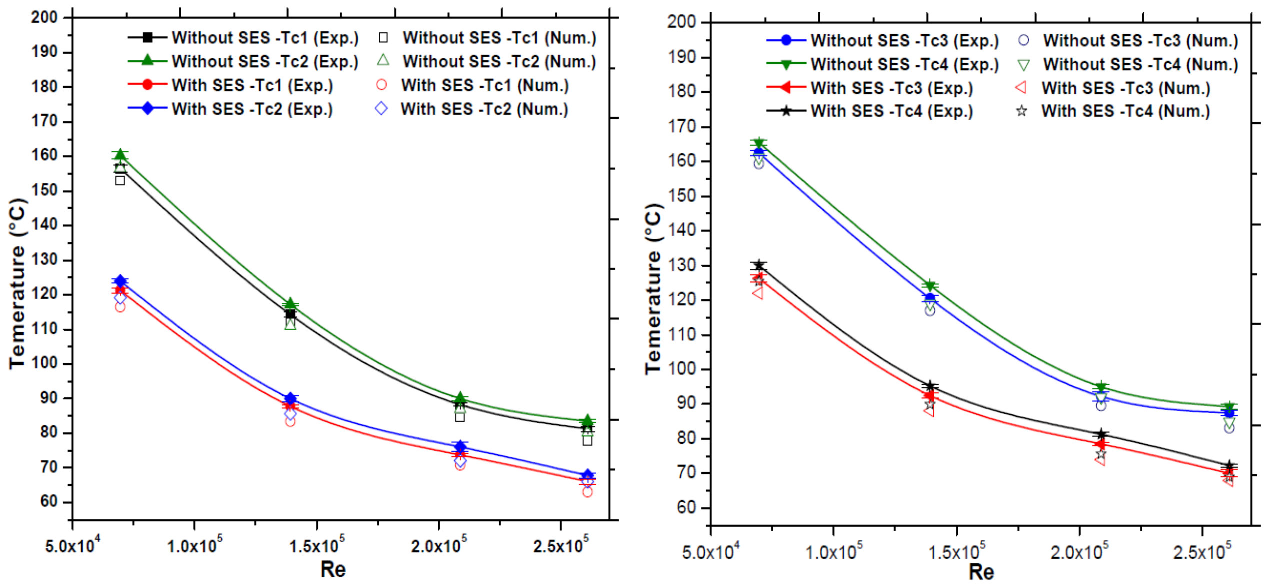

Fig. 4.11. Comparisons of measured and predicted thermocouple temperatures (a) TCs 1-2 and (b) TCs 3-4 at various Reynolds number.

4.4.2.1. Discussion on Temperature Drop by SES

The temperature distributions in the target plate with/without SES, as predicted by the mathematical model are depicted in Fig. 4.12 for Re = 1.3×10^5. It is seen that for identical heat flux, addition of SES in the design reduces the plate temperature appreciably. It is due to the improvement in the effective heat transfer coefficient by SES, as a result of increase in surface area and turbulence.

Further, the surface temperature of the test section at the center (TC-1) drops down rapidly while it increases in the radial direction. The rapid decrease in temperature at the center is due to the direct impingement of a high velocity jet, which leads to high heat dissipation that is clearly evident in Fig. 4.12. Similar trends are observed in the experiments also. These results suggest that the heat transfer efficiency is improved with the provision of SES.

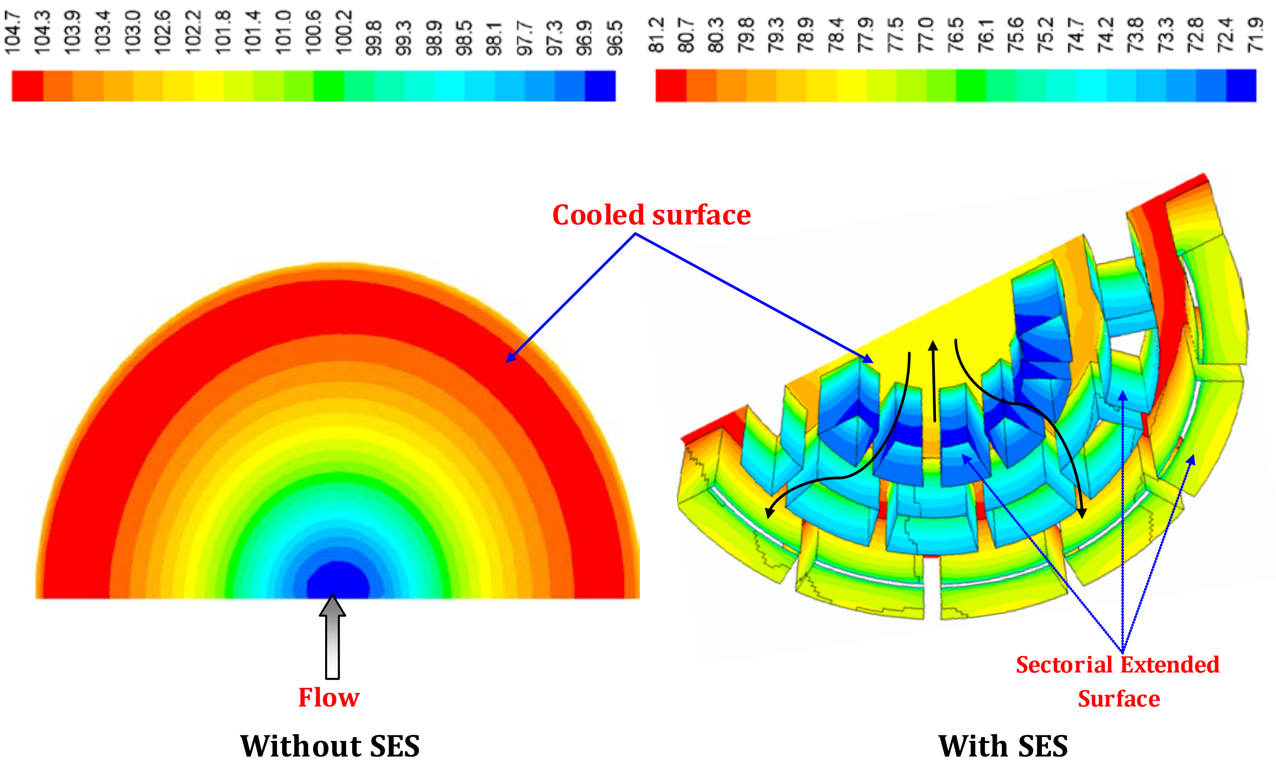

Fig. 4.12. Comparison of predicted temperature (˚C) distribution over the cooled surface at Re=1.3×10^5.

4.4.3. Comparative Studies on Pressure Drop by SES

Pressure drops in the test section were measured for a heat load ~0.75 MW/m^2 at various Reynolds numbers. Figure 4.13 compares the measured pressure drop against numerically predicted pressure drop, with and without SES in the test section. The predicted and measured results exhibit identical trends.

The pressure drop in the test module with the presence of SES arrays is higher than that without the SES module, as the fluid has to cross a series of barriers provided by the SES. It can be observed that the numerical results of the both the test modules are in satisfactory agreement with the experimental results at the low Reynolds number (~1.5×10^5). Deviation observed between the measured and predicted results for both configurations is ~8% at the prototypical Reynolds number.

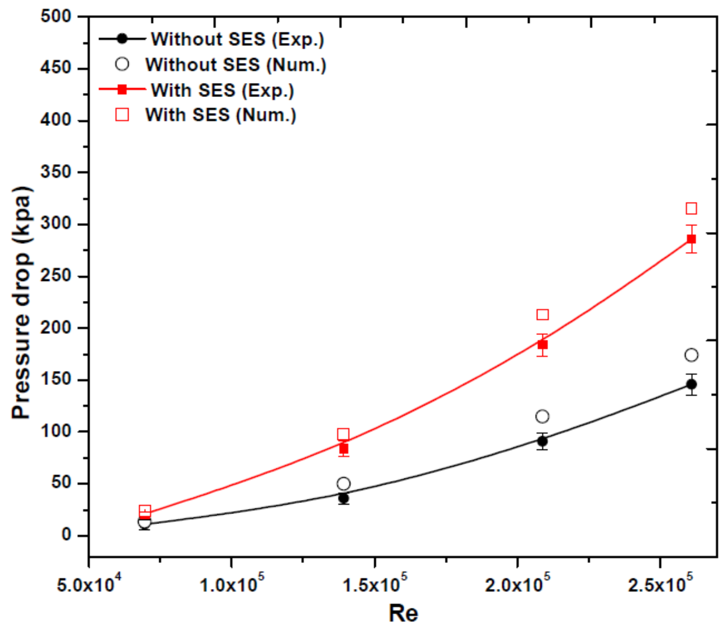

Fig. 4.13. Comparisons of the measured and predicted pressure drop against Re.

4.4.3.1. Correlation for Loss Coefficient

An engineering parameter of practical interest is the pressure loss coefficient. It is essential to know its dependence on the Reynolds Number. The functional relationship for loss coefficient can be written as:

- $K_L = f_n\,(Re)$

The loss coefficient (K_L), based on the coolant property and measured pressure drop (ΔP) across the test module is determined from,

- $K_L = \dfrac{\Delta P}{\rho v^2/2}$ (4.3)

Where, v stands for the mean velocity of the jet. The data corresponding to all experimental tests for both the configurations have been used for determination of K_L. Based on this, the following relationships have been developed:

- $K_L = 2.6271\ Re^{-0.1708}$ (Without SES) (4.4)

and

- $K_L = 3.8251\ Re^{-0.1379}$ (With SES) (4.5)

The R^2 values for these equations are 0.996 and 0.992, respectively.

4.4.3.2. Discussion on Pressure Drop by SES

In order to develop further understanding into the effect of SES on the pressure drop mechanism, a comparison of the contour and vector plots of the stream wise velocity distribution on *x*-*y* plane of both the configurations is depicted in Fig. 4.14. It can be seen, from Fig. 4.14(b) and Fig. 4.14(c), that a high velocity jet flow and symmetric vortices are generated in the vicinity of the extended surface as compared to the case without SES.

Due to the formation of vortex and high velocity, turbulence level increases, leading to the associated increase in heat transfer coefficient. However, the eddies and flow acceleration caused by blockage, increase the pressure loss in SES.

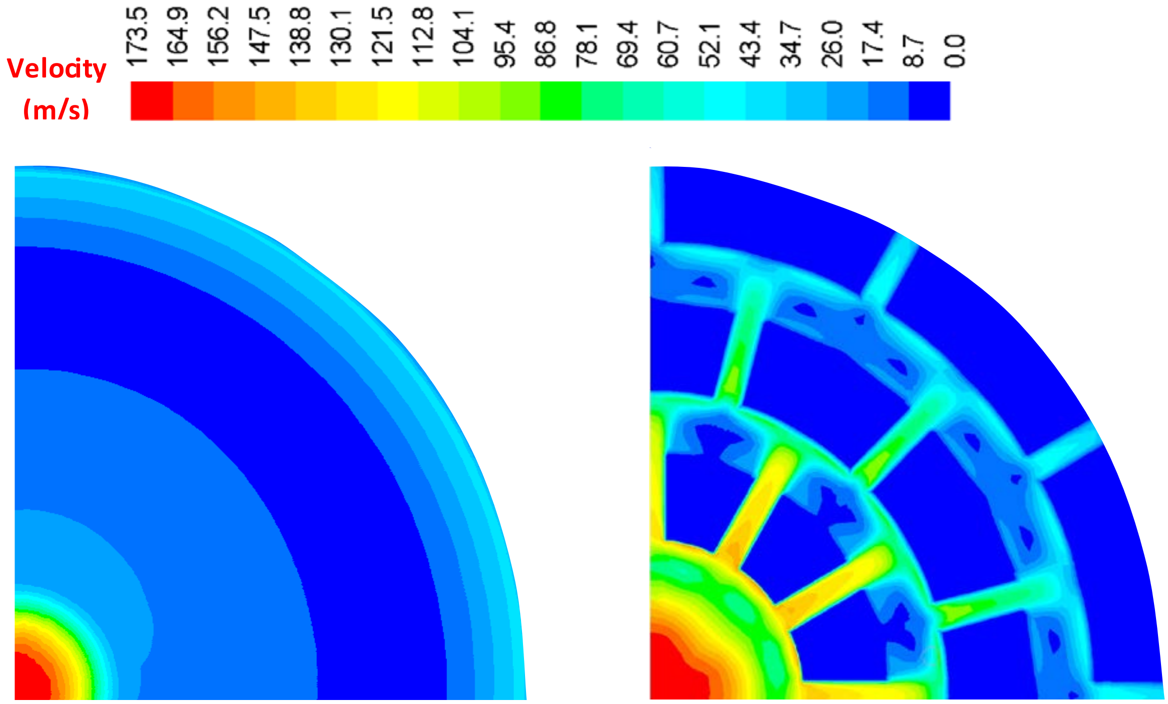

(a) Without SES

(b) With SES

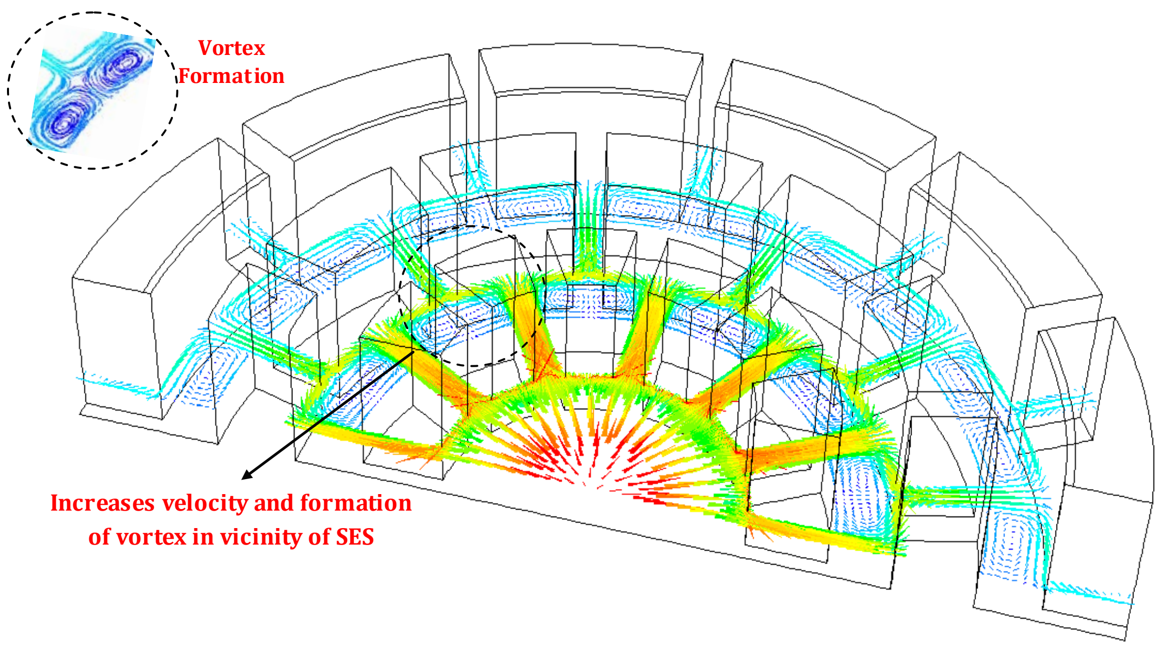

(c) Vector plot with SES

Fig. 4.14. Comparison of velocity (m/s) distribution on *x*-*y* plane at a distance of 0.5 mm from the cooled surface at Re = 1.3×10^5.

4.4.4. Comparative Analysis of Heat Transfer by SES

For the experimental test section shown in Fig. 4.1, thermal performance has been analyzed to find the efficacy of SES. A comparison of experimental data predicted by three-dimensional conjugate analysis is presented in Fig. 4.15. Effective heat transfer coefficient of the test section with SES is significantly larger than the case without SES for the entire Re range. As expected, the effective heat transfer coefficient is large with SES, as it offers a relatively large surface area. Also, due to a proper layout of the SES, all the walls of the extended surface are forced to participate in the heat exchange process.

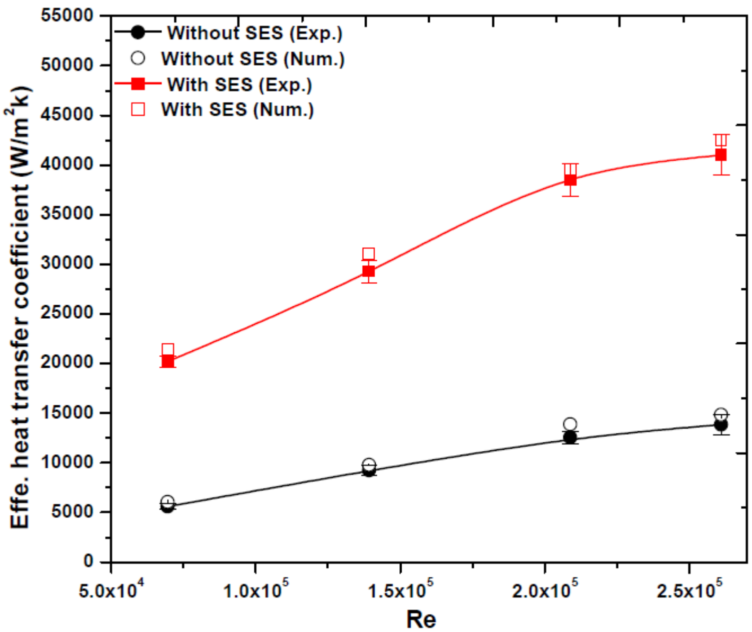

Fig. 4.15. Comparison of the measured and predicted effective heat transfer coefficient.

It can be seen from Fig. 4.15 that the predicted values of h_{eff} are in good agreement with the experimental values for the entire range of Reynolds number. The maximum deviation between the measured and predicted results at the prototypical condition for both configurations is less than 6.5%. The numerical simulation is reasonably accurate in predicting the heat transfer enhancement potential of the test section with SES. This serves as a validation for the computational model which is the most important consideration in the mock up design for the divertor.

4.4.4.1. Correlation for Nusselt number

The intensity of heat exchange between the cooled surface wall and flowing fluid is described by the Nusselt number (Nu). The Nusselt number over the cooled surface is determined from h_{eff}, jet diameter and thermal conductivity of air evaluated at the bulk fluid temperature. From the above description and data presented in Fig. 4.15, it is found that the Nusselt number has also strong relationship with Re. The average Nu can be correlated as,

- $Nu = C\ Re^n$

The values of coefficient `C' and exponent `n' have been determined from the experimental data and curve fitted as a function of Re, from which the following correlation for the Nusselt number are proposed.

- $Nu = 0.1488\ Re^{0.71}$ (Without SES) (4.6)

and

- $Nu = 2.2762\ Re^{0.578}$ (With SES) (4.7)

The values of R^2 for above equations are 0.995 and 0.983, respectively.

These correlations are valid for Re number range of 6.9×10^4 to 2.6×10^5, and Pr ~ 0.7 used for the present experiments.

4.4.4.2. Discussion on Heat Transfer by SES

From Fig. 4.12, it is seen that in the present design, the SES offers a relatively large surface area to the volume ratio. Further with an appropriate arrangement of the SES, satisfactory coolant velocity can be achieved on the entire surface. Also, since the extended surfaces are short, efficiency and effectiveness are expected to be very high (Section 4.4.5). Thus, the addition of SES greatly enhances the heat transfer performance of the present design.

4.4.5. Comparative Analysis of Thermal Hydraulic Performance

The performance of the extended surface is determined by both the efficiency (η) and effectiveness (ζ). Effectiveness of extended surface gives the quantity of additional heat dissipated by the extended surface. It should be large to keep the extra cost of adding the extended surface as low as possible. On the other hand, by determining the efficiency of an extended surface, one can assess the heat transferring capacity of the extended surface.

Figures 4.16(a) and (b) show the variations of η and ζ illustrating the performance of SES as a function of Re. As expected, when the Re increases in the SES, both η and ζ decrease due to the increase in heat transfer coefficient. At the prototypical operating conditions, the values of η and ζ for air are ~ 89 % and 2.98, respectively. This result suggests that extended surface could potentially enhance thermal performance when compared with its bare counterpart. The values of efficiency and effectiveness predicted from the three dimensional conjugate heat transfer computations are also presented in Fig. 4.16. It is found that, satisfactory agreements between the experimental and numerical results exist with maximum deviations of 0.9% for η and 1.2% for ζ

.

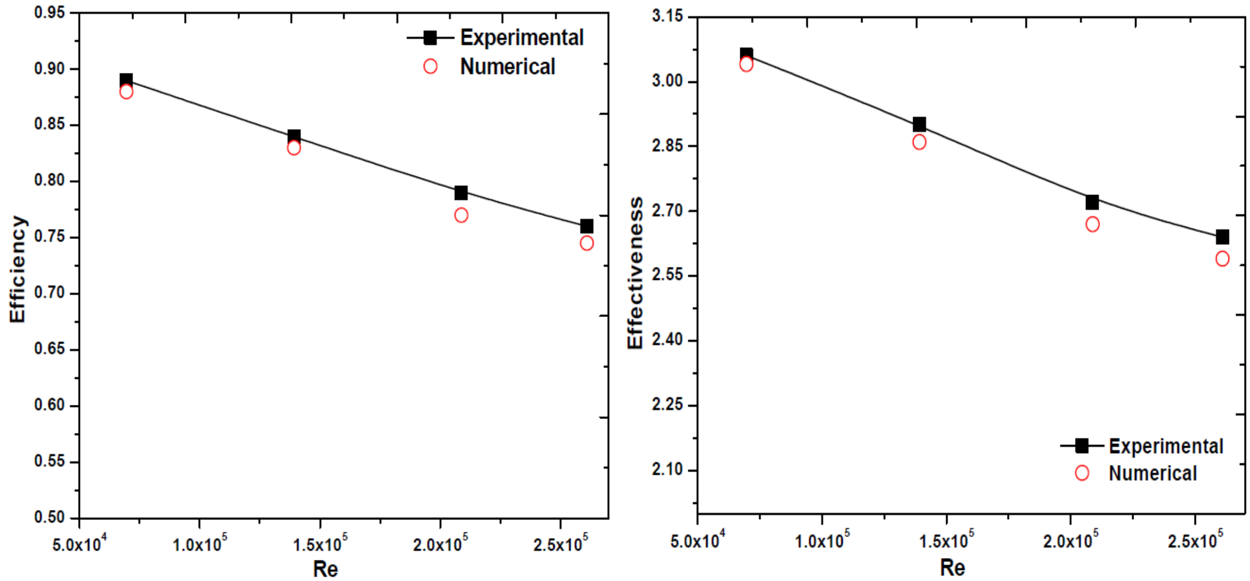

(a) (b)

Fig. 4.16. Comparison of measured and predicted data, (a) efficiency of SES and (b) effectiveness of SES.

Figure 4.17(a) depicts the pumping power required for air flow through the test section as a function of Re at a constant heat flux. It is seen that, the pumping power (W_{air}) constantly increases with Re in both cases of with and without SES. However, W_{air} required for the case with extended surface is significantly higher at the same Re, due to increase in the pressure drop by the SES.

Figure 4.17(b) compares the variation in the effective heat transfer coefficient (h_{eff}) with pumping power with/without extended surface. From the figure, it can be observed that h_{eff} continuously increases with W. But at identical pumping power, the test section with extended surface offers a higher h_{eff} as compared to that without SES. When the experimental data are extrapolated to the prototypical operating conditions, the pumping power for the extended surface test section is found to be 25% greater and h_{eff} increases by more than the double, compared to the bare test section.

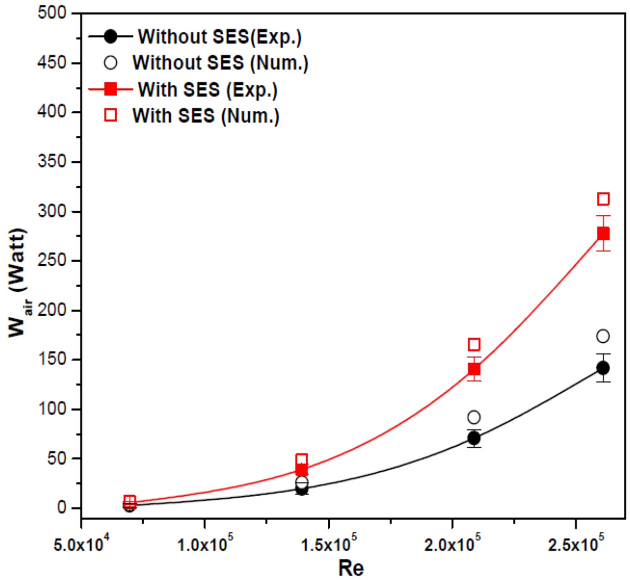

(a)

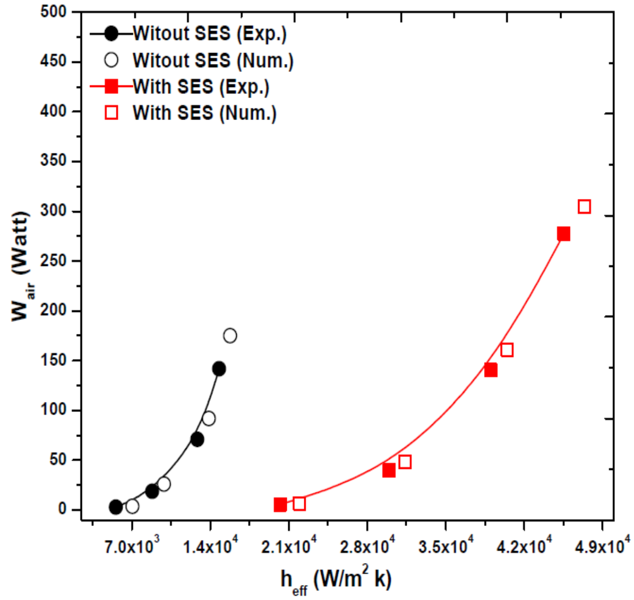

(b)

Fig. 4.17. (a) Dependence of pumping power on Reynolds number and (b) Pumping power as a function of the $h_{eff.}$

4.5. CLOSURE

An experimental and computational approach has been proposed for the evaluation of thermal hydraulics performance of a finger type divertor. Experiments have been performed on a full scale "finger" type test mock-ups respecting geometric and dynamic similarities. Both without SES and with SES test mock-up have been tested in air (which represents helium in the prototype) for a wide range of Reynolds number. The geometric parameter of the divertor with sectorial extended surface resembles that of future fusion power plant.

The experimental data on pressure drop, heat transfer coefficient, SES effectiveness and SES efficiency have been used as a benchmark for validation of conjugate 3-D numerical model including realizable k–ε turbulence model. Heat concentrator with electrical heater has been developed for simulating incident high heat flux similar to that of plasma heating. Both the finger mock-ups have been numerically simulated towards validation of the numerical model. It is seen that the effective heat transfer coefficient increases more than double with the addition of SES at the cost of ~25% higher pumping power. The efficiency and effectiveness of the SES are found to be ~ 89% and ~2.98, respectively at the prototypical Reynolds number 1.1×10^5. The numerical results of effective heat transfer coefficient compare satisfactorily with the experimental data within 6.5% at the prototype Reynolds number. Suitable correlations have been derived for Nusselt number and pressure loss coefficient in the finger mock-up as a function of Reynolds number.

CHAPTER 5

GEOMETRIC OPTIMIZATION OF DIVERTOR HEAT SINK WITH SECTORIAL EXTENDED SURFACES

5.0. INTRODUCTION

In the previous chapter, an experimental and computational approach has been discussed for the assessment of thermal hydraulic performance of a finger mock-up design with proposed SES. The results of previous study encouraged to use the numerical method for the design of the divertor. Therefore, in the present study "*the effect of geometric variation on the thermal performance is evaluated, and an optimal design of SES is found through numerical simulations*". The principal aim of the optimization study is to reduce the 'thimble' temperature as much as possible below the brazing filler temperature (1050°C) to enhance the life of divertor finger mock-up design with SES, and simultaneously limit the pressure drop to a reasonable value to save pumping power.

Various non-dimensional design variables, viz., relative pitch, thickness, jet diameter, the ratio of height of SES to jet diameter and circumferential position of the SES are considered for the present optimization study. The effects of design variables on thermal performance of the divertor are evaluated in the Reynolds number (Re) range of 7.5×10^4 to 1.2×10^5. The analysis reveals that, the heat transfer performance of finger mock-up with SES is improved for two optimum designs having relative pitch and thickness of 0.30 and 0.56 respectively. Also, it is observed that finger mock-up heat sink with SES performs better, when the ratio of "SES height" – to - "jet diameter", reduces to 0.75 at the cost of marginally higher pumping power. The effects of jet diameter and circumferential position of SES are found to be counterproductive towards the heat transfer performance. To understand the stress distribution in the optimized geometries, a combined computational fluid dynamics and structural analysis have been carried out. It is found that deviation in peak stresses among various optimized geometries is not significant.

5.1. PROBLEM DESCRIPTION

5.1.1. Computational Domain, Numerical Approach and Boundary Conditions

For the present analysis, 30º sector of divertor finger mock-up with various geometric configurations of SES (as discussed in the Chapter 3) is adopted. To optimize the design of the divertor finger mock-up with SES, overall comparisons are necessary among different geometric configurations of SES. In order to compare the performance of various designs of divertor finger mock-up with SES, the incident heat flux, coolant inlet temperature and pressure are maintained at $10 MW/m^2$, 600 ˚C and 10 MPa respectively. Thermal hydraulic performance of finger mock-up with SES has been analyzed for a wide range of Re number from 7.5×10^4 to 1.2×10^5.

5.1.2. Mathematical Formulations

The following mathematical formulas are used to compare the thermal hydraulic performance of the finger mock-up design for various configurations of SES.

The Reynolds number based on the hydraulic diameter of the jet is defined as:

❖ $$Re = m\, D/(\mu\, A_{jet}) \tag{5.1}$$

Where, the A_{jet} is the area of the jet, m is mass flow rate, μ is the dynamic viscosity of helium, and D is the diameter of the jet.

Pressure drop (ΔP) is one of the most important factors, which reflects the hydraulic performance of the finger mock-up and is calculated by,

- $\Delta P = P_{in} - P_{out}$ (5.2)

Where P_{in} and P_{out} are the coolant pressures at inlet and outlet of the finger mock-up.

The pumping power which is required to circulate helium in the finger mock-up at mass flow rate m, to cool the target surface is determined by,

- $W = (m/\rho)\,\Delta P$ (5.3)

The pumping power ratio (J) is defined as:

- $J = W/Q_T$ (5.4)

In the above equation ρ is the density of helium at the bulk temperature $(T_{in} + T_{out})/2$, and ΔP is the pressure drop across the divertor finger mock-up section. Additionally, Q_T is the total incident power on test mock-up, and W is the power required to circulate helium through the finger mock-up.

5.2. RESULTS AND DISCUSSION

5.2.1. Effect of Reynolds Number on Heat Transfer

The non-dimensional velocity (U/U_{in}) contours and the pathlines in a plane at height Z=1 mm from target surface at various mass flow rates for the reference case (case 'B') [83] is depicted in Fig. 5.1. It can be seen that at the low mass flow rate, the flow field is smooth without any zones of recirculation. However, as mass flow rate increases, standing vortex pair is observed in the wake region of central SES, with further increase in the helium flow rate intense recirculation zones appear behind the middle row of SES also. These intense recirculation enhance the heat transfer when compared to a smooth channel.

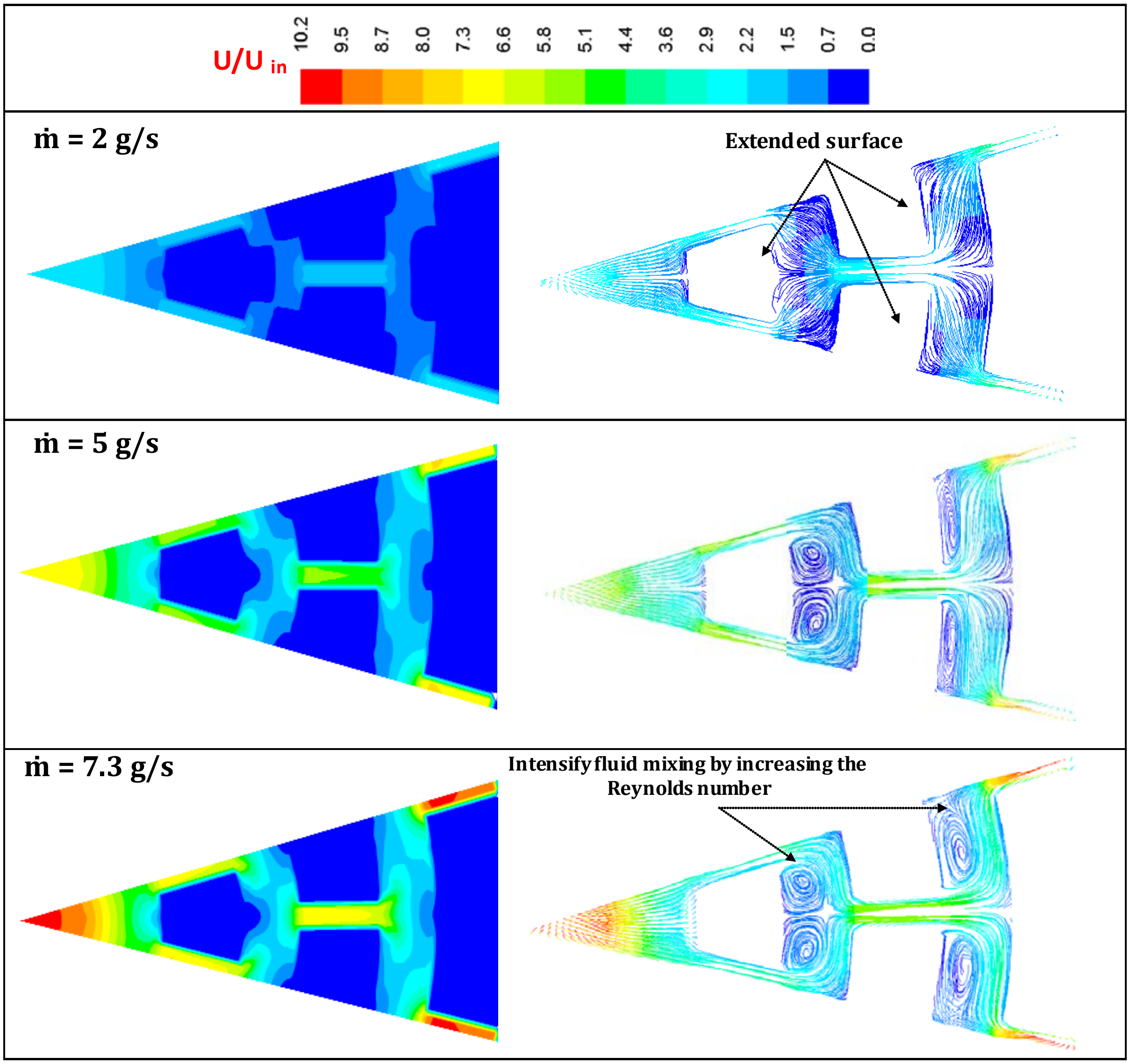

Fig. 5.1. Non-dimensional velocity contours and the pathlines in x-y plane at a distance of 1 mm from the target surface at different mass flow rates.

For example, the contour of turbulence kinetic energy (TKE) at an identical mass flow rate for the case of smooth channel and a channel with SES is depicted in Fig. 5.2. It is seen that the

TKE is maximum at the entrance due to high velocity and acceleration of the fluid through a jet impingement. But provision of SES has enhanced the level of turbulence in the mainstream, particularly around the SES walls due to vortex formulation.

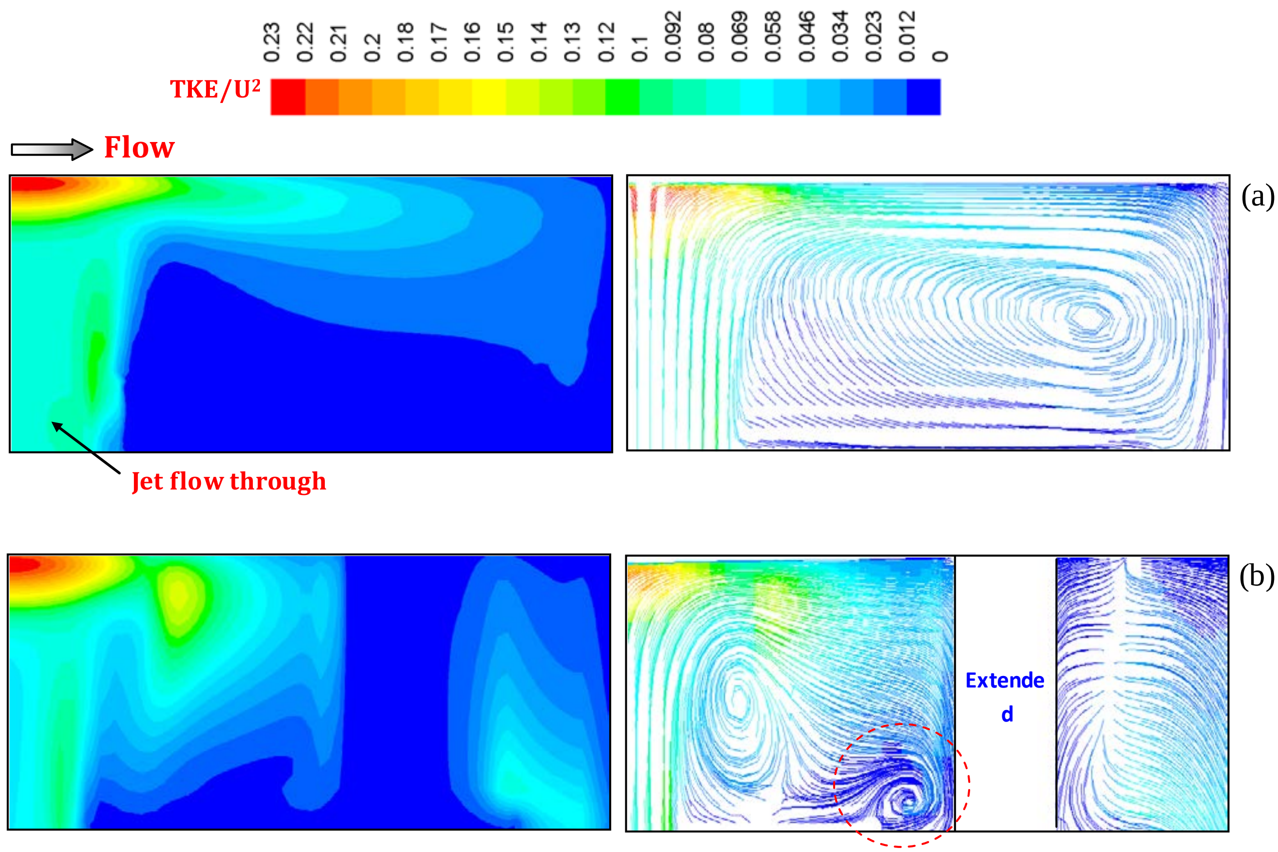

Fig. 5.2. Comparison of turbulent kinetic energy distribution and pathlines in *y*-*z* plane (a) without SES and (b) with SES at Re = 1.10×10^5.

Figure 5.3 presents the non-dimensional temperature contours of the target and extended surface walls at various mass flow rates. It is observed that, the temperature distribution at the front row of the extended surfaces has a lower average temperature compared to the SES in peripheral row. This is due to a lower average temperature of coolant at the inner row of extended surface, which continuously increases when the fluid passes from inner to outer arrays of SES. It is clearly seen from the figure that the peak temperature at the hot surface decreases as the mass flow rate increases. The presence of horseshoe vortices (Fig. 5.1) and the increase in surface area for interaction of coolant causes higher temperature gradients. Therefore, a higher heat transfer coefficient and a lower average wall temperature are attained.

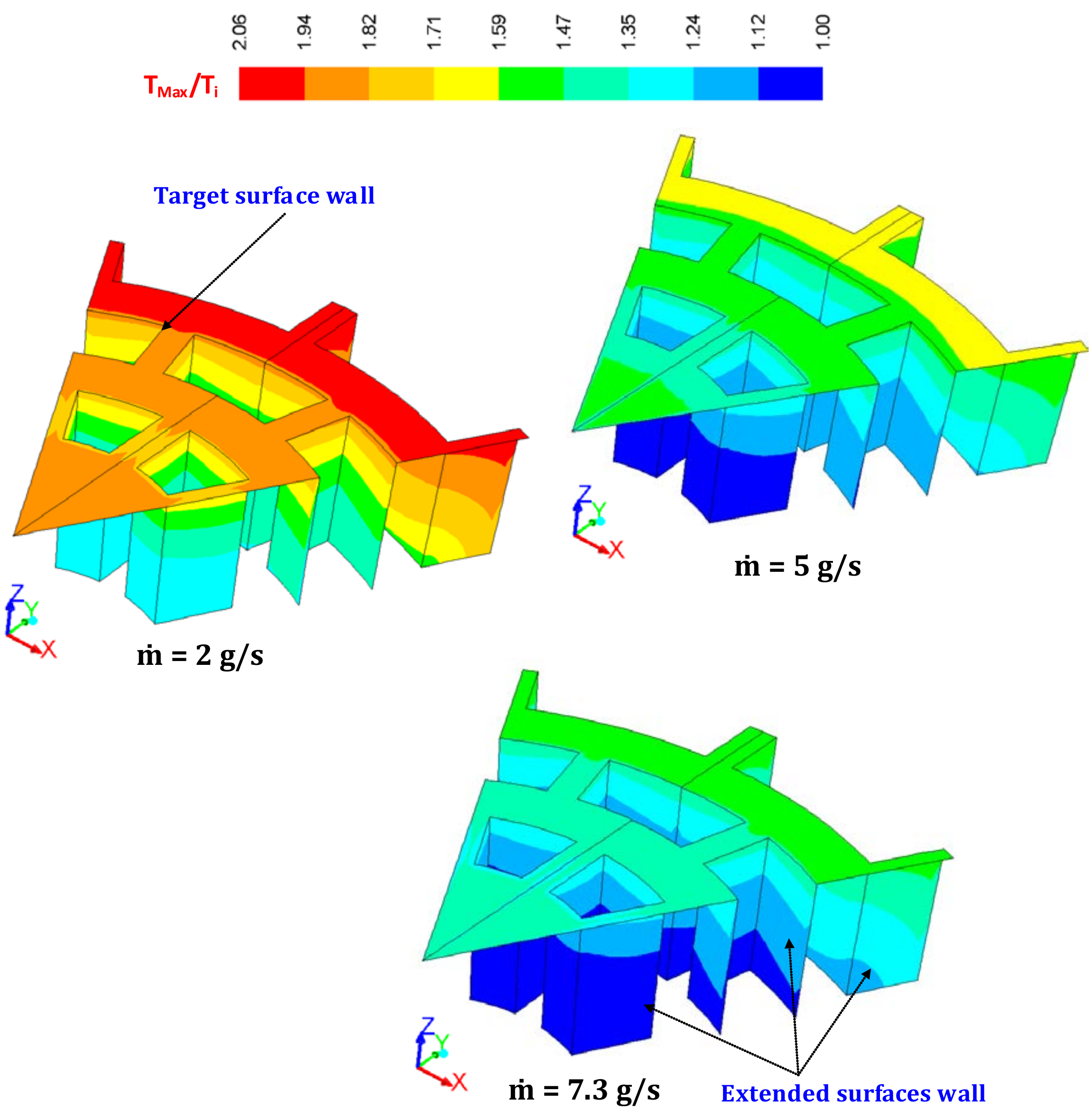

Fig. 5.3. Non-dimensional temperature contours for reference case 'B' at various mass flow rates.

5.2.2. Appropriate Location of Central SES

Detailed studies on the distribution of heat transfer coefficient due to impingement of central jet has been carried out for placing first row of SES at the appropriate location to maximize heat transfer enhancement. This study is extremely important because due to the close proximity of the extended surface at the center, jet does not diffuse easily and hence leading to a higher pressure drop. The predicted variation of the local wall heat transfer coefficient along radial position on the target surface for divertor without SES is shown in Fig. 5.4.

It is seen that the heat transfer coefficient is maximum in the central region of the plate due to high fluid velocity emanating from the jet, and starts to decrease gradually beyond 1.9 mm. Hence, the first row of extended surface should be provided outside of the peak heat transfer zone that will enhance the performance of the extended surface with a minimum pressure drop.

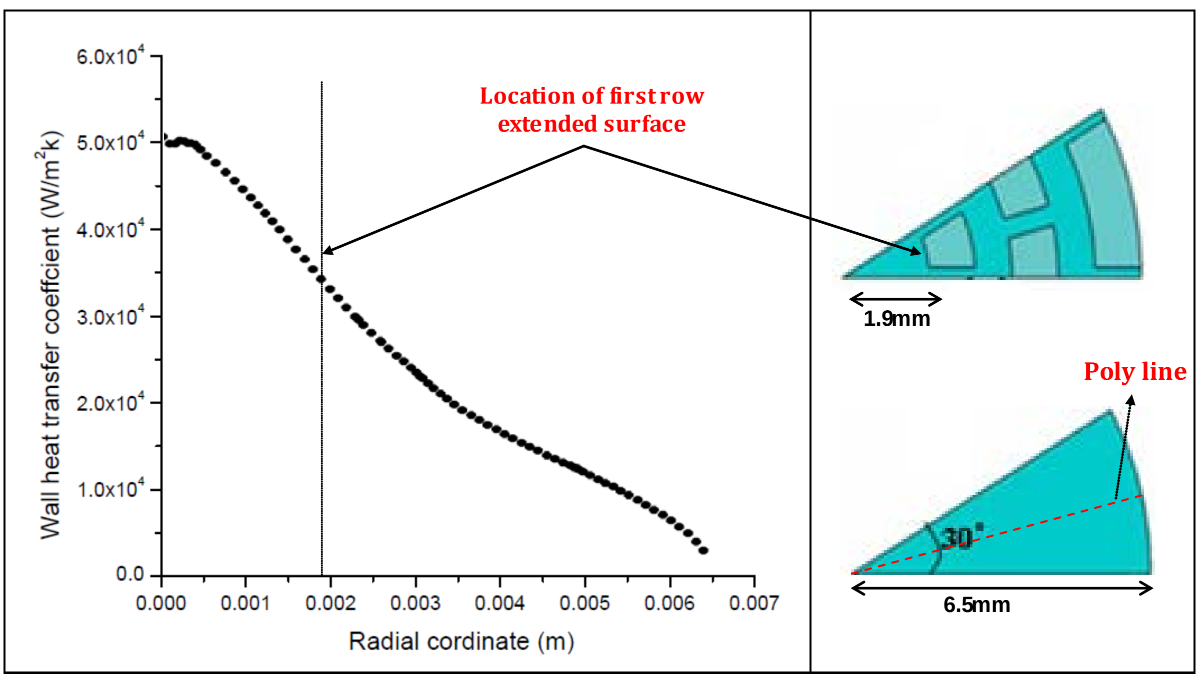

Fig. 5.4. Schematic of variation in heat transfer coefficient along radial position at target surface for divertor without SES (case 'A').

5.3. EFFECT OF DIFFERENT PARAMETERS ON FINGER MOCK-UP PERFORMANCE

An elaborate parametric study has been performed to find the effect of each heat sink parameter on heat transfer and pressure loss. Here, the most vital design parameter of interest is maximum thimble temperature, which is limited by filler material melting temperature in brazed joint. In order to achieve best cooling performance, various cases for non dimensional geometric parameters such as relative pitch (δ_p = p/h), thickness (δ_t = t/h), the ratio of SES height to jet diameter h/D, the circumferential position of SES (β°), and jet diameter (D) have been investigated for the divertor finger mock-up. For each case a wide range of parameter is considered, while the other geometric parameters are kept constant. Geometrical details of the various cases studied are presented in Table 5.1.

Table 5.1: Geometric dimension of finger mock-up for various studied cases (all dimensions in mm).

Cases	**Pitch (p)**	**Thickness (t)**	**Height** (h)	**Jet Diameter** (D)	**No. of SES**	**Circumferential position of SES (β°)**
A	-	-	-	2	-	-
B	0.8	1	2	2	36	30°
C	0.7	1	2	2	36	30°
D	0.6	1	2	2	36	30°
E	0.5	1	2	2	36	30°
F	0.6	1.13	2	2	36	30°
G	0.6	0.9	2	2	36	30°
H	0.6	0.6	2	2	36	30°
I	0.6	0.5	2	2	36	30°
J	0.6	1	1.5	2	36	30°
K	0.6	1	1.2	2	36	30°
L	0.6	1	2.5	2	36	30°
M	0.6	1.13	1.5	2	36	30°
N	0.6	1.13	2.5	2	36	30°
O	0.6	1	2	1.7	36	30°
P	0.6	1.	2	1.5	36	30°
Q	0.6	1	2	2	54	20°
R	0.6	1	2	2	72	15°

Case 'A' denotes the case of divertor without SES, whereas case 'B' is considered as the initial reference case with extended surface for the optimization studies. Schematic of a few cases studied is depicted in Fig. 5.5. All the results are compared at the prototypical Reynolds number (Re = 1.1×10^5), which is corresponding to mass flow rate of 7.3 g/s [83].

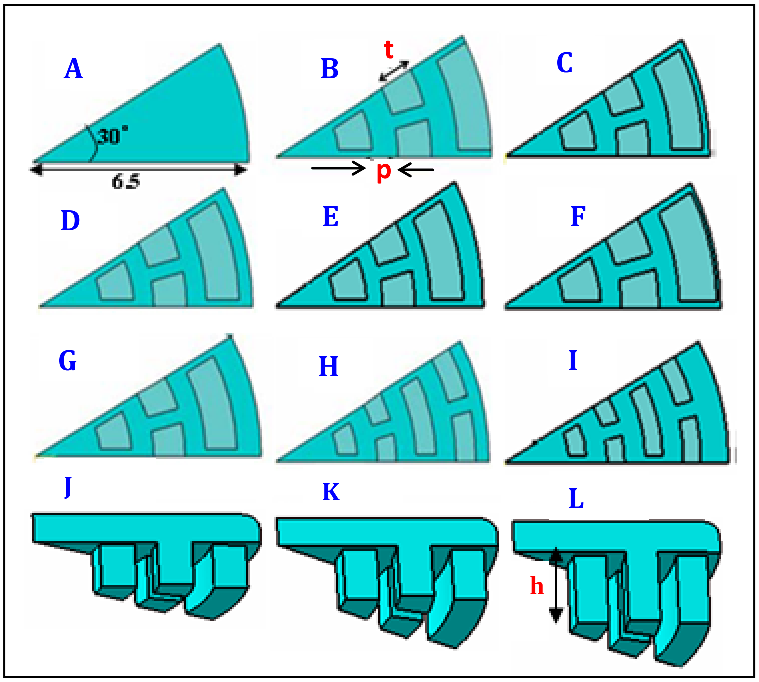

Fig. 5.5. Schematic of few studied cases for finger mock-up with SES.

5.3.1. Comparison of Finger Mock-Up at various SES Relative Pitch

A comparison of tile and thimble temperature among different SES relative pitches (δ_P) with same SES height (h = 2 mm), thickness (t = 1 mm), and Circumferential position (β = 30°) are shown in Figs. 5.6(a) and (b). It can be noticed that, the tile and thimble temperatures initially decrease with a reduction in the SES spaces at the identical Re numbers. This suggests that the relative pitch makes the vortices stronger, and intensifies the fluid mixing causing high heat transfer rate.

Temperatures of tile and thimble reduce as relative pitch decreases up to 0.30 (case 'D'), and further decrease in pitch (case 'E') leads to an increase in tile and thimble temperature, presumably due to the trap of coolant between the vicinity of SES. The lowest tile and thimble temperatures achieved in case 'D' are lower by ~14 °C and ~18 °C respectively, compared to the reference case 'B' at identical prototypical Re.

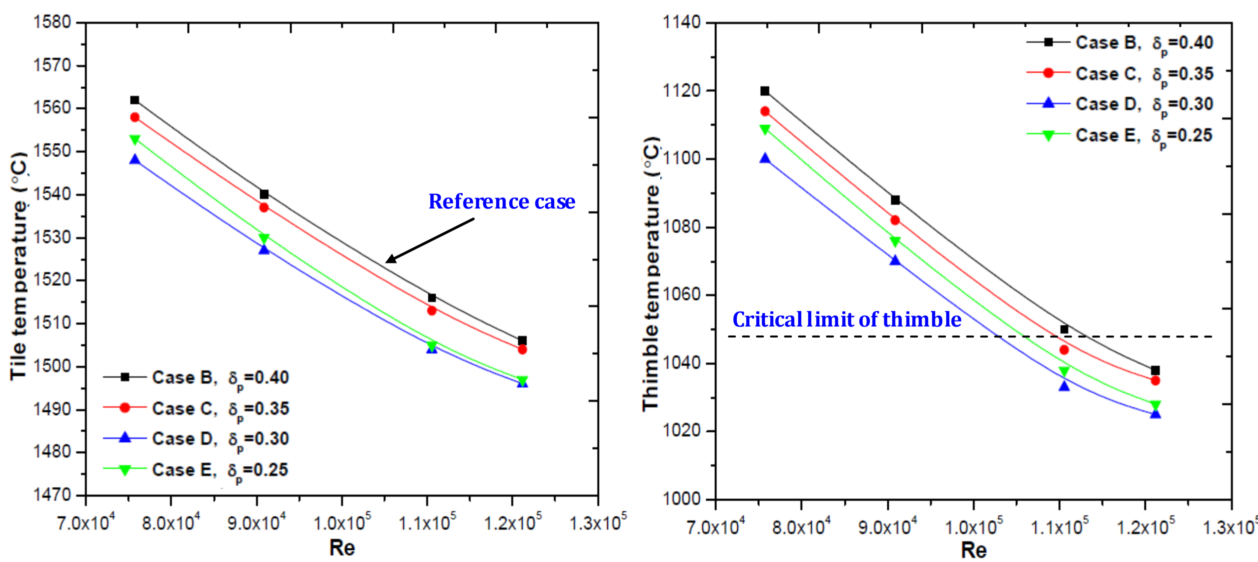

(a) (b)

Fig. 5.6. Comparison of (a) tile, and (b) thimble temperature against Re with different δ_p.

Figures 5.7 (a) and (b) present the variation in the pressure drops (ΔP) and pumping power ratio (J) as a function of Re number and pitch. It is clear that both ΔP and J increase continuously with Re number, as expected. The case 'D' offers a slightly higher pumping power ratio compared to the reference case 'B'. The increase in pressure drop is due to the complex interaction between the SES and vortices, as δ_P decreases. The result indicates that when $\delta_p = 0.6$

mm, an improved heat transfer performance is exhibited by case ‘D’ and it has been chosen for further optimization studies.

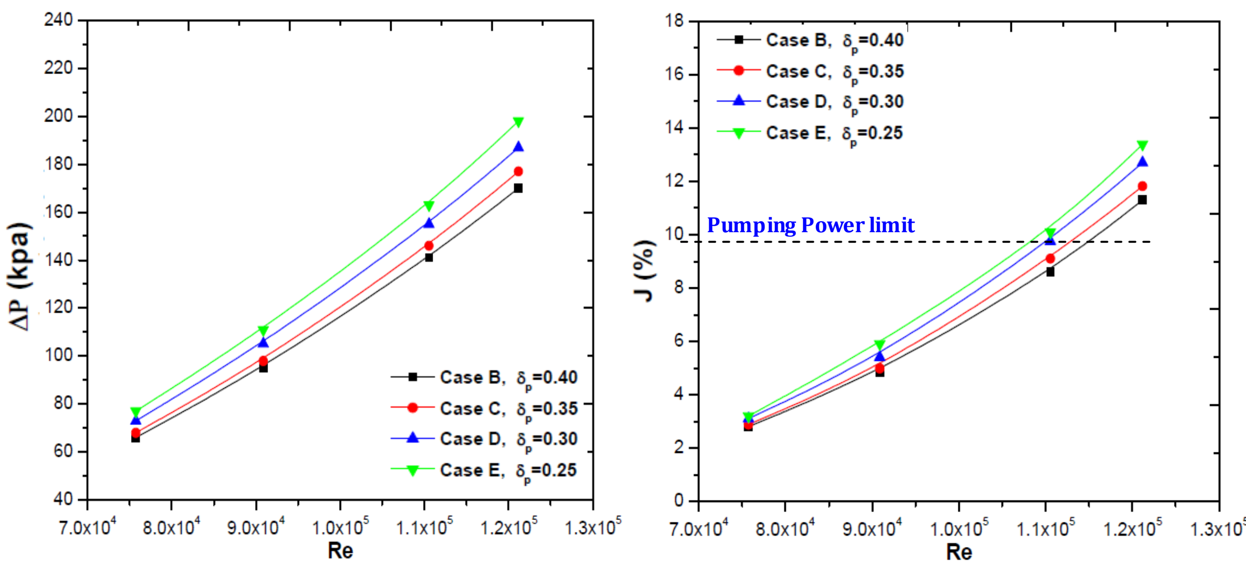

(a) (b)

Fig. 5.7. Comparison of (a) pressure drop, and (b) pumping power ratio against Re with various δ_p.

5.3.1.1. Discussion on Heat Transfer at Various SES Relative Pitch

Figure 5.8 demonstrates the comparison of the turbulent kinetic energy (TKE) normalized by the bulk mean velocity squared, at a distance of 1.5 mm away from the target surface at Re = 1.10×10^5. It can be observed that as the relative pitch decreases, the turbulence level in the mainstream flow region increases, and maximum turbulent mixing level appears in the center around the vicinity of SES.

Also, the eddies formed at the back of the last row of SES, due to increase in space between the last row of SES and thimble are shown Fig. 5.8. These vortices also help in enhancing the heat transfer coefficient in case ‘D’, as compared to case ‘B’. From the above discussion, it is clear that the thermal performance of divertor finger mock-up with SES increases with a decrease in the relative pitch, at the cost of higher pressure drop.

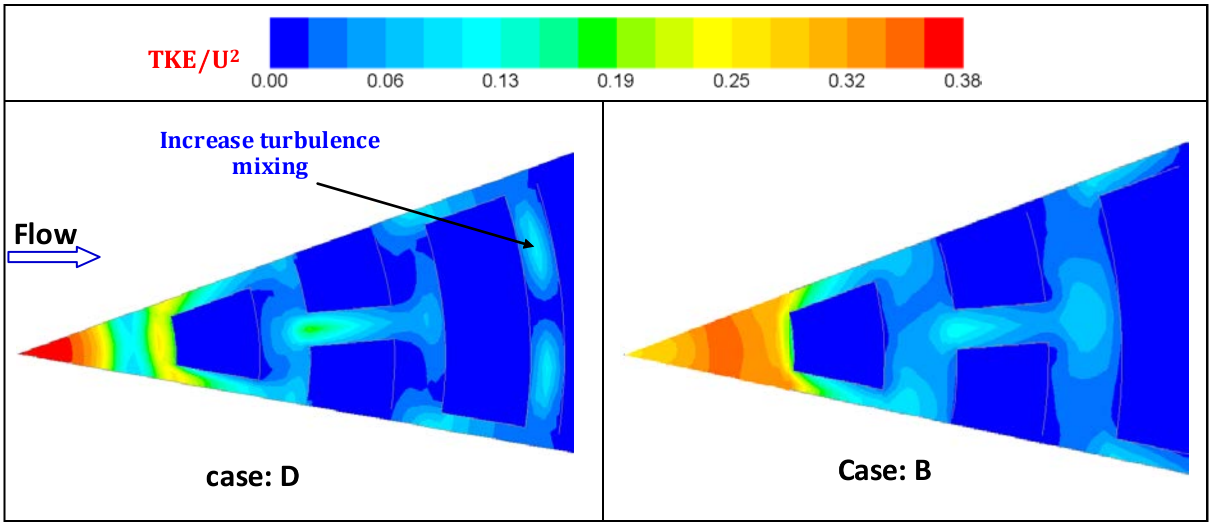

Fig. 5.8. Comparison of turbulence kinetic energy distribution around SES for reference case 'B' and optimized cases 'D' at Re = 1.10×10^5.

5.3.2. Comparison of Finger Mock-Up at Different SES Relative Thickness

The effects of relative thickness (δ_t) on the temperature and pressure drop in divertor finger mock-up with SES are shown in Figs. 5.9 and 5.10. Other geometric parameters viz., p = 0.6 mm, h = 2 mm and β = 30° are kept constant in the various cases studied. Figures 5.9(a) and (b) exhibit the effect of δ_t on the tile and thimble temperature. It can be seen that the temperature readily decreases when the thickness of SES increases for all the values of Re number. This is due to effective heat transfer caused by increasing the surface area exposed to the fluid medium.

Due to space limitation, it is not possible to increase the δ_t above 0.57 mm. Further reduction in temperatures of tile and thimble has been examined by adding another row of extended surface by decreasing δ_t as shown in Fig. 5.5. One can notice that with the reduction in thickness, thermal performance of finger mock-up with SES becomes worse. Compared to cases 'B' and 'D', decrease in thimble temperature achieved in case 'F' is ~27.5°C and ~8°C, respectively at identical prototypical Reynolds number (Re = 1.10 × 10^5).

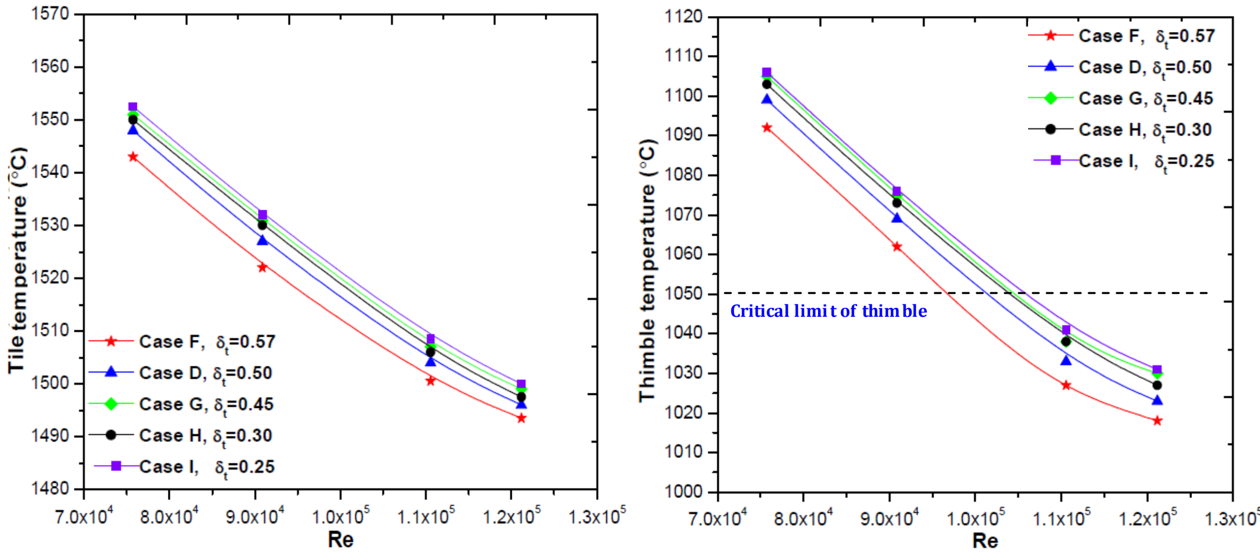

(a) (b)

Fig. 5.9. Comparison of (a) tile and (b) thimble temperature versus Re with various δ_t.

Figures 5.10(a) and (b) illustrate the dependence of pressure drop and pumping power ratio on Re number for various values of SES thickness. From Fig. 5.10(a), it is observed that the pressure drop in divertor finger mock-up decreases as SES thickness increase, because the momentum of coolant reduces by an increase in surface area. As a consequence a lower pumping power needed to remove the heat loads from finger mock-up. The maximum difference observed in ΔP values of case 'F' and case 'B' is ~5.2 kPa. Similarly the difference observed in ΔP values of case 'F' and case 'D' is ~10 kPa at same prototypical Re.

It should be noticed that when the δ_t is decreasing, the ΔP and J of finger mock-up with SES increase significantly. The reason is that adding another row of SES, also offers resistance to the flow of helium through finger mock-up. Further, cases 'D' and 'F' both have been considered for further optimization studies to find the effect of h/D on the heat transfer performance.

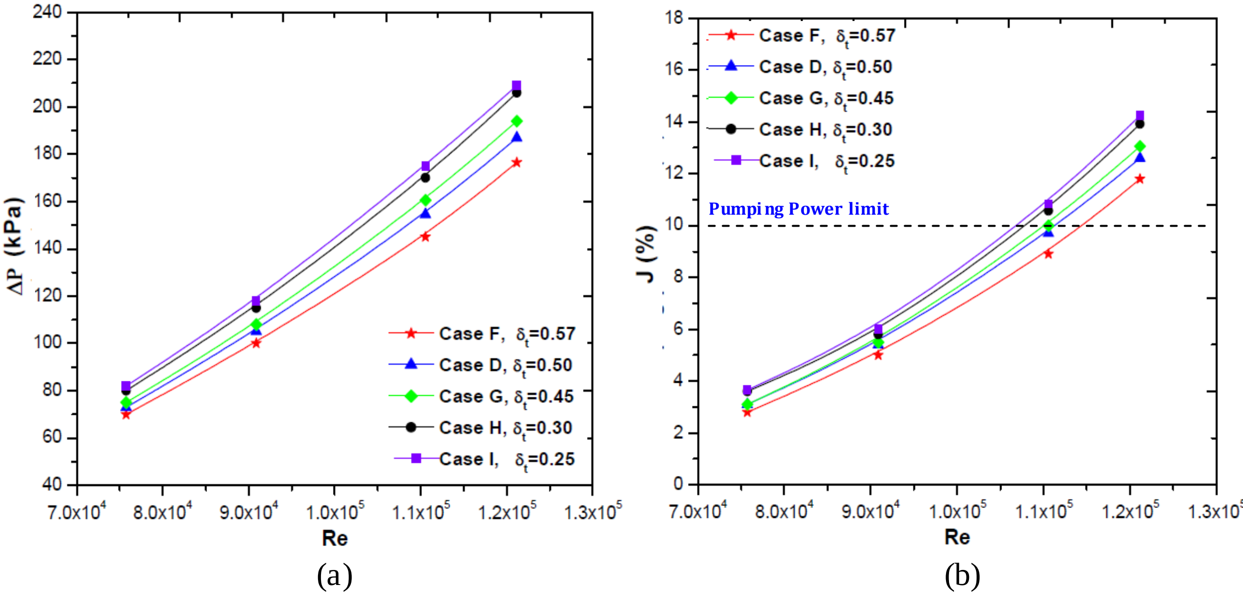

Fig. 5.10. Dependence of (a) pressure drop and (b) pumping power ratio verses Re for various δ_t.

5.3.2.1. Discussion on Heat Transfer at Various SES Relative Thickness

The temperature distributions of thimble in the finger mock-up with SES, as predicted by the computational model are depicted in Fig. 5.11 for Re = 1.10×10^5. It is seen that for identical Re, cases 'D' and 'F' leads to reduced thimble temperature compared to the reference case 'B'. It is due to the improvement in the heat transfer rate by an increase in surface area and turbulence.

It can be noticed that, the surface temperature of the thimble at the center location has a lower average temperature and increases in the radial direction. The rapid decrease in temperature at the center is due to direct impingement of a high velocity jet, and lower average temperature of coolant at the front row of SES. This leads to high heat dissipation in divertor finger mock-up with SES, as seen in Fig. 5.3.

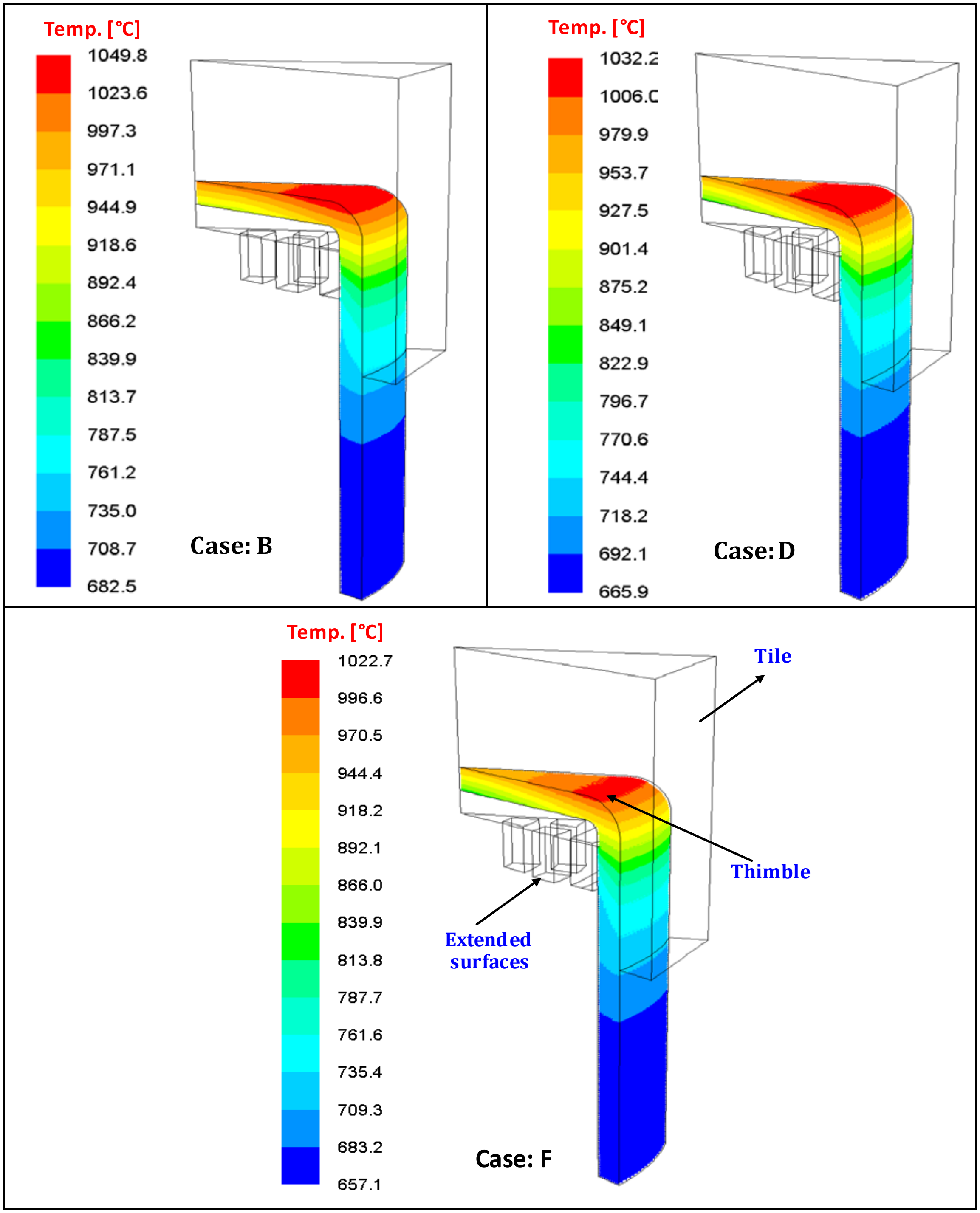

Fig. 5.11. Comparison of thimble temperature distributions in the finger mock-up with SES at Re = 1.10×10^5.

5.3.3. Comparison of Finger Mock-Up at Different h/D Ratio

Figure 5.12(a) and (b) presents the variations of tile and thimble temperature with various heights to jet diameter ratio for the case 'D', keeping δ_p, δ_t and β° as constant. It can be observed that temperature is low when the h/D ratio is small, because wall heat transfer coefficient increases with reduction in height of SES.

The value of the tile and thimble temperature is minimum for case 'J', where h/D = 0.75 and a further decrease in h/D produces only a small change in temperature. The maximum reduction in thimble temperature achieved in case 'J' is 30°C compared to case 'B' and 13°C compared to the case 'D' at same prototypical Re.

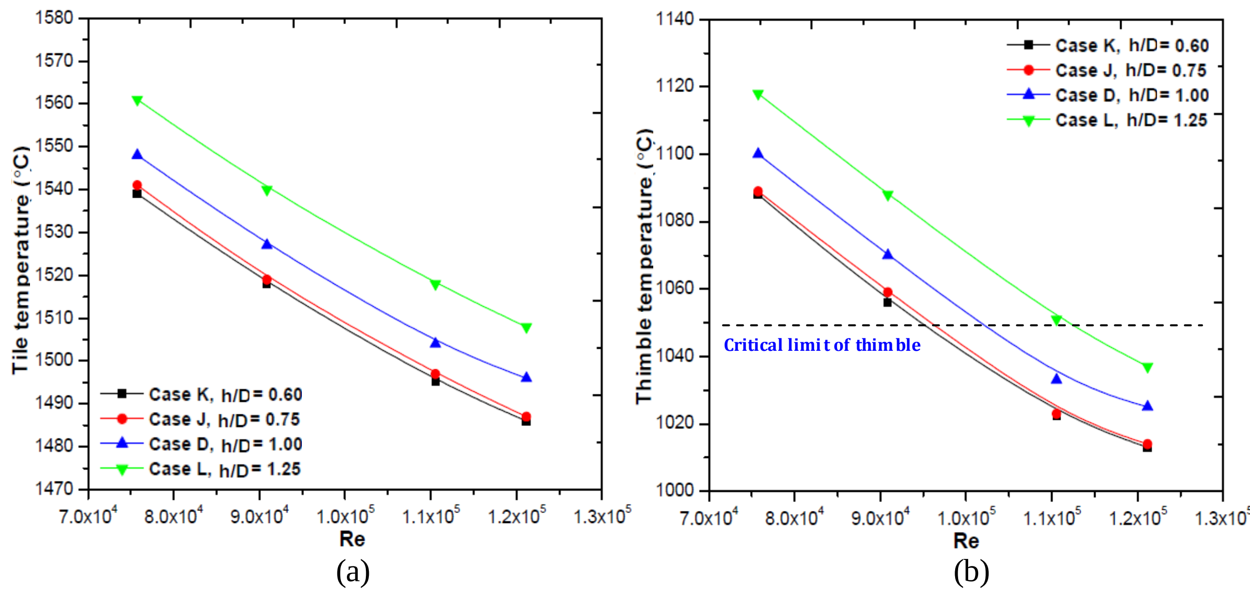

Fig. 5.12. Comparison of (a) tile, and (b) thimble temperature versus Re with various h/D ratios for case 'D'.

From Figs. 5.13(a) and (b), it can be seen that the pressure drop dramatically increases as the ratio h/D decreases. It shows that temperature of the tile and thimble are significantly lower, but the corresponding flow resistance is much higher than reference case. This is due to the strongly interruption of flow by SES. The increase in ΔP observed in case ‘J’ is 51 kPa, compared to case ‘D’ and the increase in the pumping power ratio is ~3.5% at equal prototypical Re.

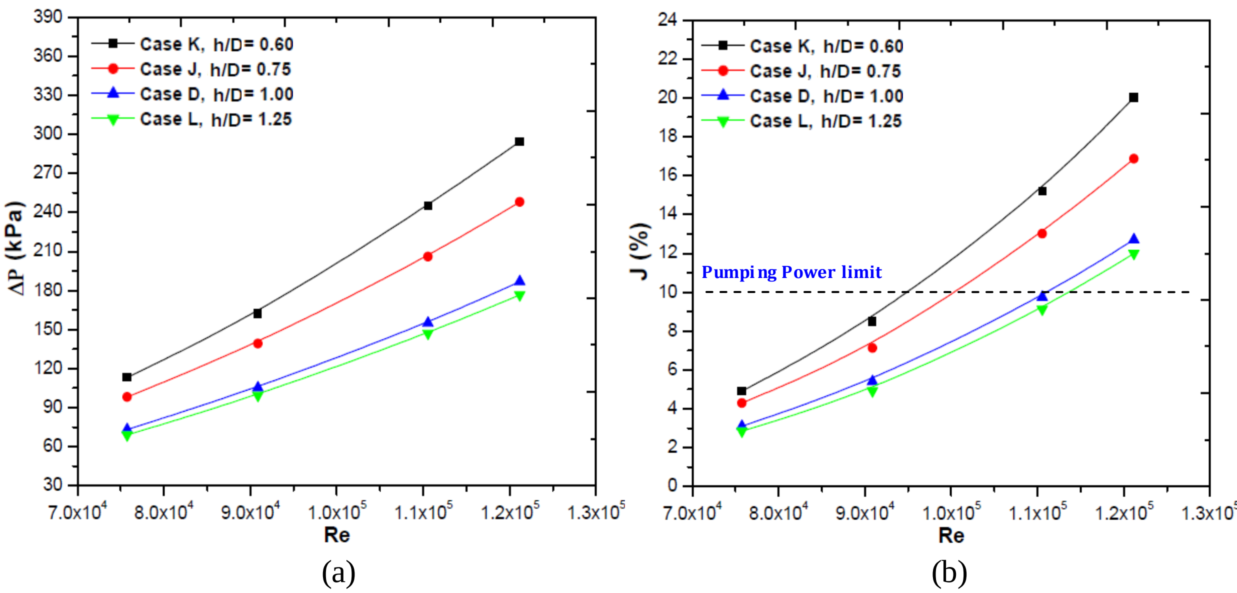

Fig. 5.13. Comparison of (a) pressure drop, and (b) pumping power ratio versus Re with various h/D ratios for case ‘D’.

The effects of h/D ratio on the temperature and pressure drop for the case ‘F’ are also shown in Figs. 5.14 and 5.15. A similar study was also performed for case ‘F’, and same phenomenon observed in studied cases. The temperature drop in thimble observed in case ‘M’ (h/D = 0.75) is 37°C and 13.5°C respectively, compared to cases ‘B’ and ‘F’ at Re. The increase in ΔP observed in case ‘M’ is 42 kPa compared to case ‘F’, and corresponding increase in pumping power ratio is ~3%.

From the above result, we find that h/D ratio has significant influence on the thermal-hydraulic performance of divertor finger mock-up. It is observed that, cases ‘J’ and ‘M’ appreciably reduce the thimble temperature at the cost of marginally higher pumping power ratio than the target value by ~3% and ~2.3%, respectively.

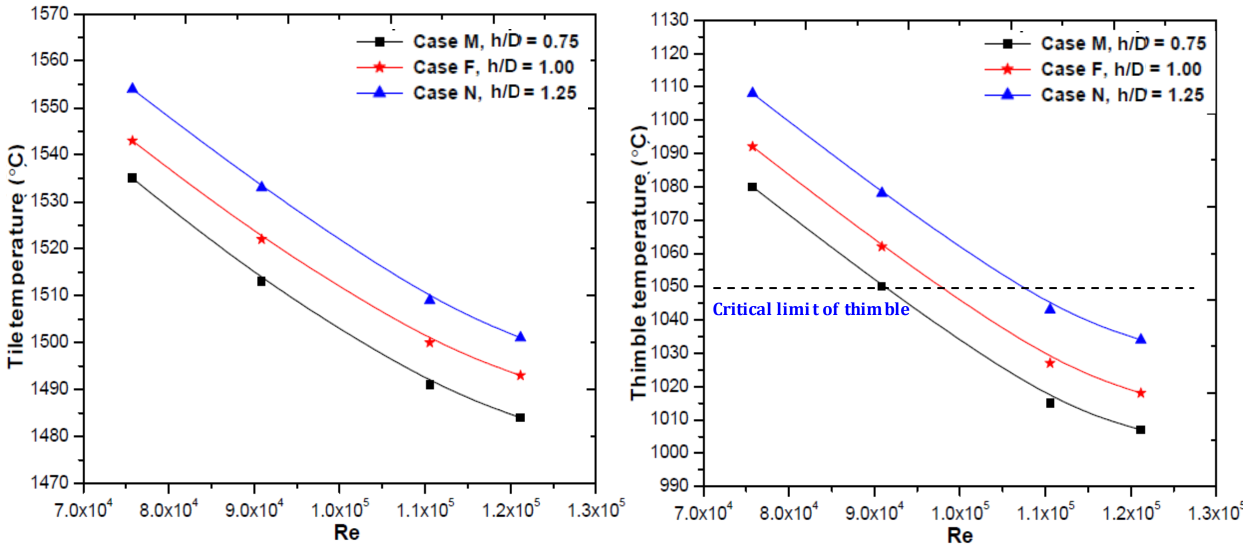

(a) (b)

Fig. 5.14. Comparison of (a) tile and (b) thimble temperature as a function of Re with various h/D ratios for case 'F'.

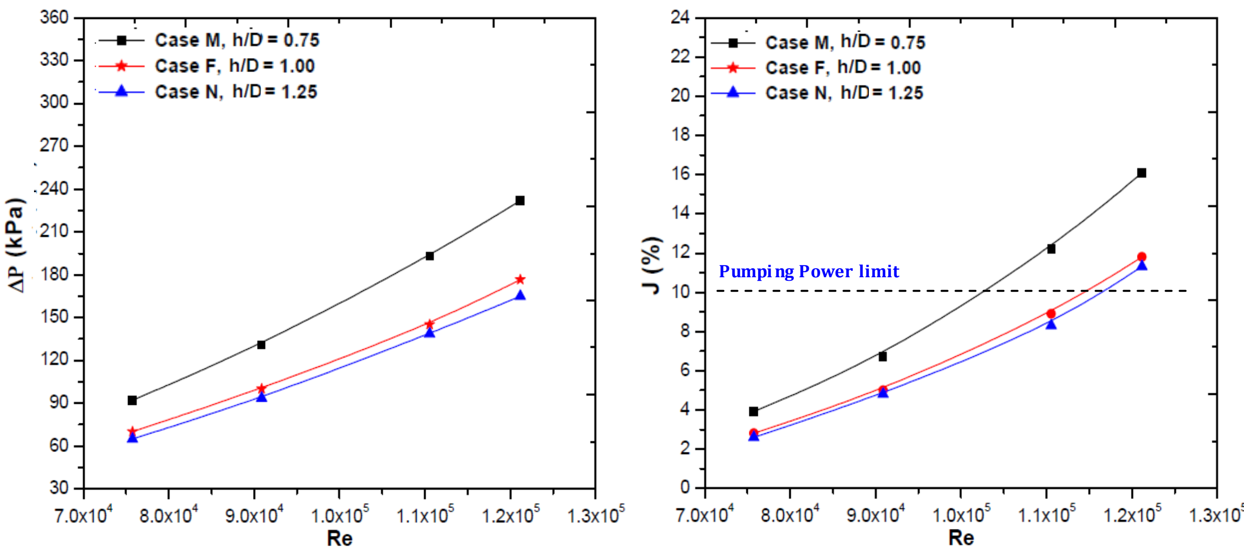

(a) (b)

Fig. 5.15. Comparison of (a) pressure drop, and (b) pumping power ratio as a function of Re with various h/D ratios for case 'F'.

5.3.3.1. Discussion on Heat Transfer at Various h/D Ratio

In order to develop further understanding into the influence of the h/D on the heat transfer mechanism in the divertor finger mock-up, a comparison of the contour plots of the wall heat transfer coefficient for cases 'J' (h/D = 0.75) and 'D' (h/D = 1) is depicted in Fig. 5.16. It can observe that the peak heat transfer coefficient occurs near the center of the jet in both of the cases, because the velocity of fluid is high at the center. It can be clearly seen that, heat transfer coefficient is high in case of 'J' compared to the case 'D'. The reason is that, high velocity jet impinges directly on the target surface without losing its momentum to the surrounding flow, leading to the associated increase in heat transfer coefficient.

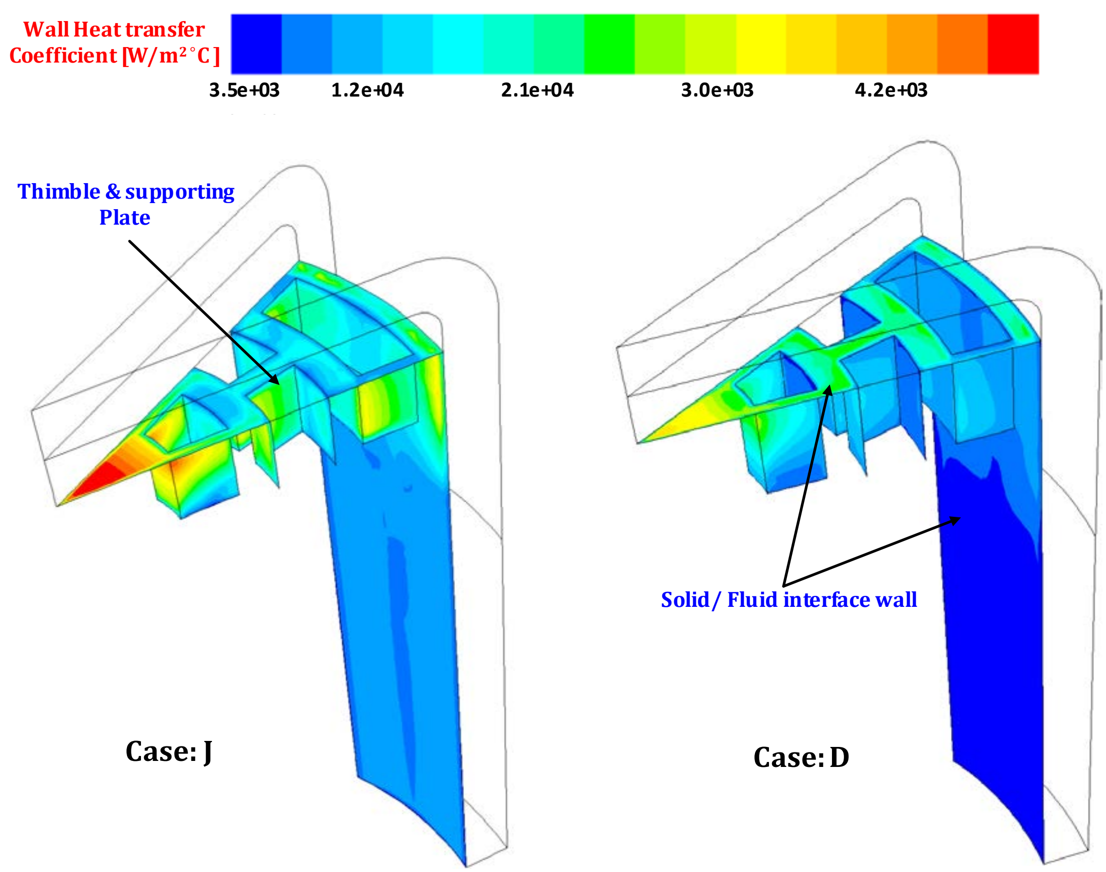

Fig. 5.16. Comparison of the wall heat transfer coefficient contour plots at Re = 1.10×10^5.

5.3.4. Comparison of Finger Mock-Up at Different Jet Diameter

The sensitivity analysis of jet diameter on thermal performance of finger mock-ups has been performed for prototypical Re = 1.10×10^5. The outcome of the analysis is presented in Table 5.2. As shown in Table 5.2 a reduction in jet diameter of finger mock-ups experiences an increment in temperature and pressure drop, which deteriorate the heat transfer performance. Further studies for the case 'F' have not been performed as already a reduction in the thermal performance has been observed in the former case.

Table 5.2: Results of different jet diameter on thermal performance of divertor at Re = 1.1×10^5.

Case	Unit	P	O	D
Jet diameter	mm	1.5	1.7	2
Maximum tile temperature	˚C	1545.6	1522.8	1504.2
Maximum thimble temperature	˚C	1075.1	1049.5	1032.2
Pressure drop (Δp)	kPa	240.87	200.37	155.60
Relative pumping power ratio (J)	%	14.93	12.42	9.4

5.3.5. Comparison of Finger Mock-Up at Various Circumferential Positions of SES

The effect of circumferential position of SES on thermo hydraulic performance of finger mock-up has been studied for various configurations. From Fig. 5.17, it can be seen that when circumferential positions varied, the corresponding number of SES is also varied. The circumferential positions of SES (β = 30˚) are same for all cases discussed in the above section. The main objective of this study is to assess the heat transfer capability by varying the circumferential position (15˚and 20˚), and find the effect of increase in SES.

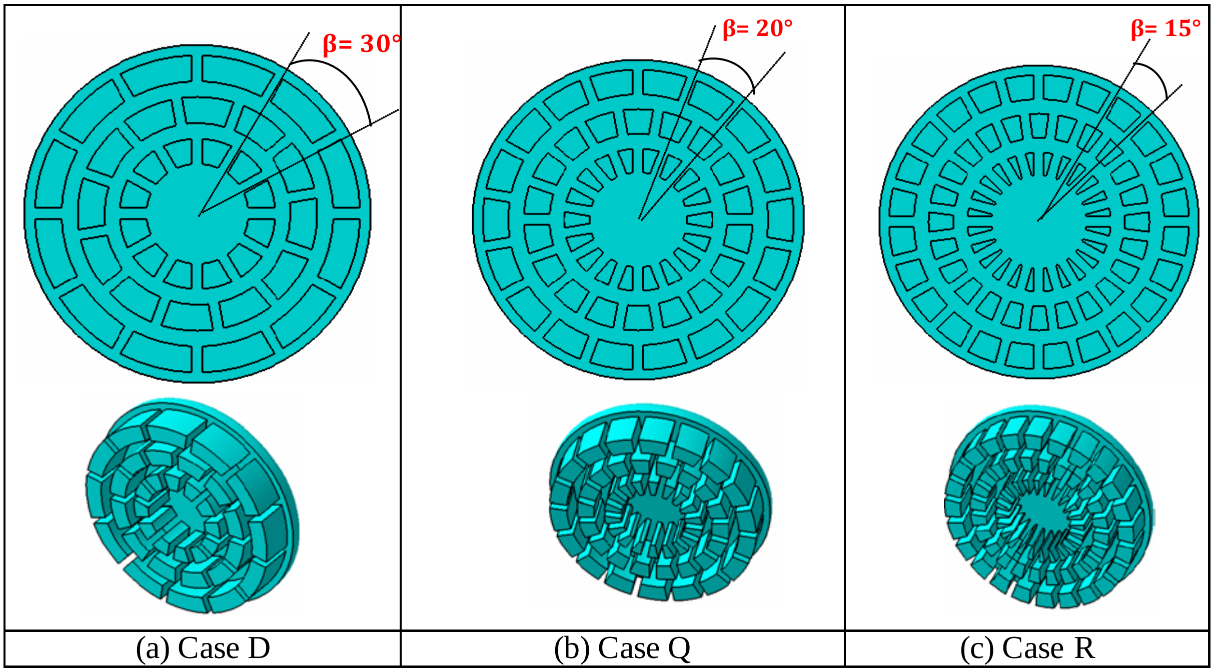

Fig. 5.17. Plan and 3D views of different configuration of SES (a) 30º, (b) 20º and (c) 15º.

Temperature and pressure drop values for the case 'D', 'Q' and 'R' are presented in Table 5.3. From the Table 5.3 it can be noticed that, thermal performance of finger mock-up with SES decreases significantly, when β˚ decreases. This is presumably due to a reduction in the surface area of SES. It indicates that the heat transfer is counterproductive towards the increase in the SES. Similar observations have been noticed for case F also.

Table 5.3: Results of circumferential positions of SES on performance of divertor at Re = 1.1×10^{5}.

Case	Unit	R	Q	D
Circumferential position of SES (β)	-	15°	20°	30°
Number of SES		72	54	36
Maximum tile temperature	˚C	1532.7	1525.2	1504.2
Maximum thimble temperature	˚C	1061.3	1052.9	1032.2
Pressure drop (Δp)	kPa	173.72	169.46	155.60
Relative pumping power ratio (J)	%	10.99	10.5	9.4

5.4. STRUCTURAL ANALYSIS

A combined CFD and structural analysis have been carried out to evaluate the stresses induced in the system due to high pressure (10 MPa) and large heat flux (10 MW/m^2) for various optimized designs of divertor finger mock-up using ANSYS Workbench 14.0. To determine the stress distributions, the pressure and temperature distributions obtained from the CFD optimization studies are imported to the finite element tool. Temperature dependant properties are considered for tungsten (W) and tungsten lanthanum oxide (WL-10). To prevent the movement in the vertical direction, constraints are applied to the thimble bottom surface. Figure 5.18 illustrates the Von-Mises stress distribution for optimized geometries. The peak stresses occur at the tile-thimble interface in all the cases. For all the optimized designs, von-Mises stresses are within allowable limits of 378 MPa [78], and the variation in the maximum peak stress is insignificant (< 1.4 %).

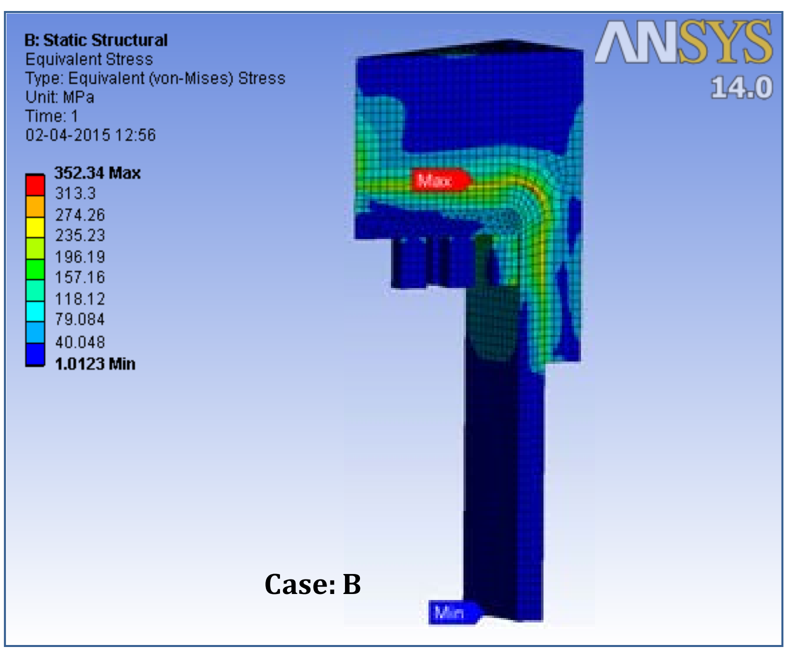

(a)

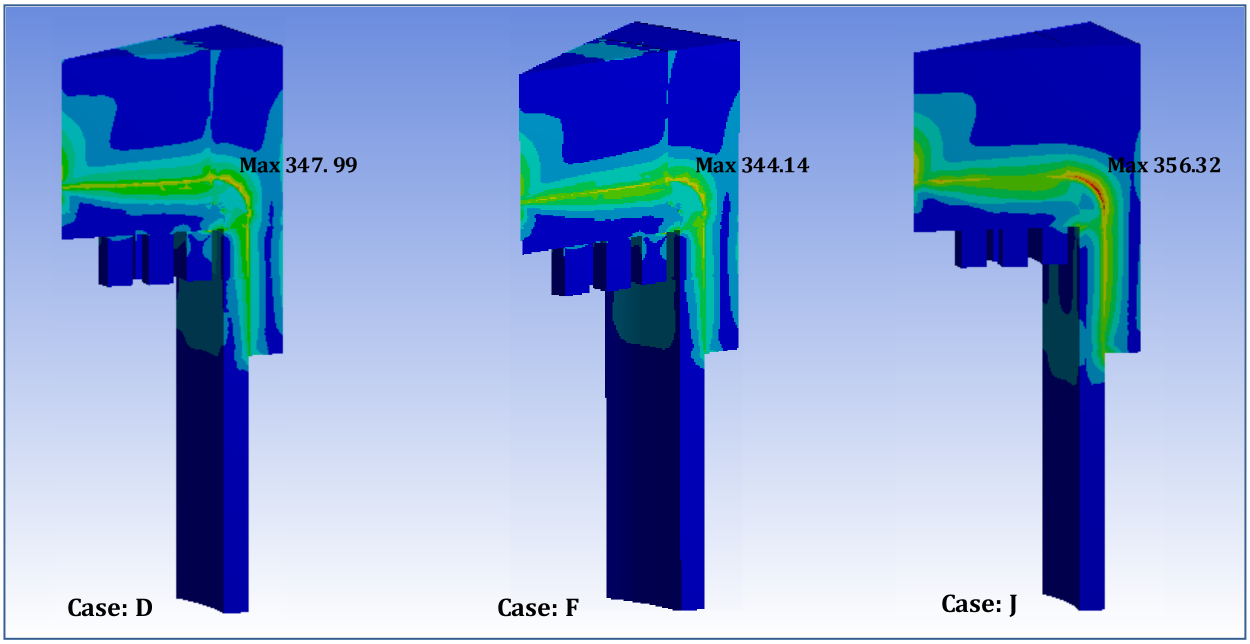

(b)

Fig. 5.18. Von-Mises stress distribution for (a) reference case and (b) various optimized design variants.

5.5. CLOSURE

Detailed parametric studies have been carried out towards geometrical optimization of divertor finger mock-up with SES. For this purpose, 3-dimensional conduction in the solid walls and convection in high pressure helium jet have been solved as a conjugate problem. The computational model has been validated against in-house experiments carried out in a new heat concentrator with air as the simulant. The non dimensional geometric parameters considered for the optimization are SES relative pitch (δ_p = p/h), thickness (δ_t = t/h), the ratio of SES height to jet diameter (h/D), the circumferential position of extended surface (β°), and jet diameter (D). The flow parameter varied is the jet Reynolds number. The following are the major conclusions of the parametric study:

- The tile and thimble temperatures decrease considerably whereas the pressure drop and the pumping power ratio increase significantly with an increase in flow Reynolds number.
- The thermal performance of finger mock-up with SES is significantly improved for the two optimum designs, having relative pitch and thickness of 0.30 (case 'D') and 0.56 (case 'F'), compared to the reference design (case 'B').
- The influence of h/D ratio on the performance of divertor finger mock-up heat sink is noticeable. It is observed that, in cases 'J' and 'M' (h/D = 0.75) the tile and thimble temperatures appreciably reduce with marginally higher pumping power ratio than the target value by ~3%.
- The effect of jet diameter and circumferential position of SES are found to be counterproductive towards the heat transfer performance.

A combined computational fluid dynamics and structural analysis approach are adopted to simulate the Von-Mises stress distribution in divertor finger mock-up heat sink. The results show that the deviation in peak stresses for various optimized geometries are within the design limits. The maximum stress deviation for the optimized design is ~ 1.4%.

CHAPTER 6

COMPUTATIONAL FLUID DYNAMIC STUDIES ON NEW CONCEPT FOR HELIUM COOLED DIVERTOR

6.0. INTRODUCTION

Development of an efficient divertor concept is an important task to meet in the scenario of the fusion power plant. Present chapter deals with, *"divertor heat sink concept cooled by helium for the fusion tokamak"*. The first wall of the divertor made-up of several modules has to overcome the stresses caused by high heat flux, in the present design. Thermal hydraulic performance of one such divertor heat sink module is numerically investigated using the Volume Fluent software.

The effects of critical thermal hydraulic and geometric parameters on the heat transfer characteristics are presented as a function of Reynolds number. The 3-dimensional thermal hydraulic investigations include thimble diameter (D_T), nozzle diameter (D_N), the ratio of "nozzle to wall space" to "nozzle diameter" (H/D_N) and nozzle shapes etc. as parameters. Elliptical nozzles at specific orientation are found to perform better than other nozzles for identical Reynolds number. The performances of triangular nozzles are found to be poorer than other nozzles. Similarly, a minimum thimble temperature and pressure drop in the circuit is achieved at H/D_N ~1.66. The proposed design is found to have a margin of 10 % i.e., capable of handling 11 MW/m^2 against target heat flux values of 10 MW/m^2.

The stresses induced in the divertor heat sink by the thermal and pressure loads are an important factors that limit the life of the divertor. Therefore, structural analysis of the divertor heat sink assembly has been carried out and the stress values arising out of temperature gradient and pressure are found to be within acceptable limits, demanding the reliability of the proposed concept.

6.1. DESCRIPTION OF DIVERTOR HEAT SINK CONCEPT

A schematic diagram of the proposed divertor heat sink for fusion reactor application is shown in Fig. 6.1. A divertor is toroidal divided into a number of cassettes, for easier handling and maintenance. A modular design has been developed to reduce thermal stresses, which allows a higher heat flux to be accommodated. The plasma-facing component is exposed to plasma particle and neutron that lead to physical and chemical sputtering of the target surface. Tungsten (W) is the most promising divertor material, because it has excellent thermo-physical properties.

As illustrated in Fig. 6.1, plasma-facing wall of divertor is made up of tungsten with sacrificial thickness (4 mm) as the thermal shield. The thermal shield is not cooled directly, to avoid the probability of crack formation in design. Thermal shield is brazed on the thimble made of tungsten alloy (WL-10). A high melting temperature filler material Pd-Ni 40 (1511K) has been considered as the brazing filler between the mating surfaces [84-87]. A steel jet cartridge carrying the multiple nozzles is placed concentrically inside the thimble for efficient heat transfer. The coolant fluid (He) enters through the inlet manifolds to the cartridge, and accelerates through the multiple nozzles (D_N = 0.7 mm). The helium jet impinges upon and cools the heated surface, then flows down along the space (H= 1 mm) between the inner cartridge to the outlet manifold as shown in Fig. 6.1.

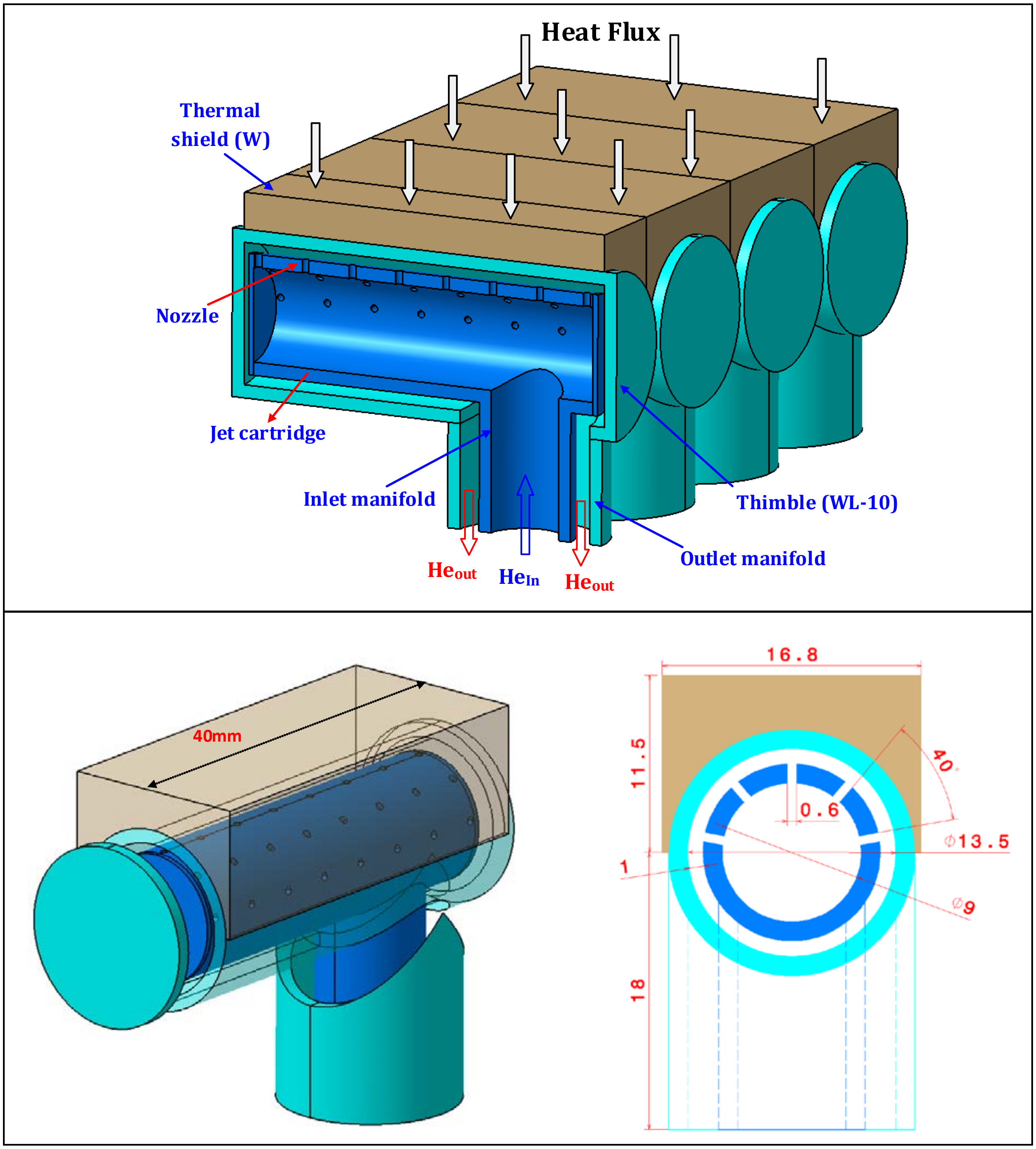

Fig. 6.1. Schematic diagram of divertor heat sink and detailed view (All dimensions in mm).

6.1.1. General Design Constraint

The total allowable heat flux limit for the helium cooled divertor heat sink is determined by the maximum temperature of the thimble, the pumping power of the helium coolant, and the combined mechanical and thermal stresses. The main design constraint is maximum thimble temperature, which is limited by ductile-to-brittle transition temperature (~600 °C) and recrystallization temperature (~1300 °C) of the W-alloy [76]. The most critical parameter in the present design is peak thimble temperature, which must be lower than the filler material melting temperature (1511 K) to enhance the life of the divertor and safe operation. Next limit is the necessary power to pump the helium through the divertor structure, which is targeted to be less than 10% of the total incident power removed from the structure. The third limit is total stresses (mechanical and thermal loads), which should be lower than the allowable stress limit at the corresponding temperature.

6.2. THEORETICAL FORMULATION AND NUMERICAL MODEL

6.2.1. Governing Equations and Numerical Method

In order to reduce the computational effort, only half of the section has been modeled in the present simulation. The fluid inside the divertor heat sink structure is modeled as an ideal gas under steady flow. Realizable k- ε turbulence model [88, 89] has been adopted to account for turbulent heat transfer and fluid flow. A second order upwind calculation scheme is used to reduce the numerical errors. The SIMPLE algorithm is used to resolve coupling between pressure and velocity in the computations. The convergence criteria for the momentum and continuity equations are set to a value below 10^{-4}, whereas for energy equation it is set to below 10^{-7}.

6.2.2. CFD Mesh and Boundary Condition

Figure 6.2 shows an isometric view of the CFD mesh for the divertor heat sink model. The commercial software GAMBIT is used to create the structured grid for the computational model.

For accurate resolution of heat transfer phenomenon near the fluid-solid interface walls, a boundary layer mesh is adopted as can be seen in Fig. 6.2. Temperature dependent material properties have been considered for the solid domains. Helium (He) is specified as an ideal gas. A constant heat flux of 10 MW/m^2 is prescribed on the top surface wall, while the remaining walls are assumed to be adiabatic. No-slip conditions are applied at all of the walls. Uniform mass flow rate, temperature and pressure (600 ˚C and 10 MPa) are assigned at the inlet, whereas, outlet pressure condition is chosen at the outlet.

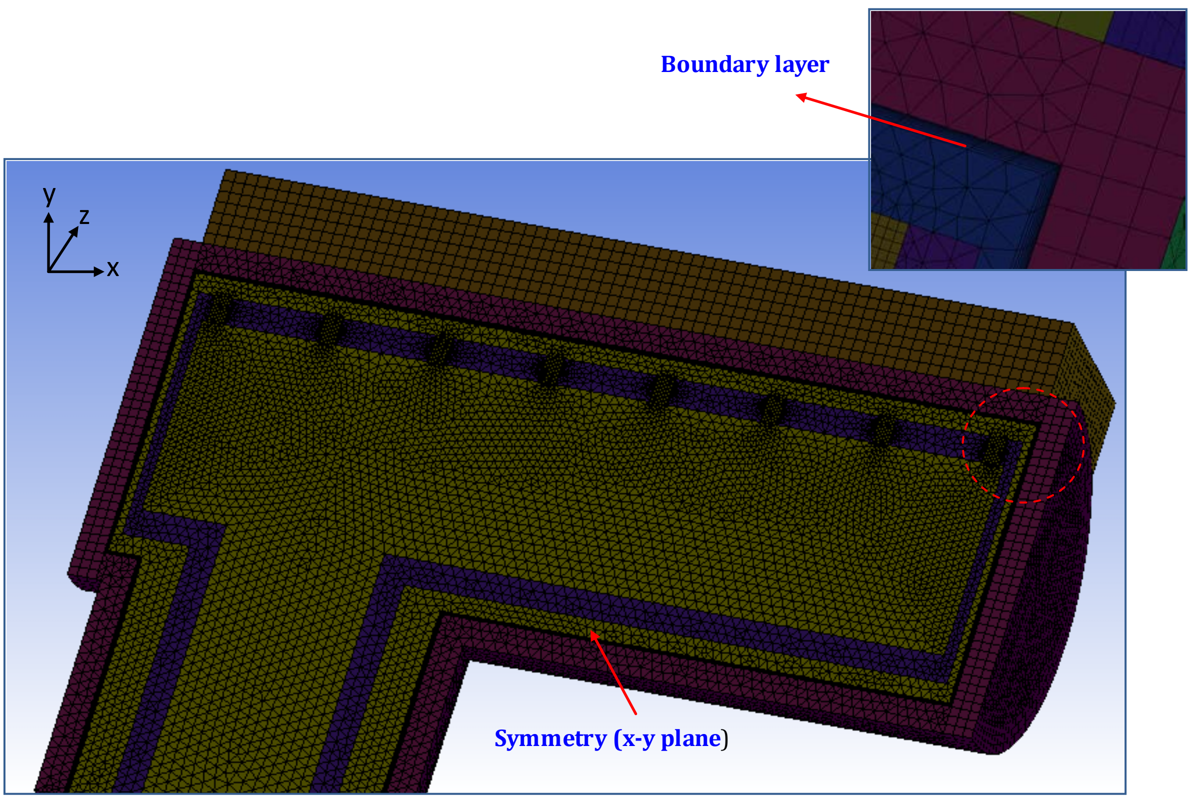

Fig. 6.2. CFD mesh for divertor heat sink model.

6.2.3. Grid Independence Analysis

In order to get a grid independent solution, careful grid independence check has been carried out with several grid systems. The number of grid cells considered, ranging from 2.75×10^5 to 7.42×10^5, as shown in Table 6.1. The maximum thimble temperature is selected as the target parameter for grid optimization, as it is an important design constraint. The result revealed that the computed results based on 6.5×10^5 cells are insensitive to further grid refinement, and thus employed for all models in the present study.

Table 6.1: Comparison of the maximum thimble temperature for different grid pattern at Re = 1.58×10^4.

Grid	Number of cells	Predicted maximum thimble temperature (K)	Percentage difference in temperature
Very coarse	275,000	1520	
Coarse	384,240	1503	-1.118%
Intermediate	508,638	1496	-0.465%
Fine	650,000	1493	-0.200%
Very fine	742,800	1493	0.000%

6.2.4. Parameter Definitions

The thermal hydraulic performance of proposed design has been evaluated by considering various parameters such as pressure drop (ΔP), pumping power (W) and pumping power ratio (J). Details of the thermal parameters are given in the Section 5.1.2.

6.3. RESULTS AND DISCUSSION

6.3.1. Thermal-hydraulic Performance Analysis

Three-dimensional simulations are performed to investigate the heat transfer and fluid flow characteristics in divertor heat sink. The objective of this study is to find the optimum cooling approach for divertor heat sink module. In addition, thimble diameter (D_T) has been varied to find the optimum diameter. Five inlet mass flow rates (m) of 10, 13, 15, 20 and 25 g/s, corresponding to the Re numbers of 1.2×10^4, 1.5×10^4, 1.8×10^4, 2.4×10^4 and 3.0×10^4, respectively are adopted to analyze the thermal hydraulic performance of divertor heat sink as shown in Figs. 6.3 and 6.4. Numerical studies are carried out at constant heat flux 10 MW/m^2.

Figure 6.3(a) and (b) presents a comparison of maximum temperature on the surface of thermal shield and thimble under a wide range of Re number. It can be observed that, when the thimble diameter increases, both the thermal shield and the thimble experience an increment in temperature at the same Re number. A possible explanation of the phenomenon above is that when thimble diameter is increased, the total heat loads to the structure increases. Therefore, higher mass flow rates are needed to maintain the thimble temperature limit. Thimble temperatures are well below the filler temperature constraint (1511 K) at Re number 1.58×10^4, 2.2×10^4 and 2.7×10^4, corresponding thimble diameters are 16, 20 and 25mm, respectively as seen in Fig. 6.3(b).

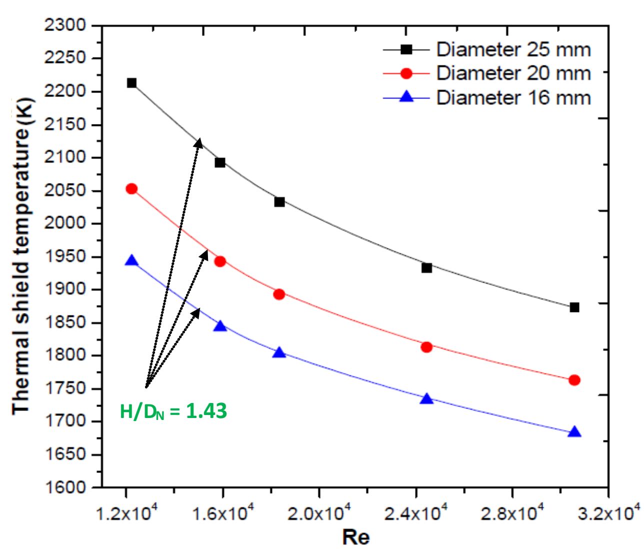

(a)

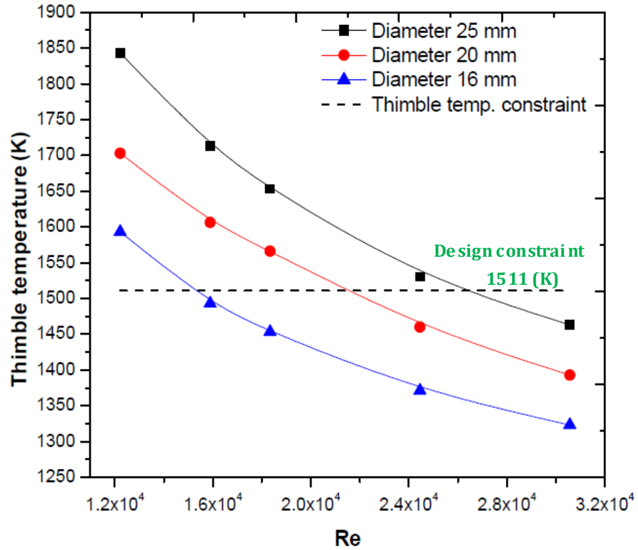

(b)

Fig. 6.3. Comparison of (a) thermal shield, and (b) thimble maximum temperature at various Re number.

Comparison of the pumping power ratios (J) with a different heat sink diameter is shown in Fig. 6.4. It is clear that with the increase in Re number, the pumping power ratios of heat sink increase as square of the Re. However, increasing the thimble diameter reduces the pumping power ratio. One notable fact is that the pressure drop decreases significantly in a larger diameter tube. This is due to the increase in diameter of the inlet manifold section and surface area of divertor heat sink, hence velocity of fluid decreases.

It may be noticed that the pumping power ratio is well within the design limit at Re number 1.58 x 10^4 for 16 mm diameter of the tube. About 60% and 140% higher pumping power ratio is required for 20 and 25 mm diameter tube to maintain the desired thimble temperature constraint. The results show that the performance of divertor heat sink reduces with increase in thimble diameter, and better thermal-hydraulic performance can achieved from the small diameter tube. Therefore, thimble with 16 mm diameter has been selected for further studies.

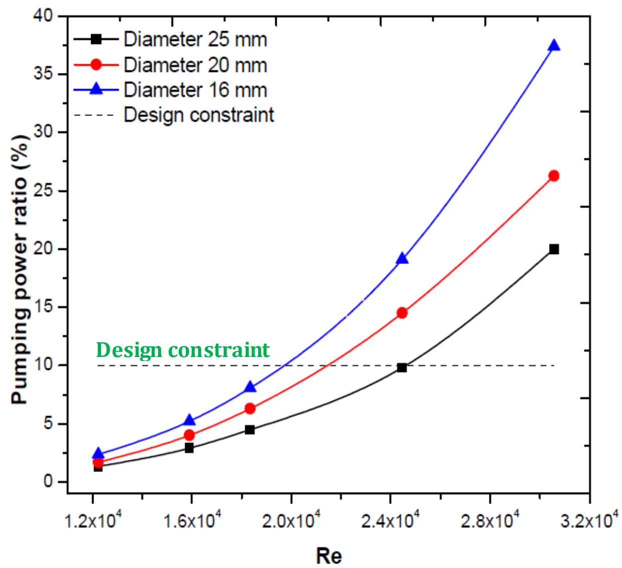

Fig. 6.4. Comparison of pumping power ratio as function of Re number at various thimble diameters.

To develop further understanding on the effect of thimble diameter on the heat transfer performance in the divertor heat sink, a comparison of temperature distribution at prototypical $Re_p = 1.58 \times 10^4$ is depicted in Fig. 6.5. It can be seen that, temperature of thermal shield and the thimble is higher for larger tube, and they decrease significantly with reduction in thimble diameter. This is due to enhanced heat load at the top of a larger diameter tube demanding higher amount of coolant to keep the thimble temperature within the design limit, and hence the high pumping power.

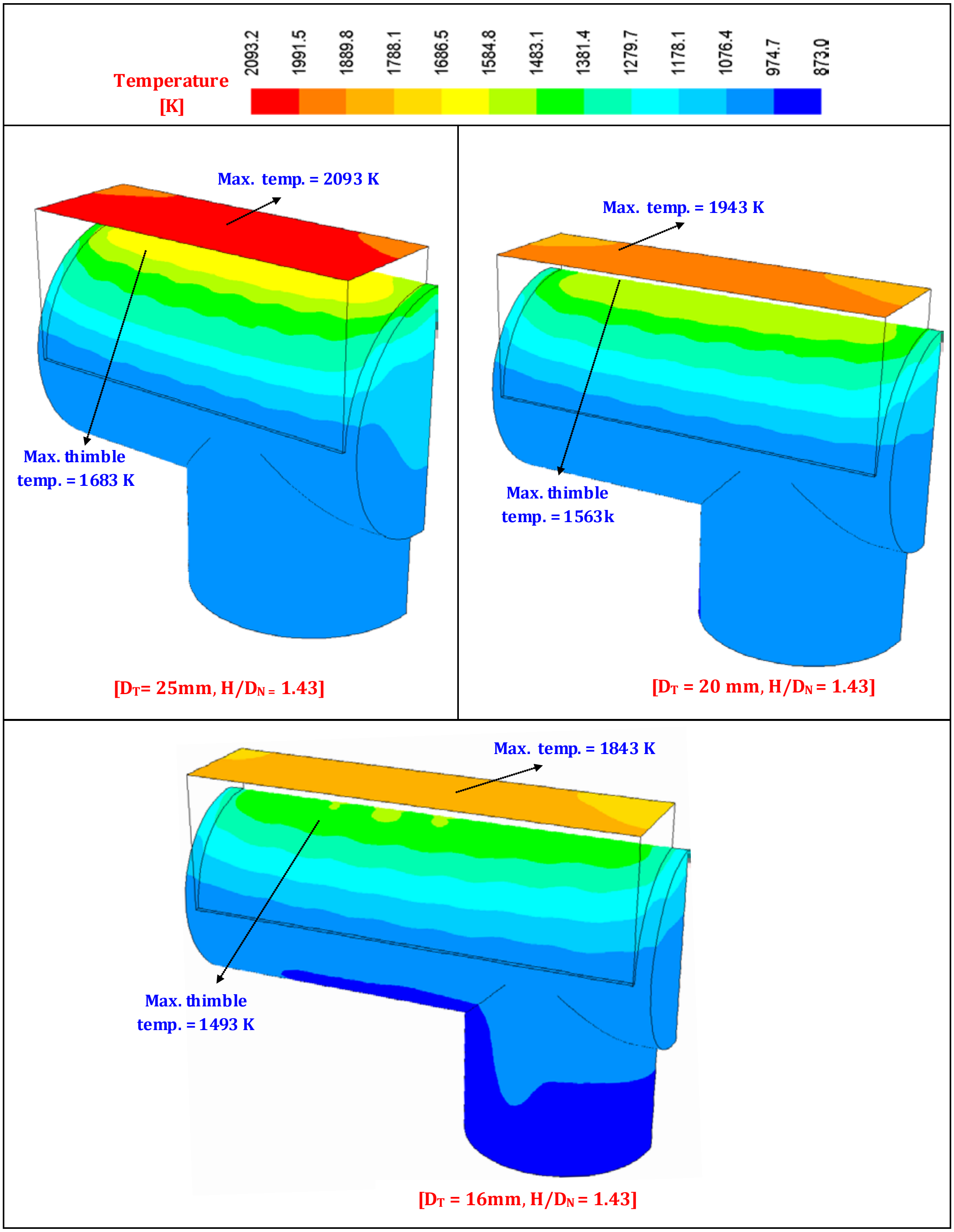

Fig. 6.5. Comparison of temperature distribution at various thimble diameter at $Re_p = 1.58 \times 10^4$.

6.3.2. Parametric Analysis

In Fig. 6.3(b), the thimble temperature is seen to be close to the temperature limit of filler material at a prototypical Re number. Therefore, an effort is made to reduce the thimble temperature as much as possible below the brazing filler-melting limit for enhanced life of divertor and safe operation. As discussed before, the Re number corresponding to the actual prototypical condition based on the mass flow rate 13 g/s for the DEMO is $Re_p = 1.58 \times 10^4$. Therefore, parametric analysis has been performed at the prototypical Reynolds number (Re_p).

6.3.2.1. The Effect of Nozzle Diameter (D_N) on Thermal-Hydraulic Performance

A comparison of performance of divertor heat sink as a function of nozzle diameter (D_N) is depicted in Fig. 6.6(a) and (b). The investigation has been carried out for five different nozzle diameters such as 0.7, 0.65, 0.6, 0.55 and 0.5 mm, while the nozzle-to-wall distance (H = 1 mm) and the number of nozzle holes are kept constant.

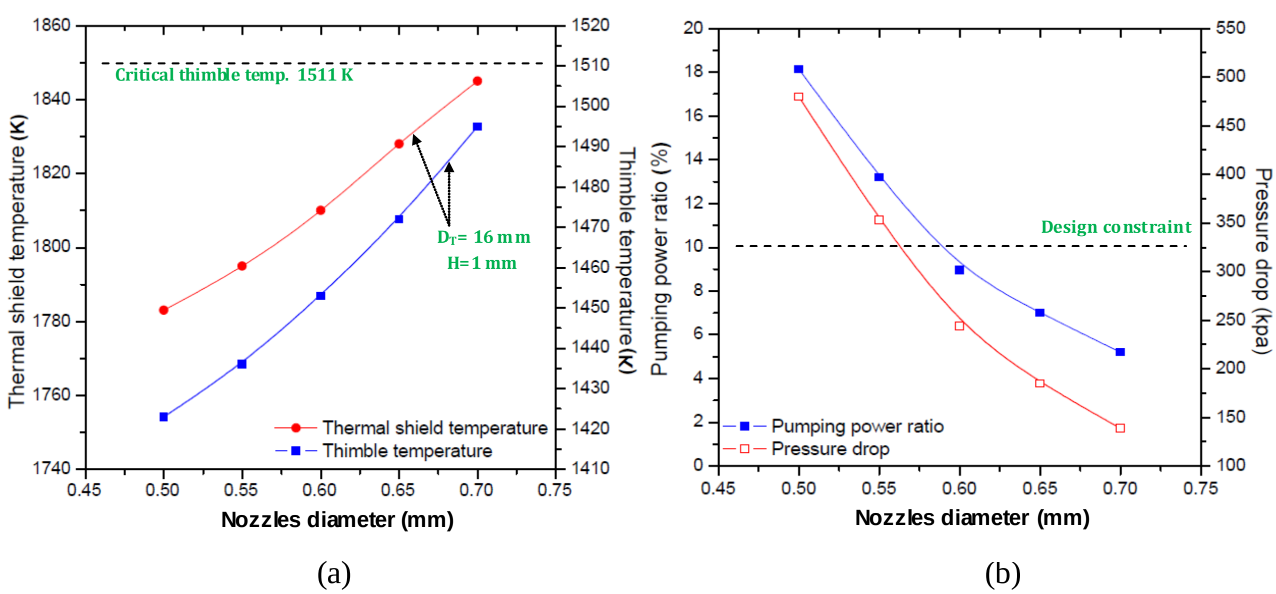

Fig. 6.6. Effect of different nozzle diameter on (a) maximum thermal shield and thimble temperature (b) pumping power ratio and pressure drop.

Figure 6.6(a) shows that a change in diameter of the nozzle holes has a stronger influence on the maximum thermal shield and thimble temperature. Temperature of divertor heat sink is decreasing with the decrease in nozzle diameter, because the velocity of impinging jets increases significantly, leading to the associated increase in heat transfer coefficient.

Figure 6.6(b) shows the pressure drop (ΔP) and pumping power (J) ratio as a function of nozzle diameter. It is seen that, ΔP and J extensively increase as the jet diameter decreases. The fluid velocity increases largely, which increase in the heat transfer rates. On the other hand, it causes a strong increase in pressure loss due to the direct relation between pressure loss and volume average velocity of the working fluid. It can be observed that, thimble temperature continuously decreases, but below the 0.6 mm nozzle diameter, pressure drop and pumping power ratio also increase largely. The above discussions reveal that 0.6 mm nozzle diameter reduces the thimble temperature substantially at the acceptable pumping power limit. Therefore, this diameter has been considered for further studies.

Figure 6.7 illustrates the comparison of velocity and temperature distributions predicted by CFD analysis for heat flux 10 MW/m^2 at Re_p. It can be clearly seen that, velocity is high at center of the nozzle and it continuously increases as nozzle diameter decreases. The nozzle with 0.5mm diameter has the smallest cross section of jets and consequently the highest nozzle velocity. Furthermore, it is clear that the temperature of the thimble is also reduced by an increase in the velocity of fluid.

The high velocity of jet causes higher turbulence in divertor heat sink, leading to an increase in heat transfer coefficient at the cost of higher-pressure drop. The contours of the local heat transfer coefficient (HTC) for different nozzle diameters are shown in Fig. 6.8. The heat transfer coefficient at the jet position is very high, since the local heat transfer coefficient is strongly influenced by jet velocity. The typical values of HTC are in the range of 10^4 W/m^2K.

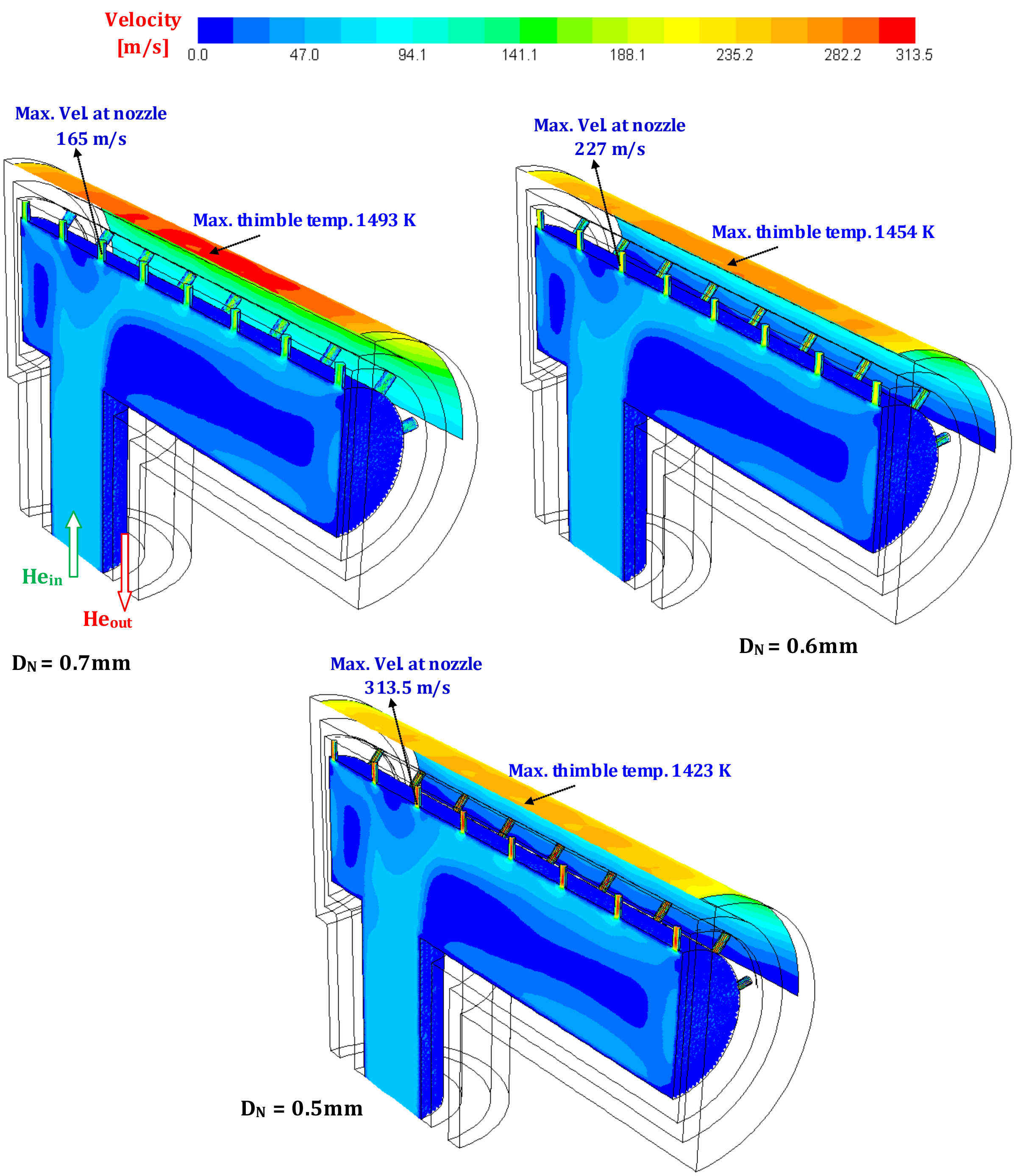

Fig. 6.7. Comparison of velocity and thimble temperature distributions in divertor heat sink for different nozzle diameters at Re_p= 1.58 x10^4.

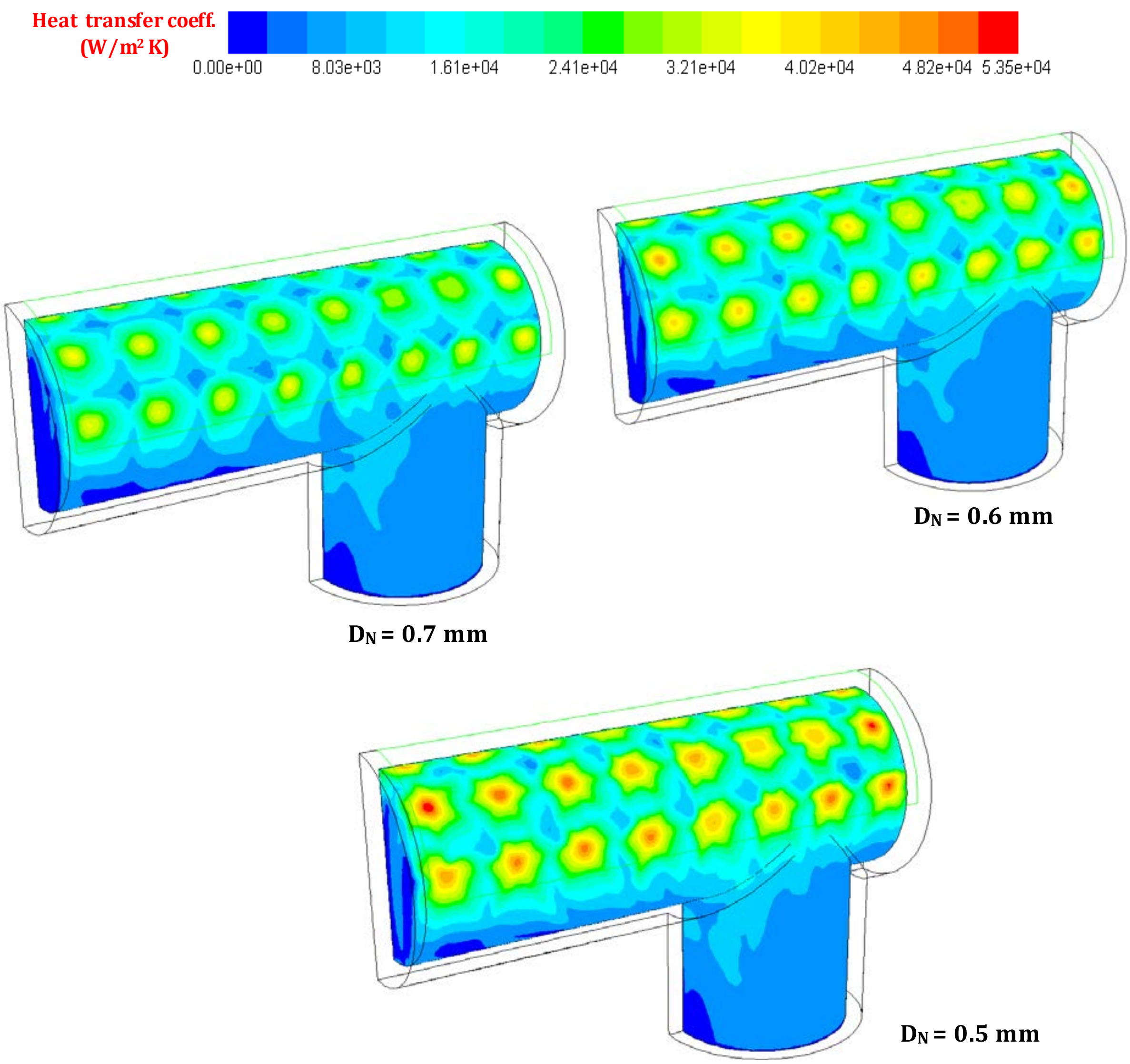

Fig. 6.8. Comparison of local heat transfer coefficient contour for various nozzle diameters.

6.3.2.2. The Effect of Nozzle to Wall Space (H) on Thermal-Hydraulic Performance

Figure 6.9(a) presents the variation of thermal shield and thimble temperature with different nozzle to wall space to nozzle diameter ratio (H/D_N), whereas the nozzle diameter (D_N = 0.6 mm) and the number of nozzle holes are kept constant. In this study, nozzle-to-wall space is varied as 0.7, 0.9, 1, and 1.2 mm. The corresponding H/D_N ratios are 1.33, 1.50, 1.66, and 1.83 mm, respectively. It can be observed that, divertor heat sink temperature increases as the nozzle to wall space increases. This is due to the reduction in momentum of jet velocity at the impingement location. As the space between nozzle to wall (H) increases, the effective heat transfer coefficient decreases. Furthermore, there is no significant difference found in results with a reduction in nozzle to wall space.

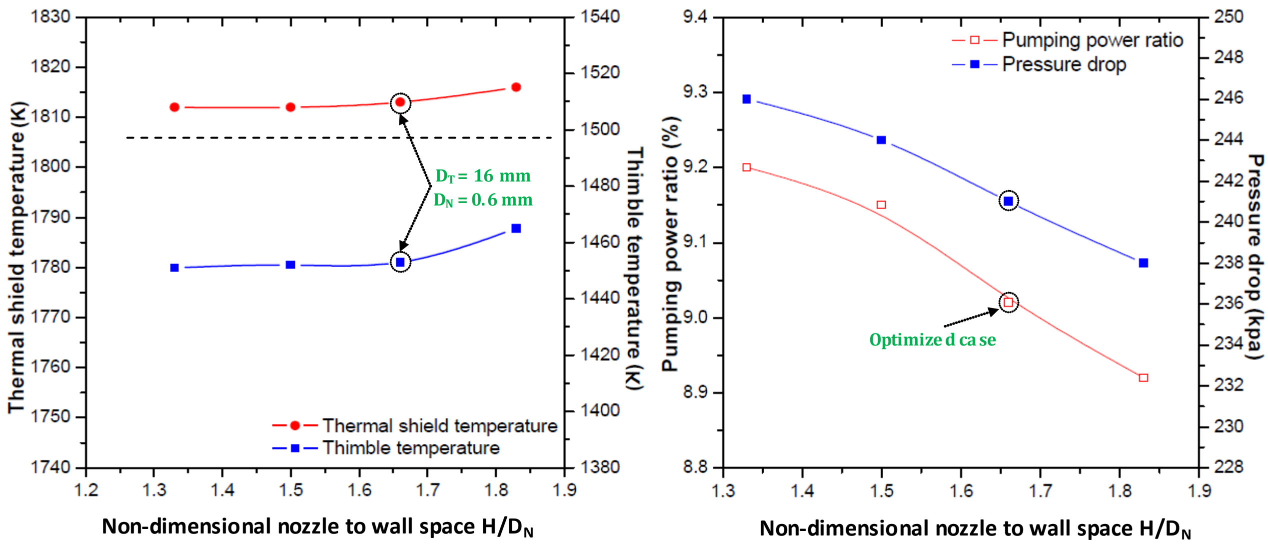

Fig. 6.9. (a) Comparison of maximum thermal shield and thimble temperature and (b) pumping power ratio and pressure drop at various H/D_N ratios.

Figure 6.9(b) illustrates the effect of different H/D_N ratios on pressure drop and pumping power ratio. The pumping power ratio decreases as H increases, due to the reduced velocity magnitude in the system. The results demonstrate that, jet to wall space does not significantly affect the thermal hydraulic performance of divertor heat sink. Therefore, nozzle to wall space H=1 mm for H/D_N =1. 66, is considered to be optimal.

From the all thermal-hydraulic and parametric studies, it is evident that divertor heat sink concept has potential to accommodate the design heat flux value of ~10 MW/m^2 at an acceptable pumping power limit. The optimized dimension of the thimble (D_T), nozzle diameter (D_N) and ratio of nozzle to wall space and nozzle diameter (H/D_N) are 16, 0.6, and 1.66 mm, respectively. To respect thimble temperature and pumping power limit, 13 g/s mass flow rate ($Re_p = 1.58 \times 10^4$) is adequate for the present divertor heat sink concept.

6.3.3. The Influence of Nozzle Shapes on Thermal-Hydraulic Performance

The influences of different nozzle shapes on heat transfer characteristics have been determined for the proposed divertor heat sink concept. For all the nozzle geometries, simulations have been performed for nozzle-to-wall distance of 1 mm for mass flow rates in the range of of 10-14 g/s. These mass flow rates correspond to Re number range of $1.2 \times 10^4 – 1.7 \times 10^4$ for circular jet. Five different nozzles, namely circular, elliptical, rectangular, square and triangular shapes of approximately equal cross section area are chosen for the present simulation. Details of the jet exit geometries are given in Table 6.2. Schematic of different nozzle shapes studied for divertor heat sink is depicted in Fig. 6.10.

Table 6.2: Detailed dimension of the nozzle exit geometries.

Name	Geometry	Major axis (mm)	Minor axis (mm)	Hydraulic Diameter (mm)
Case - A	○	0.60	0.60	0.60
Case - B	⬭	0.90	0.48	0.60
Case - C	⬯	0.90	0.48	0.60
Case - D	▭	0.80	0.50	0.60
Case - E	▯	0.80	0.50	0.60
Case - F	□	0.60	0.60	0.60
Case - G	△	0.90	0.90	0.60

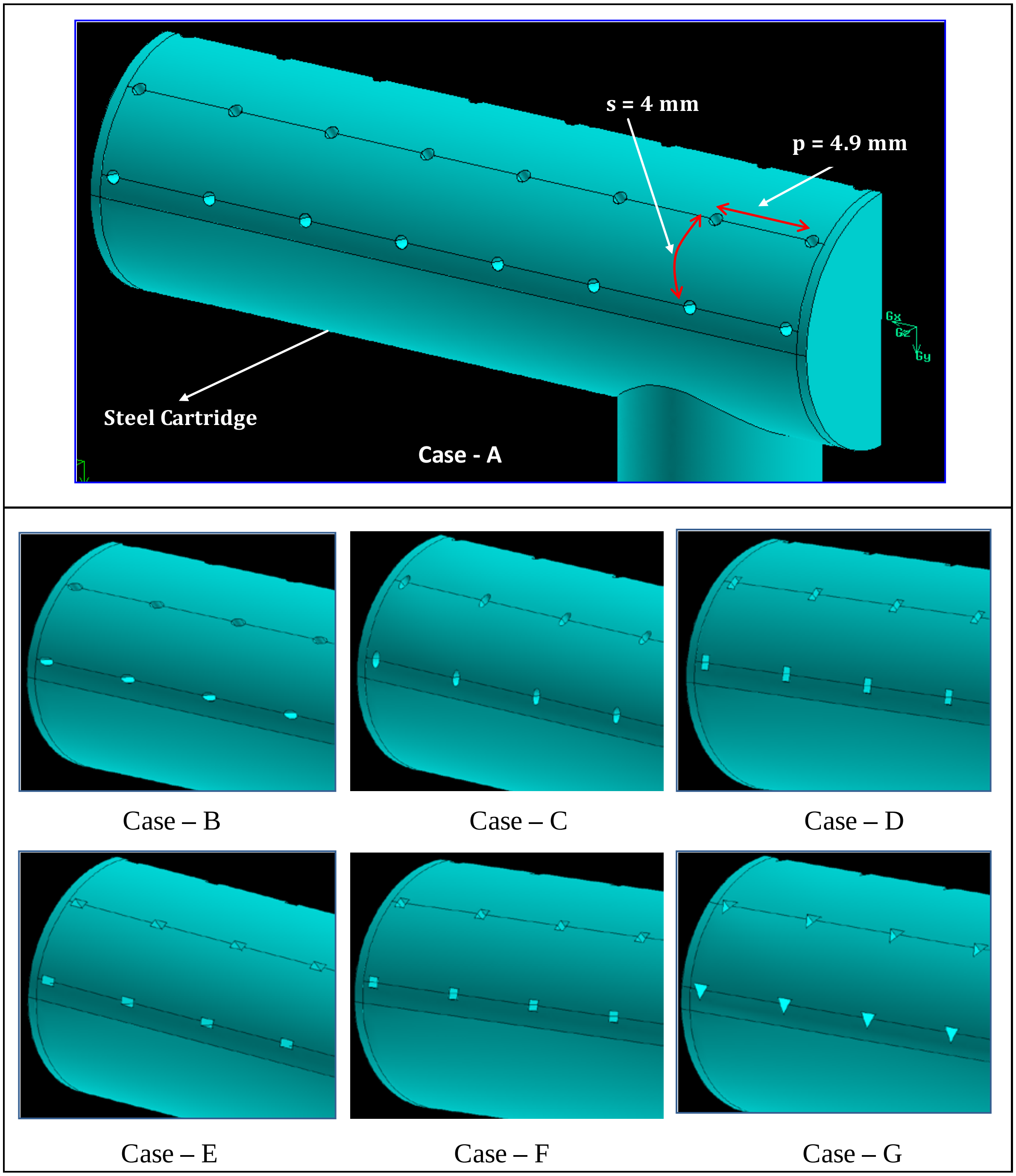

Fig. 6.10. Schematic of different nozzle shapes studied for divertor heat sink.

A comparison of thermal shield and thimble temperature for the various nozzle shapes is shown in Figs. 6.11(a) and (b). It can be observed that, the thermal shield and thimble temperatures are the minimum for the elliptical nozzle (case-B) as compared to all the other cases. The maximum deviation among the various cases is ~30°C. Figure 6.12 is a comparison of the turbulent kinetic energy (TKE) at Re = 1.58×10^4 for elliptical and circular nozzles. It can be observe that, TKE is higher for the case of elliptical nozzle contributing to increase mixing and the associates increased in HTC.

It can be noticed that the square nozzle (case-F) also offer a temperature similar to the circular nozzle (case-A) for the same Re number. All the other nozzle shapes and vertical orientation of nozzles (case-C and E) are counterproductive towards the thermal performance of divertor heat sink. The lowest tile and thimble temperatures achieved for elliptical nozzle are respectively ~12°C and ~18°C less than the reference circular nozzle at same Re_p number.

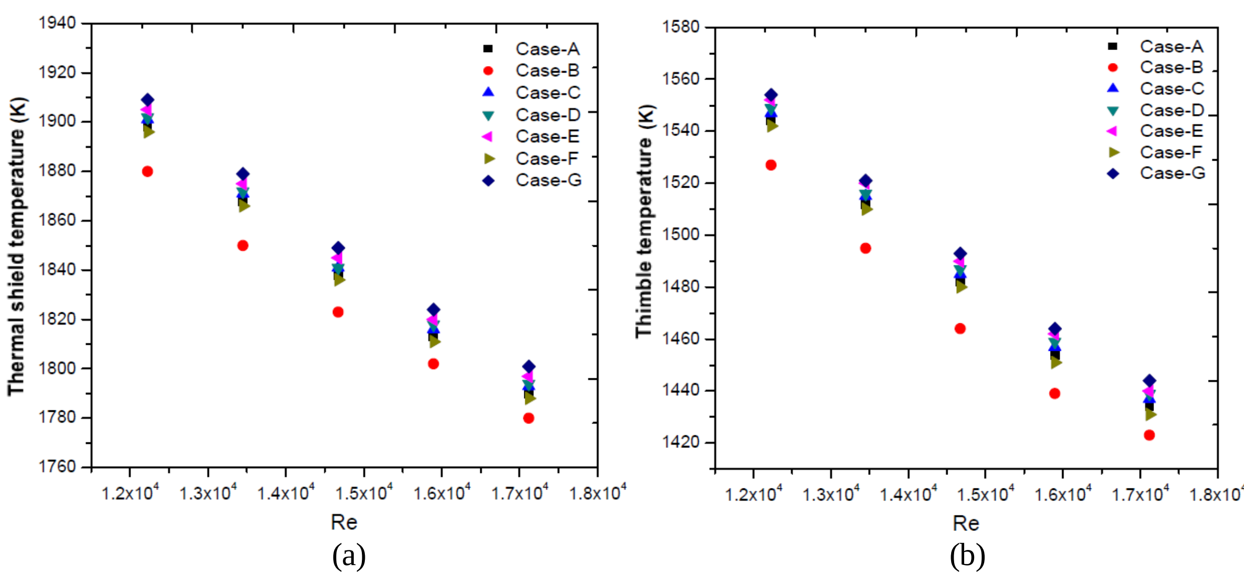

Fig. 6.11. Influence of nozzle shape on the maximum temperature (a) thermal shield and (b) thimble.

Figures 6.13(a) and (b) illustrate the dependence of pressure drop and pumping power ratio on Re number for the various nozzle shapes. It is clear that both pressure drop and pumping power ratio are the highest for triangular nozzles. Similarly, the elliptical nozzle also demands marginally higher pumping power compared to the reference case-A.

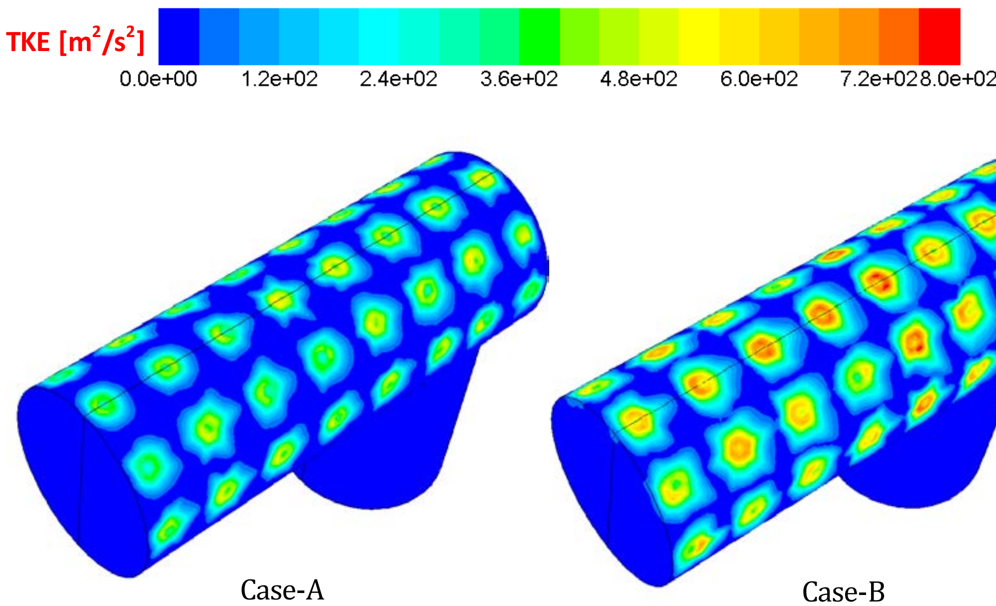

Fig. 6.12. Comparison of turbulence kinetic energy distributions for reference case-A and optimized case-B at Re = 1.58×10^4.

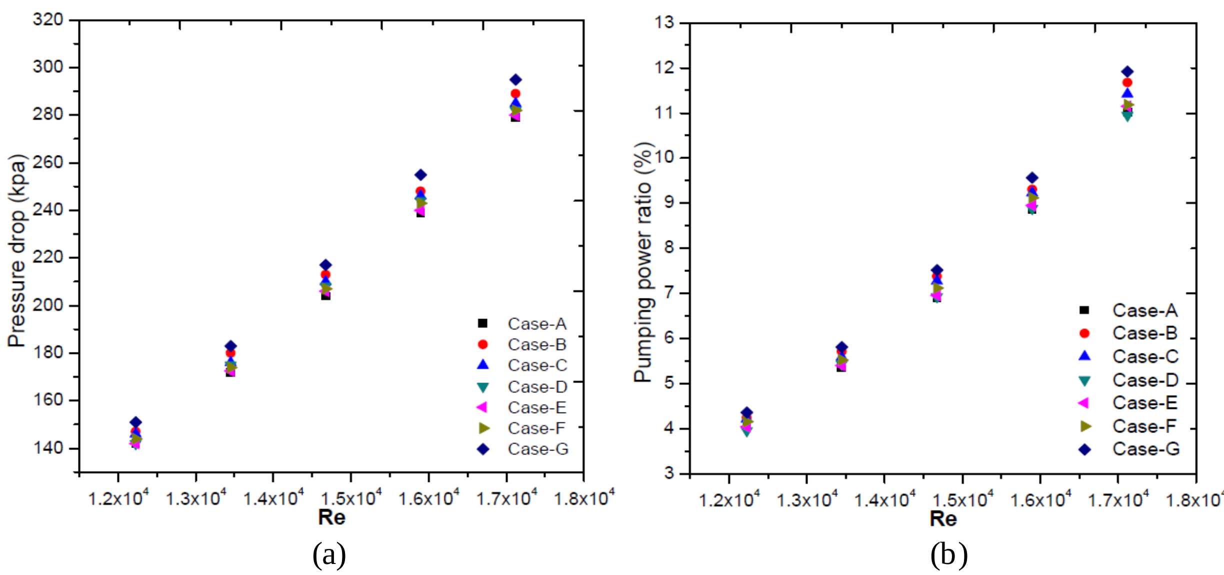

Fig. 6.13. Influence of shape of nozzle on (a) pressure drop and (b) pumping power ratio.

6.3.4. Design Analysis of Divertor Heat Sink Concept at Different Heat flux

Thermal-hydraulic performance of divertor heat sink concept has been investigated at higher thermal loads to estimate the tolerance of the design. Towards this, numerical studies have been performed at various heat flux values, viz., 8, 10, 11, and 12 MW/m^2 over a wide range of Re number 1.2 x 10^4 - 3.0 x 10^4 for the optimized divertor heat sink design. The temperature distribution on the surface of thermal shield and thimble at various heat loads are depicted in Fig. 6.14(a) and (b), respectively.

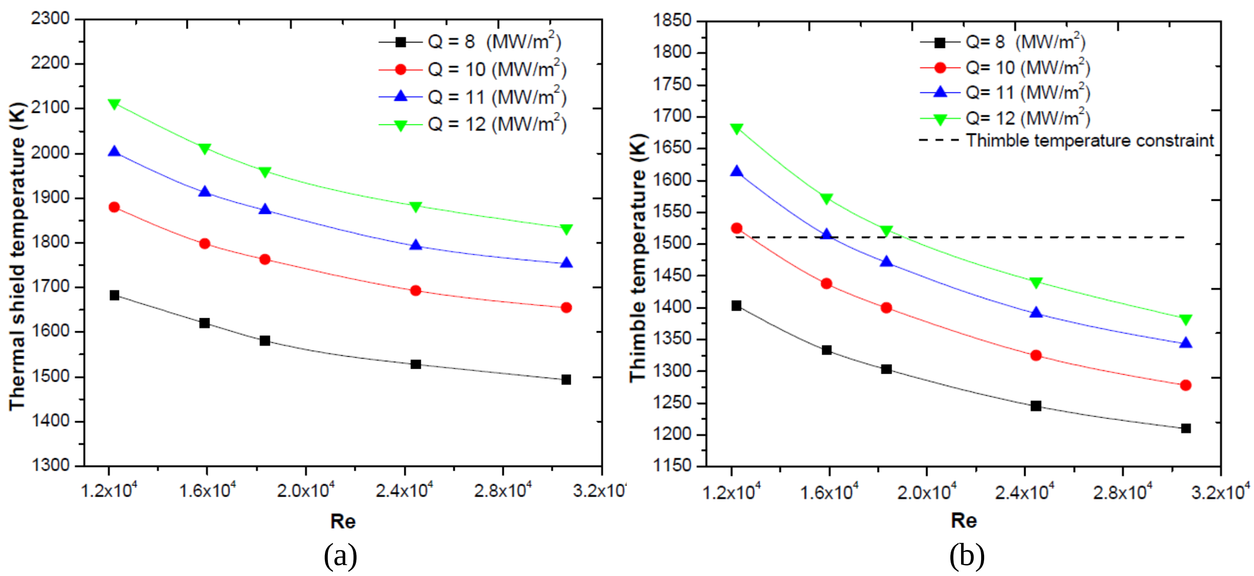

Fig. 6.14. Comparison between (a) maximum thermal shield and (b) thimble temperature at different heat loads.

The peak temperature increases linearly with increase in heat flux at a fixed Re number. This is expected because for identical heat transfer coefficient and fluid temperature, the peak structural temperature is directly proportional to heat flux. Further, for a fixed heat flux the peak temperature decreases gradually with Re number, as the heat transfer coefficient increases as Re$^{0.66}$ (Fig. 6.15).

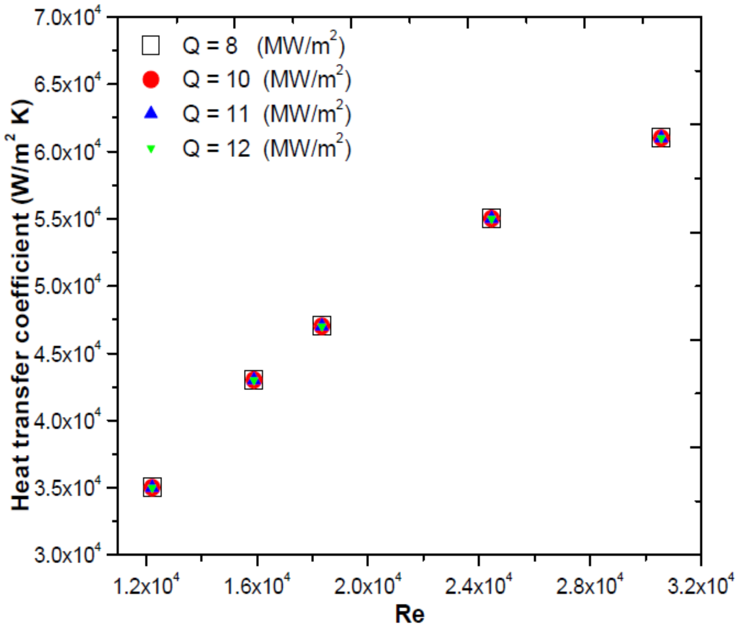

Fig. 6.15. Comparison between wall heat transfer coefficient against various heat loads.

It can be seen that, max temperature of divertor heat sink is well within the design limits for heat loads of $\leq$ 10 MW/m^2 at Re_p = 1.58 x 10^4. On the other hand, when the heat flux is 11 MW/m^2 the peak temperature on thimble would still be under the required temperature limit indicating a margin of 10% in the design. For heat flux values exceed 11 MW/m^2, the Re number has to be increased with the associated penalty in pumping power.

6.4. FINITE ELEMENT ANALYSIS

Structural analysis is performed to determine the state of stresses in divertor heat sink assembly as a result of high pressure (10 MPa) and large temperature gradient. The computed result of pressure and temperature distribution by the computational fluid dynamics analysis is used to carry out the thermo-mechanical analysis through finite element based program ANSYS Workbench 14.0.

6.4.1. Calculation Model, Meshing and Boundary condition

In the finite element study a computational model identical to that used as in CFD analysis has been adopted. The x-y plane is defined as the symmetry plane. The finite element mesh for the computational model is formed by the internal ANSYS Workbench mesh-tool. It consists of a uniform hexahedral mesh with ~2.5 x 10^4 elements. Temperature dependent material properties have been considered for the pure tungsten (W) and tungsten lanthanum oxide (WL-10). The values are taken from the ITER Material Handbook. The nodal temperature and pressure data are imported from CFD results (case-A) for the finite element analysis, and suspension is defined at the lower end of the thimble as frictionless.

6.4.2. Finite Element Analysis Results

Figure 6.16(a) represents the imported temperature distribution at the thimble surface from the CFD calculation. It can be seen that, the peak temperature at the thimble are very close to the CFD results, and the maximum deviation in imported temperature is found to be less than ~1 °C. Figure 6.16(b) depicts the predicted von-Misses stress distribution in the divertor heat sink design. It is seen that the maximum resulting stress in the thimble is ~365 MPa occurring in the sharp corner on its inner side at a temperature of ~726 °C, which is well below the allowable limit of~462 MPa [78]. Even an existing stress of about 145 MPa at thermal shield and the thimble interface at a maximum temperature of about ~1182 °C is still within the allowable value of about 310 MPa. For the tungsten tile the maximum stress is ~145 MPa. It occurs at the top surface at an existing temperature of ~1543 °C, and is well below the allowable limit of about 246 MPa.

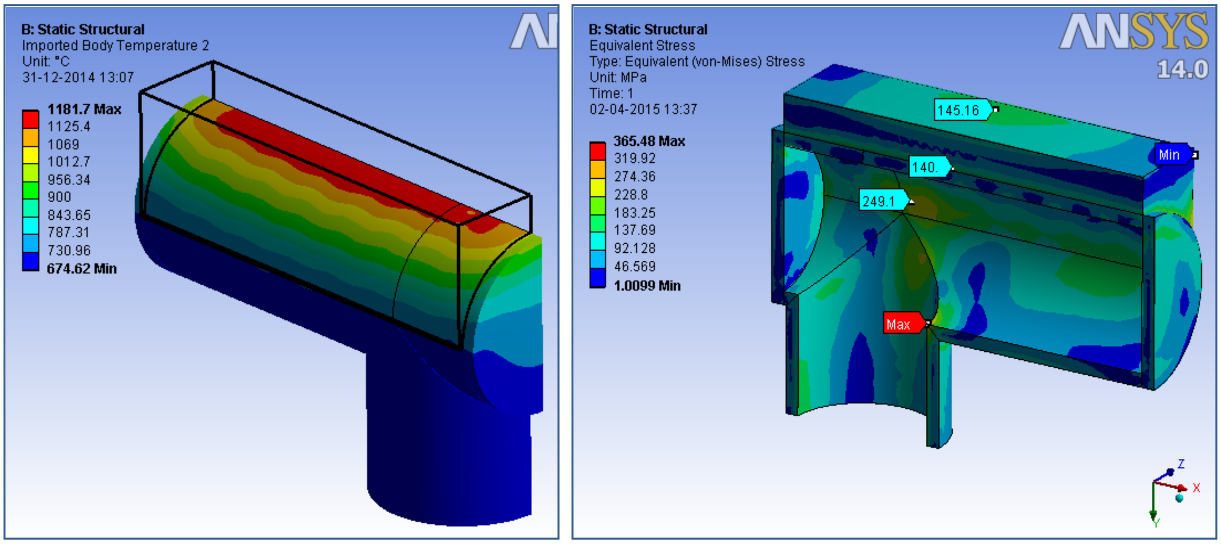

Fig. 6.16. Divertor heat sink (a) temperature distribution (b) von-Mises distribution.

6.5. CLOSURE

A multi jet helium cooling system has been proposed for use in fusion reactor application. 3 -dimensional thermal hydraulic investigations have been carried out to understand the performance of the cooling system as a function of various critical parameters which include thimble diameter, nozzle diameter, nozzle-to-wall space and nozzle shape etc. along with the nozzle Reynolds number. Elliptical nozzles at specific orientation are found to perform better than other nozzles for identical Reynolds number.

The performances of triangular nozzles are found to be poorer than other nozzles. Similarly, a minimum thimble temperature and pressure drop in the circuit is achieved at H/D_N ~1.66. The proposed design is found to have a margin of 10 % i.e., capable of handling 11 MW/m^2 against target heat flux values of 10 MW/m^2. Following the CFD investigation, structural analysis of the divertor heat sink assembly has been carried out and the stress values arising out of temperature gradient and pressure are found to be within acceptable limits, demanding the reliability of the proposed concept.

CHAPTER 7

CONCLUSIONS AND SCOPE FOR FUTURE STUDIES

7.0. INTRODUCTION

Helium cooled divertor concept relevant fusion reactor application has been studied in the present thesis work. Previous work reported by other groups and the associated issues/ concerns in those works are identified, viz., manufacturing difficulties, high heat flux removal capabilities, high pressure drops and absence of experimental validation associated with helium cooled divertor designs. Efforts are made to address some of the issues and improve the heat transfer capability as well as structural stability and propose a new design for the divertor.

The concept of “finger” type helium cooled divertor target for a tokamak based fusion reactor is investigated for its fluid flow and heat transfer characteristics. Computational fluid dynamic simulations as well as structural analysis are carried out for engineering design. The feasibility of implementing a novel concept of sectorial extended surface (SES) is studied for enhancement of heat transfer. Design is further optimized for maximum heat transfer rate at minimal pressure drop. Optimized design is used for the actual fabrication of a test mock-up for experimental studies on heat transfer and pressure drop. An experimental setup based on high pressure air-loop is established for experimental investigations of heat transfer and pressure drop studies for the fabricated test mock-up. Experimental results are found to be in agreement with the results of numerical simulations for heat transfer rate and pressure drop across the mock-up. Along with the “finger” concept, an innovative divertor heat sink concept is also proposed and numerically investigated for the divertor target.

Major observations and conclusions drawn from the results of Chapters 3 to 6 are summarized below.

7.1. Numerical Studies on Helium Cooled Divertor Finger Mock Up with Sectorial Extended Surfaces:

- ❖ Numerical investigations showed that addition of SES greatly increases thermal performance of the divertor "finger" type mock-up.
- ❖ Performance analysis indicates that the present mock-up design should be acceptable for mass flow rate less than 7.3 g/s to ensure desired pumping power and thimble temperature limits.
- ❖ Adding the array of extended surface, doubles the maximum heat flux that can be accommodated by the divertor finger mock-up.
- ❖ Thermo-mechanical analysis has been carried out for the "finger" type mock-up through finite element based approach. It is seen that, all the stresses are within the permissible limits.

7.2. Experimental Studies with Divertor Finger Mock-Up and Validation of CFD Model:

- ❖ A heat concentrator with electrical heater has been designed to achieve a heat flux of 0.75 MW/m^2. "Finger" type mock-up thermally attached to the heat concentrator is tested for pressure drop and heat transfer coefficient. The same experimental set-up is also numerically simulated as a conjugate CFD study.
- ❖ The computational result for heat transfer coefficients and pressure loss are in satisfactory agreement with the experimental results.
- ❖ Deviation observed between the measured and predicted results for HTC is ~6.5% and for pressure drop is 8% at the prototypical Reynolds number.
- ❖ Correlations have been proposed for Nusselt number (Nu) and pressure loss coefficient (K_L) as a function of Reynolds number which can be used for design applications.
- ❖ The efficiency and effectiveness of the SES are found to be ~ 89% and ~2.98, respectively at the prototypical Reynolds number.

7.3. Geometric Optimization of Divertor Heat Sink with Sectorial Extended Surfaces:

- The 'tile' and 'thimble' temperatures decrease considerably whereas the pressure drop and the pumping power ratio increase significantly with an increase in flow Reynolds number.
- The thermal performance of divertor finger mock-up is significantly improved for the two optimum designs, having relative pitch and thickness of 0.30 (case 'D') and 0.56 (case 'F'), compared to the reference design (case 'B').
- The influence of the h/D ratio on the performance of divertor finger mock-up heat sink is noticeable. It is observed that, in cases 'J' and 'M' (h/D = 0.75) the tile and thimble temperatures appreciably reduce with marginally higher pumping power ratio than the target value by ~3%.
- The effect of jet diameter (D) and circumferential position of SES are found to be counterproductive towards the heat transfer performance.
- The deviation in peak stresses for various optimized geometries are within the design limits. The maximum stress deviation for the optimized design is ~ 1.4%.

7.4. Computational Fluid Dynamic Studies on New Concept for Helium Cooled Divertor:

- Three dimensional thermal hydraulic investigations have been carried out to understand the performance of the proposed helium cooling system for use in fusion reactor application.
- The proposed design is found to have a safety margin of 10 % above design value i.e., it is capable of handling 11 MW/m^2 against target heat flux values of 10 MW/m^2.
- Elliptical nozzles at specific orientation are found to perform better than other nozzles for identical Reynolds number. The performances of triangular nozzles are found to be poorest amongst other shapes of nozzles studied.
- Similarly, a minimum thimble temperature and pressure drop in the circuit is achieved at H/D_N ~1.66.
- The maximum resulting stress in the thimble is ~365 MPa occurring in the sharp corner on its inner side at a temperature of ~726 °C, which is below the allowable limit of~462 MPa.

7.5. FUTURE STUDIES

The following are the main issues may be addressed in future studies:

- Finger mock-up design may be fabricated from actual tungsten material to perform the experiment.
- Pressurized loop for helium may be designed and developed to perform the experiment in the prototypical condition to validate the findings.
- The proposed divertor heat sink design may be manufactured and experiment can be performed with air loop or helium loop.

REFERENCES

[1] IPCC Fifth Assessment Report: Climate Change 2014. [http://www.ipcc.ch/pdf/ assessment-report/ar5/syr/AR5_SYR_FINAL_SPM.pdf].

[2] Growth of Electricity Sector in India from 1947-2015, CEA, India. [http://www.cea.nic.in /reports/planning/dmlf/growth_2015.pdf], Retrieved 13 June 2015.

[3] D.J. Ward, The contribution of fusion to sustainable development, *Fusion Engineering and Design*, **82** (2007) 528 – 533.

[4] K. Miyamoto, Plasma Physics For Nuclear Fusion, MIT Press, 1989.

[5] M. Kikuchi et al., Fusion Physics, IAEA, Vienna, 2012.

[6] J. Wesson, Tokamaks, 3rd Edition, Oxford University Press.

[7] J.D. Lawson, Some Criteria for a Useful Thermonuclear Reactor, Atomic Energy Research Establishment, Culham Report No: A.E.R.E. GP/R – 1807 (1955).

[8] W.M. Stacey, Fusion: An Introduction to the Physics and Technology of Magnetic Confinement Fusion, 2nd edition, Wiley Publication (DOI: 10.1002/9783527629312), 2010.

[9] J.A. Boedo, G.D. Porter, M.J. Schaffer, R. Lehmer, Flow reversal, convection, and modeling in the DIII-D divertor, *Physics of Plasma*, **5** (1998) 4305 - 4310.

[10] N. Asakura, S. Sakurai, M. Shimada, Y. Koide et al., Measurement of natural plasma flow along the field lines in the scrape-off layer on the JT-60U Divertor Tokamak, *Physical Review Letter*, **84** (2000) 3093 - 4101.

[11] S.K. Erents, A.V. Chankin, G.F. Matthews, P.C. Stangeby, Parallel flow in the JET scrape-off layer, *Plasma Physics and Controlled Fusion*, **42** (2000) 905 - 915.

[12] J.P. Gunn, C. Boucher, M. Dionne, I. Ďuran et al., Evidence for a poloidally localized enhancement of radial transport in the scrape-off layer of the Tore Supra tokamak, *Journal of Nuclear Materials*, **363–365** (2007) 484 - 490.

[13] G.S. Xu, B.N. Wan, H.Q. Wang, H.Y. Guo et al., First evidence of the role of zonal flows for the L-H transition at marginal input power in the EAST tokamak, *Physical Review Letter*, **10** (2011) 125001- 125005.

[14] A.R. Field, P.G. Carolan, N.J. Conway, G.F. Counsell et al., The influence of gas fuelling location on H-mode access in the MAST spherical tokamak, *Plasma Physics and Controlled Fusion*, **46** (2004) 981 - 1006.

[15] G.S. Xu, B.N. Wan, M. Song, J. Li, Direct measurement of poloidal long-wavelength E×B flows in the HT-7 tokamak, *Physical Review Letter*, **91** (2003) 125001 - 125004.

[16] P. Chaudhuri, S.K.S. Parashar, P. Santra, D.C. Reddy, Thermal-hydraulics and thermo-mechanical design of plasma facing components for SST-1 tokamak, *International Journal of Thermal Sciences*, **86** (2014) 299-306.

[17] S. Jacob, S.S. Khirwadkar, P. Sinha, H.A. Pathak et al., Plasma facing component design for steady state tokamak SST-1, *Journal of Nuclear Materials*, **233-237** (1996) 655-659.

[18] D. Sangwan, R. Jha, J. Brotankova, M.V. Gopalkrishna, Plasma flows in scrape-off layer of Aditya tokamak, *Physics of Plasmas*, **19** (2012) 0925071 - 0925076.

[19] K. Tomabechi, J.R. Gilleland, Yu.A. Sokolov, R. Toschi and ITER Team, ITER conceptual design, *Nuclear Fusion*, **31** (1991) 1135 - 1224.

[20] S.S. Khirwadkar, K.P. Singh, Y.Patil, M.S. Khan et al., Fabrication and characterization of tungsten and graphite based PFC for divertor target elements of ITER like tokamak application, *Fusion Engineering and Design*, **86** (2011) 1736-1740.

[21] D. Maisonnier, I. Cook, S. Pierre, B. Lorenzo et al., DEMO and fusion power plant conceptual studies in Europe, *Fusion Engineering and Design*, **81** (2006) 1123 – 1130.

[22] T.J. Dolan, Magnetic Fusion Technology, Springer Science & Business Media, USA, 2014.

[23] P. Norajitra, R. Giniyatulin, V. Kuznetsov, I. V. Marshall et al., He-cooled divertor for DEMO: Status of development and HHF tests, *Fusion Engineering and Design*, **85** (2010) 2251 – 2256.

[24] H. Meister, R. Fischer, L.D. Horton, C.F. Maggi et al., Zeff from spectroscopic bremsstrahlung measurements at ASDEX Upgrade and JET, *33rd EPS Conference on Plasma Physics*. Rome, 19 – 23 June 2006.

[25] T. Ihli, He-cooled Divertor Development in the EU: The Helium Jet cooled Divertor HEMJ in *ARIES Meeting*, San Diego, CA, 2005.

[26] H. Bolt, V. Barabash, G. Federici, J. Linke et al., Plasma facing and high heat flux materials - needs for ITER and beyond, *Journal of Nuclear Materials*, **307-311 (**2002) 43 - 52.

[27] M. Merola, D. Loesser, A. Martin, P. Chappuis et al., ITER plasma-facing components, *Fusion Engineering and Design*, **85** (2010) 2312 - 2322.

[28] R. Pitts, S. Carpentier, F. Escourbiac, T. Hirai et al., Physics basis and design of the ITER plasma-facing components, *Journal of Nuclear Materials*, **415** (2011) 957 - 964.

[29] W.P. Beak, S.H. Chang, Coolant option and critical heat flux issues in fusion reactor divertor design, *Journal of Korean Nuclear Society*, **29** (1996) 348 - 359.

[30] M.S. Tillack, P.W. Humrickhouse, S. Malang, A.F. Rowcliffe, The use of water in a fusion power core, *Fusion Engineering and Design*, **91** (2015) 52 – 59.

[31] C.P.C. Wong, C.B. Baxi, C.J. Hamilton, R.W. Schleicher et al., Helium-cooling in fusion power plants, 15th *International Conference Plasma Physics and Controlled Nuclear Fusion Research*, Seville, Spain, 26th Sept – 1st Oct 1994.

[32] K.R. Schultz, Gas-cooled fusion-fission hybrid reactor systems, *Journal of Fusion Energy*, **1** (1981) 163 – 183.

[33] C.B. Baxi, Evaluation of helium cooling for fusion divertors, *Fusion Engineering and Design*, **25** (1994) 263 – 271.

[34] C.B. Baxi, C.P.C. Wong, Review of helium cooling for fusion reactor application, *Fusion Engineering and Design*, **51 – 52 (**1994) 319 – 324.

[35] T. Ihli, M. Ilić, Efficient helium cooling methods for nuclear fusion devices: Status and prospects, *Fusion Engineering and Design*, **84 (**2009) 964 – 968.

[36] S. Hermsmeyer, K. Kleefeldt, Review and Comparative Assessment of Helium-Cooled Divertor Concepts, FZKA 6597, 2001.

[37] D.L. Youchison, M.T. North, J.E. Lindemuth, J.M. McDonald et al., Thermal performance and flow instabilities in a multi-channel, helium-cooled, porous metal divertor module, *Fusion Engineering and Design*, **49–50** (2000) 407 – 415.

[38] E. Gayton, L. Crosatti, D.L. Sadowski, S.I. Abdel-Khalik, M.Yoda et al., Experimental and numerical investigation of the thermal performance of the gas cooled divertor plate concept, *Fusion Science and Technology*, **56** (2009) 75 - 79.

[39] M.D. Hageman, D.L. Sadowski, M. Yoda, S.I. Abdel-Khalik, Experimental studies of the thermal performance of gas cooled plate type divertor, *Fusion Science and Technology*, **60** (2011) 228 - 232.

[40] X.R. Wang, S. Malang, A.R. Raffray and the ARIES Team, Design optimization of high performance helium-cooled divertor plate concept, *Fusion Science and Technology*, **56** (2009) 1023 – 1027.

[41] A. Pizzuto, P.J. Karditsas, C. Nardi, S. Papastergiou, HETS performances in helium cooled power plant divertor, *Fusion Engineering and Design*, **75–79 (**2005) 481 – 484.

[42] E. Visca, P. Agostini, F. Crescenzi, A. Malavasi et al., Manufacturing and testing of a HETS module for DEMO divertor, *Fusion Engineering and Design*, **87** (2012) 941– 945.

[43] P. J. Karditsas, Optimization of the HETS He-cooled divertor concept: Thermal fluid and structural analysis, *Fusion Science and Technology*, **47** (2005) 729 – 733.

[44] P. Norajitra, S.I. Abdel-Khalik, L. M. Giancarli, T. Ihli et al., Divertor conceptual designs for a fusion power plant, *Fusion Engineering and Design*, **83** (2008) 893 – 902.

[45] E. Diegele, et al., Modular helium cooled divertor for power plant application, *Fusion Engineering and Design*, **66 – 68 (**2003) 383 - 387.

[46] T. Ihli, R. Kruessmann, I. Ovchinnikov, P. Norajitra et al., An advanced He-cooled divertor concept: Design, cooling technology, and thermo-hydraulic analyses with CFD, *Fusion Engineering and Design*, **75–79** (2005) 371 – 375.

[47] R. Kruessmann, G. Messemer, P. Norajitra, J.Weggen et al., Validation of computational fluid dynamics (CFD) tools for the development of a helium-cooled divertor, *Fusion Engineering and Design*, **82** (2007) 2812 – 2816.

[48] B. Končar, P. Norajitra, K. Oblak, Effect of nozzle sizes on jet impingement heat transfer in He-cooled divertor, *Applied Thermal Engineering*, **30** (2010) 697 – 705.

[49] V. Widak, P. Norajitra, Optimization of He-cooled divertor cooling fingers using a CAD-FEM method, *Fusion Engineering and Design*, **84 (**2009) 1973 – 1978.

[50] P. Norajitra, S. Antusch, R. Giniyatulin, V. Kuznetsov, Progress of He-cooled divertor development for DEMO, *Fusion Engineering and Design*, **86** (2011) 1656 – 1659.

[51] P. Norajitra, R. Giniyatulin, T. Hirai, W. Krauss et al., Current status of He-cooled divertor development for DEMO, *Fusion Engineering and Design*, **84** (2009) 1429–1433.

[52] P. Norajitra, S. Antusch, R. Giniyatulin, I. Mazul et al., Current state-of-the-art manufacturing technology for He-cooled divertor finger, *Journal of Nuclear Materials*, **417** (2011) 468 – 471.

[53] J. Aktaa, W.W. Basuki, T. Weber, P. Norajitra et al., Manufacturing and joining technologies for helium cooled divertors, *Fusion Engineering and Design*, **89** (2014) 913 – 920.

[54] F. Arbeiter, S. Gordeev, V. Heinzel, V. Slobodtchouk, Analysis of turbulence models for thermohydraulic calculations of helium cooled fusion reactor components, *Fusion Engineering and Design*, **81** (2006) 1555 – 1560.

[55] W. Yuan, J. Zhao, C.P. Tso, T. Wu, W. Liu, T. Ming, Numerical simulation of the thermal hydraulic performance of a plate pin fin heat sink, *Applied Thermal Engineering*, **48** (2012) 81 - 88.

[56] L. Li, X. Du, L. Yang, Y. Xu, Y. Yang, Numerical simulation on flow and heat transfer of fin structure in air-cooled heat exchanger, *Applied Thermal Engineering*, **59** (2013) 77-86.

[57] H. Shafeie, O. Abouali, K. Jafarpur, G. Ahmadi, Numerical study of heat transfer performance of single-phase heat sinks with micro pin-fin structures, *Applied Thermal Engineering*, **58** (2013) 68 - 76.

[58] M.A. Moon, K.Y. Kim, Analysis and optimization of fan-shaped pin–fin in a rectangular cooling channel, *International Journal of Heat and Mass Transfer*, **72 (**2014) 148 - 162.

[59] J. Dong, J. Chen, W. Zhang, J. Hu, Experimental and numerical investigation of thermal-hydraulic performance in wavy fin-and-flat tube heat exchangers, *Applied Thermal Engineering*, **30** (2010) 1377 - 1386.

[60] Z.M. Lin, L.B. Wang, Y.H. Zhang, Numerical study on heat transfer enhancement of circular tube bank fin heat exchanger with interrupted annular groove fin, *Applied Thermal Engineering*, **73** (2014) 1465 - 1476.

[61] G.J.V. Fossen, Heat transfer coefficients for staggered arrays of short pin fins, *Journal of Engineering for gas Turbines and Power*, **104** (1982) 268 – 274.

[62] E.M. Sparrow, J.W. Ramsey, C.A. Altemani, Experiments on in-line pin fin arrays and performance comparisons with staggered arrays, *Journal of Heat Transfer*, **102** (1980) 44–50. .

[63] J.T. Collins, C.M. Conley, N.A. John, Enhanced heat transfer using wire-coil inserts for high- heat-load applications**,** 2nd *International Workshop on Mechanical Engineering Design of Synchrotron Radiation Equipment and Instrumentation* (MEDSI02), Argonne, Illinois, U.S.A, 2002.

[64] H.K. Moon, T.O. Connell, B. Gletzer, Channel height effect on heat transfer and friction in a dimpled passage, *Journal of Engineering for Gas Turbine and Power*, **122** (2000) 307 – 313.

[65] G.I. Mahmood, P.M. Ligrani, Heat transfer in a dimpled channel: combined influences of aspect ratio, Temperature ratio, Reynolds number and flow structure, *International Journal of Heat and Mass Transfer*, **45** (2002) 2011 – 2020.

[66] G.I. Mahmood, M.L. Hill, D.L. Nelson, P.M. Ligrani, H.K. Moon, B. Glezer, Localheat transfer and flow structure on and above a dimpled surface in a channel, *Journal of Turbomachinery*, **123** (2001) 115 – 123.

[67] R. Narayanaswamy, T.T. Chandratilleke, A.F. Jun Li, Thermodynamic analysis of heat and fluid flow in a microchannel with internal fins, *ASME Summer Heat Transfer Conference*, San Francisco, USA, 19th Jul 2009 (Paper No. HT200988107, pp. 785-792, DOI: 10.11.1115/HT2009-88107).

[68] R. Narayanaswamy, A.F. Jun Li, T.T. Chandratilleke, Numerical analysis of microchannels with internal longitudinal fins, 20th *National and* 9th *International ISHMT-ASME Heat and Mass Transfer Conference*, Mumbai, India, 4th Jan 2010.

[69] S.V. Patankar, Numerical Heat Transfer and Fluid Flow, Hemisphere, New York, 1980.

[70] ANSYS FLUENT, Release 14.0, User Guide, Ansys, Inc., Lebanon, US, 2011.

[71] H.K. Versteeg, W. Malalasekra, An Introduction to Computational Fluid Dynamics,Second Edition, Pearson Education, 1995.

[72] C.J. Chen, S.Y. Jaw, Fundamentals of Turbulence Modeling, Taylor and Francis Publishers, Washington, 1997.

[73] B.E. Launder, D.B. Spalding, The numerical computation of turbulent flows, *Computer Methods in Applied Mechanics and Engineering*, **3** (1974) 269 – 289.

[74] K. Shimada, T. Isihara, Application of a modified k-epsilon model to prediction of aerodynamics characteristics of rectangular cross-section cylinder, *Journal of Fluids and Structures*, **16** (2002) 465 – 485.

[75] D.C. Wilcox, Turbulence Modeling for CFD, **3rd** Edition, DCW Industries, La Canada CA, 2006.

[76] B. Raj, T. Jayakumar, Development of Reduced Activation Ferritic–Martensitic Steels and fabrication technologies for Indian test blanket module, *Journal of Nuclear Materials*, **417** (2011) 72 – 76.

[77] G. Xie, B. Sundén den, W. Zhang, Comparisons of pins/dimples/protrusions cooling concepts for a turbine blade tip wall at high Reynolds numbers, *Journal of Heat Transfer*, **133** (2011) 061902 - 061909.

[78] ITER, Material Properties Handbook, 2001, ITER Document No. G. 74 MA 900-11-10W 0.1.

[79] Y. Cengel, A. Ghajar, Heat and Mass Transfer Fundamentals & Applications, McGraw-Hill, Noida, India, 2011.

[80] X. Yu, J. Feng, Q. Feng, Q. Wang, Development of a plate-pin fin heat sin its performance comparisons with a plate fin heat sink, *Applied Thermal Engineering*, **25** (2005) 173 – 182.

[81] G. Xie, B. Sunden, L. Wang, E. Utriainien, Augmented heat transfer of an internal blade tip by full or partial arrays of pin-fins, *Heat Transfer Research*, **42** (2011) 65 – 81.

[82] P. R. Bevington, D. K. Robinson, Data Reduction and Error Analysis for the Physic Sciences, 3rd Ed., McGraw-Hill, New York City, 2003.

[83] S. Rimza, K. Satpathy, S. Khirwadkar, K. Velusamy, Numerical studies on helium cooled divertor finger mock up with sectorial extended surfaces, *Fusion Engineering and Design*, **89** (2014) 2647 - 2658.

[84] H.D. Steffens, H. Lange, Fifth International AWS-WRC brazing conference, Houston, Texas, May 7-9, 1974.

[85] A. Roth, Vacuum Technology (3rd Edition), Elsevier Science, Amsterdam, Netherlands, 1996.

[86] C.J. Smithells, Metals Reference Book (5th Edition), Butterworth, London, England, 1549-1550, 1976.

[87] G. Sheward, High temperature brazing in controlled atmospheres, Pergamon, Oxford, New York, 1985.

[88] X. Yang, X. Long, X. Yao, Numerical investigation on the mixing process in a steam ejector with different nozzle structures, International Journal of Thermal Sciences,**56** (2012) 95–106.

[89] T. Sriveerakul, S. Aphornratana, K. Chunnanond, Performance prediction of steam ejector using computational fluid dynamics: Part 1. Validation of the CFD results, International Journal of Thermal Sciences, **46** (2007) 812–822.

Nomenclature

A	area of top surface wall, m^2
A_c	area of cooled inner surface wall, m^2
A_p	area of bare plate between the sectorial extended surfaces, m^2
A_e	surface area of the sectorial extended surface, m^2
A_{ce}	cross section area of the sectorial extended surface, m^2
A_{jet}	area of jet, m^2
C_p	coefficient of heat capacity, J/kg-K
D	diameter, m
D_T	diameter thimble, m
D_N	diameter nozzle, m
h_{eff}	effective heat transfer coefficient, W/m^2-K
h_{act}	actual heat transfer coefficient, W/m^2-K
h	height of extended surface, m
K_{eff}	effective thermal conductivity of fluid, W/m-K
K_l	laminar thermal conductivity of fluid, W/m-K
K_t	turbulent thermal conductivity of fluid, W/m-K
k	turbulent kinetic energy, m^2/s^2
L	length scale, m
l	length of extended surface, m
m	mass flow rate, kg/s
Nu	Nusselt number
K_L	pressure loss coefficient
J	pumping power ratio
P	pressure, Pa
P_e	perimeter of the sectorial extended surface, m
P_r	Prandtl number
p	pitch of extended surface, m
s	circumferential pitch, m
Q	total incident power, Watt
Re	Reynolds number

Re_p prototypical Reynolds number

r radial coordinate, m

t thickness of extended surface, m

T temperature, K

TCs thermocouples

T_b bulk temperature of the fluid, $(T_i + T_o)/ 2$, K

T_i inlet temperature of fluid, K

T_o outlet temperature of fluid, K

$\overline{T_c}$ area weighted temperature, K

u_j velocity components in three spatial directions, m/s

v jet velocity, m/s

W pumping power, Watt

GREEK SYMBOLS

β circumferential position of SES

δ_p relative pitch

δ_t relative thickness

η efficiency of the sectorial extended surface

λ_s thermal conductivity of solid, W/m-K

λ_e thermal conductivity of the extended surface, W/m-K

λ_t thermal conductivity of the thimble, W/m-K

μ_{eff} effective viscosity of the fluid, N-s/m^2

μ_l laminar viscosity of the fluid, N-s/m^2

μ_t turbulent viscosity of the fluid, N-s/m^2

ε rate of dissipation, m^2/s^3

ρ density of fluid, kg/m^3

ζ effectiveness of the sectorial extended surface

SUBSCRIPT

c	cooled inner surface wall
p	plate
e	extended surface
ce	cross section of extended surface
jet	jet
T	thimble
N	nozzle
eff	effective
act	actual
l	laminar
t	turbulent
p	prototypical
b	bulk
i	inlet
o	outlet

ACRONYM

CFC	Carbon Fibre Composite
CFD	Computational Fluid Dynamics
DBTT	Ductile-to-Brittle Transition Temperature
HETS	High Efficiency Thermal Shield
HTC	Heat Transfer Coefficient
ITER	International Thermonuclear Experimental Reactor
ID	Internal Diameter
LCFS	Last Closed Flux Surface
MCF	Magnetic Confinement Fusion
OD	Outer Diameter
PDE	Partial Differential Equations
PFC	Plasma Facing Component
RANS	Reynolds Averaged Navier Stokes

RAFMS	Reduced Activation Ferritic Martensitic steel
RCT	Recrystallisation Temperature
SOL	Scrape-off Layer
SES	Sectorial Extended Surface